STRUCTURAL, MAGNETIC AND MAGNETOSTRICTIVE PROPERTIES OF SUBSTITUTED LANTHANUM MANGANITES AND SPINEL FERRITES

THESIS
SUBMITTED TO THE
UNIVERSITY OF PUNE
FOR THE DEGREE OF
DOCTOR OF PHILOSOPHY
IN CHEMISTRY

By
Shekhar D. Bhame
Physical and Materials Chemistry Division
National Chemical Laboratory
Pune 411008
India

August 2007

CERTIFICATE

Certified that the work incorporated in the thesis

Structural, Magnetic and Magnetostrictive Properties of Substituted Lanthanum Manganites and Spinel Ferrites

submitted by **Mr. SHEKHAR D. BHAME** for the Degree of *Doctor of Philosophy* in Chemistry was carried out by the candidate under my supervision at the Physical & Materials Chemistry Division of National Chemical Laboratory, Pune. Such material as has been obtained from other sources has been duly acknowledged in the thesis.

Date:

Place: Pune

Dr. P. A. Joy

(Research Guide)

...Dedicated to my Parents...

DECLARATION BY RESEARCH SCHOLAR

I hereby declare that the thesis entitled "**STRUCTURAL, MAGNETIC AND MAGNETOSTRICTIVE PROPERTIES OF SUBSTITUTED LANTHANUM MANGANITES AND SPINEL FERRITES**", submitted for the Degree of Doctor of Philosophy in Chemistry to the University of Pune, has been carried out by me at the Physical & Materials Chemistry Division, National Chemical Laboratory, Pune, India, under the supervision of Dr. P. A. Joy (Research Guide). The work is original and has not been submitted in part or full by me for any other degree or diploma to this or any other University.

Shekhar D. Bhame

Date:
Physical & Materials Chemistry Division
National Chemical Laboratory
Pune–411008
India

Acknowledgements

During the course of this thesis work, I have been accompanied and supported by many people. It is the pleasant moment and opportunity for me to express my gratitude for all of them.

I would like to thank my research guide ***Dr. P. A. Joy****, for introducing me to the wonderful world of magnetic materials. His endless patience and innovative suggestions have always been very crucial during the research period. His support and scientific attitude have meant a great deal to me. His constant striving for excellence coupled with his quest for knowledge will always remain a source of inspiration for me. I am deeply indebted to him for his immense help, suggestions and the inspiring discussions during writing and completion of this thesis.*

I express my sincere thanks to Dr. S. K. Date and Dr. S. Pal, former and present Head of the Physical Chemistry Division, for their constant support and encouragement. I thank Dr. S. Sivaram, Director of NCL, Pune, for giving me the opportunity to work in this institute and making all the facilities available for my research work. Also, I am grateful to CSIR, Govt. of India, for awarding me a research fellowship. I would like to express my profound gratitude to Dr. K. Vijayamohanan, Dr. M. Sastry, Dr. V. Ravi, Dr. H. S. Potdar, Dr. S. B. Deshpande, Dr. K. Sreedhar and Dr. B. L. V. Prasad, from Physical Chemistry Division, for their timely help and also being kind and considerate throughout my doctoral studies.

I would like to acknowledge all my former teachers especially Prof. A. S. Bhave, Dr.(Mrs.) Kashalkar, who guided me towards the right path to reach the present stage.

I am sincerely thankful to Dr.(Mrs.) S. D. Kulkarni, Mrs. R. Pasricha, Mr. A. B. Gaikwad and Mr. Deo, from the Center for Materials Characterization, NCL, for all the help in the characterizations required during my research work.

My sincere thanks are to my senior colleagues, Dr. S. Verma, Dr. Joly, Dr. R. Sankar, Dr. Dhage, Dr. Khollam and Dr. Deka, for their help, support, interest and valuable hints. A very special thanks to my fellow lab mates Ganga, Khaja, Vijay, Sreeja, Sudesh, Rubul, Mangesh and the project students who worked with me in the lab Venkat,

Savita, Jyostna and Prashant for their help and cooperation. I am thankful to Harawade Kaka for his care and help.

My sincere gratitude goes to my friends Sachin, Hrushikesh, Atul, Rohit, Shailesh, laxman, Nilkanth, Dinanath, Navnath and Pranjal for their support and love, especially during difficult times. I take this opportunity to thank Arun, Amit, Sachin, Omkar, Nitin, and Ajay who have helped me in all possible ways.

I would like to thank all my seniors and friends in NCL, Niranjan, Jadab, Deepali, Bhalchandra, Bhaskar, Kannan, Girish, Mandar, Mahima, Meera, Sanjay, Mukata, Sumant, Debu, Akhilesh, Amit, Sourav, Deepti, Anil, Sudarshan, Sanjay, Shanbhag, Thiru, Sankar, Diganta, Suvarna, Shraddha and Nagaeshwar, for the wonderful time I had with them.

I wish to thank my best friends Nikhil, Prajakta and Janaki for the sweet memories, we have had together in the past.

My sincere thanks to the staff of our divisional office specially Mr. Deepak Jori for his prompt help in administrative matters.

No thanks can be enough to acknowledge for the endless encouragement, care and support, which I had from my family members.

Shekhar D. Bhame

Contents

Abstract **1**

1 Introduction **5**

1.1 Materials Science 5

1.2 Magnetic Materials 6

1.3 Magnetism in Materials 7

1.3.1 Magnetic Moments of Electrons 7

1.3.2 Diamagnetism 9

1.3.3 Paramagnetism 9

1.3.4 Ferromagnetism 11

1.3.5 Antiferromagnetism 12

1.3.6 Ferrimagnetism 13

1.3.7 Superparamagnetism 13

1.3.8 Magnetization Process 14

1.3.9 Magnetic Exchange Interactions 15

1.3.10 Magnetic Anisotropy 16

1.4 Magnetostriction 17

1.4.1 Physical origin of Magnetostriction 21

1.4.2 Magnetostriction in Alloys 22

1.4.3 Magnetostriction in Oxides 23

1.4.4 Applications of Magnetostrictive Materials 25

1.5 Materials Studied In the Present Work 27

1.5.1 Spinel Ferrites 27

1.5.2 Perovskite Manganites 32

1.6 Scope of the Present Work 42

1.6.1 Magnetostrictive Investigations on Cobalt Ferrite 42

1.6.2 Magnetic Properties of $LaMn_{1-x}Fe_xO_3$ 42

2 Experimental Methods 57

2.1 Introduction 57

2.2 Synthesis 57

2.2.1 Ceramic Method 58

2.2.2 Ball Milling 58

2.2.3 Low-Temperature Methods 59

2.3 Characterization and Measurement Techniques 61

2.3.1 Powder X-Ray Diffraction 61

2.3.2 Transmission Electron Microscopy (TEM) 63

2.3.3 Scanning Electron Microscopy (SEM) 64

2.3.4 Thermo-Mechanical Analysis 64

2.3.5 Mössbauer Spectroscopy 66

2.3.6 Infrared spectroscopy 67

2.3.7 Electron Paramagnetic Resonance 68

2.3.8 Density Measurements 68

2.3.9 Magnetic measurements 69

3 Magnetostriction Studies on $CoFe_2O_4$ 79

3.1 Introduction 79

3.2 Preliminary Studies on $Co_xFe_{3-x}O_4$ 81

3.2.1 Powder XRD Analysis 81

3.2.2 TMA Analysis 82

3.2.3 Magnetic Measurements 83

3.2.4 Magnetostriction Studies 83

3.3 Studies on $CoFe_2O_4$ 85

3.3.1 Microstructural Analysis 85

3.3.2 Magnetic Measurements 86

3.3.3 Magnetostriction Studies 86

3.4 Studies on Nanosized $CoFe_2O_4$ 88

3.4.1 Synthesis 88
3.4.2 Powder XRD Analysis 89
3.4.3 TMA Analysis 90
3.4.4 SEM and TEM Analysis 92
3.4.5 Magnetic Measurements 95
3.4.6 Magnetostriction Studies 96
3.5 Studies on Ball Milled $CoFe_2O_4$ 99
3.5.1 Synthesis 99
3.5.2 Powder XRD Analysis 100
3.5.3 TMA Analysis 100
3.5.4 Microstructural Analysis 102
3.5.5 Magnetic Measurements 103
3.5.6 Magnetostriction Studies 107
3.6 Conclusions 114

4 Magnetostriction Studies on Mn Substituted Cobalt Ferrite 121
4.1 Introduction 121
4.2 Studies on Mn Substituted Cobalt Ferrite 122
4.2.1 Synthesis 123
4.3 $Co_{1-x}Mn_xFe_2O_4$ 124
4.3.1 Powder XRD Analysis 124
4.3.2 TMA Analysis 125
4.3.3 Microstructural Analysis 127
4.3.4 Magnetic Measurements 127
4.3.5 Magnetostriction Studies 131
4.4 Studies on Mn Substituted $Co_{1.2}Fe_{1.8}O_4$ 136
4.4.1 Powder XRD Analysis 136
4.4.2 TMA Analysis 138
4.4.3 Microstructural Analysis 138
4.4.4 Magnetic Measurements 140
4.4.5 Magnetostriction Studies 145
4.5 Conclusions 152

5 Studies on $\mathbf{LaMn_{1-x}Fe_xO_3}$ 157

5.1 Introduction 157

5.2 Synthesis 159

5.3 Powder XRD Analysis 161

5.4 Magnetic Measurements 161

5.5 IR Spectroscopic Studies 166

5.6 Mössbauer Studies on $LaMn_{0.5}Fe_{0.5}O_3$ 168

5.7 Susceptibility studies on $LaMn_{0.5}Fe_{0.5}O_3$ 170

5.8 IR Spectra of $LaMn_{0.5}Fe_{0.5}O_3$ 171

5.9 EPR Studies on $LaMn_{0.5}Fe_{0.5}O_3$ 172

5.10 Discussion 174

5.11 Conclusions 176

List of Tables

1.1 Magnetostriction, anisotropy and Curie temperature of some magnetostrictive materials [43]. 26

3.1 Summary of particle size from XRD (d_{XRD}) and TEM (d_{TEM}), H_c, M_s, Percentage sintered density (D), grain size (G) and magnitude of maximin magnetostriction $\lambda_{\|}$, for the samples synthesized by coprecipitation (CPP), citrate (CIT), combustion (GNP) and ceramic (CER) methods. 98

3.2 Comparison of the Curie temperatures of samples sintered at different temperatures and duration. 107

3.3 Summary of magnitude of maximum magnetostriction $\lambda_{\|}$, H_c and M_s for the samples sintered at various temperatures. 113

4.1 Effective ionic radii for Fe, Co and Mn in the tetrahedral and octahedral coordinations, taken from reference [18]. 123

4.2 Cubic unit cell parameter for the compositions in the $Co_{1-x}Mn_xFe_2O_4$ (CMF) series. 126

4.3 Variation of coercivity, magnetization and Curie temperature of the sintered compositions in the $Co_{1-x}Mn_xFe_2O_4$ (CMF) series. 131

4.4 Summary of $\lambda_{\|}$, $\lambda_{\perp}$, H_{max}, $d\lambda/dH$, λ_t and ω for different compositions in the $Co_{1-x}Mn_xFe_2O_4$ (CMF) series. 136

4.5 Cubic unit cell parameters for different compositions in the $Co_{1.2-x}Mn_xFe_{1.8}O_4$ (CMFO)and $Co_{1.2}Fe_{1.8-x}Mn_xO_4$ (CFMO) series with increasing Mn content. 139

4.6 Summary of magnetization and coercivity for the powder and sintered samples in the $Co_{1.2-x}Mn_xFe_{1.8}O_4$ (CMFO) and $Co_{1.2}Fe_{1.8-x}Mn_xO_4$ (CFMO) series. 143

4.7 Summary of $\lambda_{\|}$, $\lambda_{\perp}$, H_{max}, $d\lambda/dH$, λ_t and ω for different compositions in the $Co_{1.2-x}Mn_xFe_{1.8}O_4$ (CMFO) and $Co_{1.2}Fe_{1.8-x}Mn_xO_4$ (CFMO) series. . 151

List of Figures

1.1 (a) Alignment of magnetic moments in different magnetic materials and (b) variation of the inverse susceptibility with temperature of para-, antiferro- ,ferro- and ferri-magnetic materials. 10

1.2 Basic magnetization process in ferromagnetic materials. 14

1.3 Joule magnetostriction: (A) The change in shape in response to a magnetic field H where H is proportional to the current that passes through the solenoid and (B) Relation between ΔL/L and H. 18

1.4 Mechanism of Magnetostriction. 21

1.5 The Spinel structure. 27

1.6 The two types of octants containing A cations in the tetrahedral (type I) and the B cations in the octahedral (type II) coordination in the unit cell divided into eight small octants. 28

1.7 Structural features of an ideal perovskite, ABO_3. 33

1.8 Structural distortions in perovskites. (a) due to cation size mismatch and (b) due to Jahn-Teller effect 35

1.9 Different types of exchange in manganites.(a) and (b) superexchange (c) double exchange. 37

2.1 Schematic diagram for a Thermo-Mechanical Analyzer. 65

2.2 Schematic diagram of the VSM components. 70

2.3 Schematic diagram of a strain gage. 71

2.4 Different shapes of cobalt ferrite samples used for magnetostriction measurements. 73

3.1 Powder X-ray diffraction patterns for the samples in the $Co_xFe_{3-x}O_4$ series. The simulated pattern is shown and indexed for comparison. 82

3.2 Sintering behavior for the samples in the $Co_xFe_{3-x}O_4$ series. 83

3.3 Room temperature magnetization curves for the samples in the $Co_xFe_{3-x}O_4$ series. . . . 84
3.4 Magnetostriction measured in the direction parallel to the applied field for different compositions in the $Co_xFe_{3-x}O_4$ series. . . . 84
3.5 Comparison of the SEM photographs for the composition $CoFe_2O_4$ sintered at 1100 °C for 8 hours (A) and 1450 °C for 10 minutes (B). . . . 86
3.6 Field dependence of magnetization for the powder and sintered cobalt ferrite. The inset shows the M-T curve recorded for the sintered sample. . . . 87
3.7 Magnetostriction curves of $CoFe_2O_4$ sintered at 1450 °C for 10 minutes, measured in the parallel and perpendicular directions. . . . 87
3.8 X-ray diffraction patterns of the samples synthesized by the low-temperature routes along with the one synthesized by the ceramic process. . . . 90
3.9 Sintering behavior of cobalt ferrite prepared by different methods. . . . 91
3.10 SEM photographs of the powders prepared by (A) citrate method, (B) coprecipitation method, (C) combustion method and (D) ceramic method. 93
3.11 Transmission electron micrographs of cobalt ferrite prepared by (A) citrate, (B) coprecipitation and (C) combustion methods and (D) SEM photograph of the powder synthesized by the ceramic method. . . . 93
3.12 SEM photographs of the sintered samples synthesized by (A) citrate, (B) coprecipitation, (C) combustion, and (D) ceramic methods. . . . 94
3.13 Variation of magnetization as a function of temperature (left) and magnetic field at room temperature, for the samples synthesized by the low-temperature and ceramic routes. . . . 95
3.14 Magnetostriction as a function of magnetic field recorded in the parallel direction to the applied magnetic field. . . . 96
3.15 Magnetostriction as a function of magnetic field recorded in the perpendicular direction to the applied magnetic field. . . . 97
3.16 Powder XRD pattern of ball milled cobalt ferrite and the simulated pattern for cobalt ferrite. . . . 101

3.17 Sintering behavior of the ball milled powder (solid line) and powder prepared from standard ceramic technique (dashed line) recorded using TMA. Inset shows the density of the sintered pellets as a function of temperature. 101
3.18 Scanning electron micrograph of the cobalt ferrite powder ball milled for 8 hours. 102
3.19 Scanning electron micrographs of the samples sintered at various temperatures for different dwell times. 104
3.20 Scanning electron micrographs of the samples sintered at 1100 °C for 8 h, with the presence of 1% additives, (A) TiO_2, (B) no additive (C) Y_2O_3, and (D) Nb_2O_5. 105
3.21 Room temperature magnetization curves for the samples sintered at various temperatures as indicated. 106
3.22 Variation of magnetization (at 15 kOe) and coercivity as a function of sintering temperature for different dwell times. 108
3.23 Temperature dependence of magnetization for the samples sintered at different temperatures. 108
3.24 Magnetostriction curves recorded in the parallel direction to the applied magnetic field for samples sintered at different temperatures, as indicated. 109
3.25 Magnetostriction curves recorded in the perpendicular direction to the applied magnetic field for different samples. 110
3.26 Variation of maximum magnetostriction and slope of magnetostriction as a function of the sintering temperature. 112
3.27 Magnetostriction as a function of magnetic field for the samples with Nb_2O_5, Y_2O_3 and TiO_2 as additives and without additive (CFBM). 113
4.1 X-ray diffraction patterns for different compositions in the $Co_{1-x}Mn_xFe_2O_4$ series. 124
4.2 The variation of the unit cell parameter with Mn concentration in the $Co_{1-x}Mn_xFe_2O_4$ (CMF) series. 125
4.3 Sintering behavior of the compositions in the $Co_{1-x}Mn_xFe_2O_4$ (CMF) series. 126

4.4 Scanning electron micrographs for different compositions in the $Co_{1-x}Mn_xFe_2O_4$ (CMF) series. (A) $CoFe_2O_4$ (B) $Co_{0.9}Mn_{0.1}Fe_2O_4$ (C) $Co_{0.8}Mn_{0.2}Fe_2O_4$ (D) $Co_{0.7}Mn_{0.3}Fe_2O_4$ and (E) $Co_{0.6}Mn_{0.4}Fe_2O_4$. 127

4.5 Magnetization as a function of magnetic field for the compositions in the $Co_{1-x}Mn_xFe_2O_4$ (CMF) series. 128

4.6 Temperature variation of magnetization for the compositions in the $Co_{1-x}Mn_xFe_2O_4$ (CMF) series. 129

4.7 Variation M_s, H_c, and T_C as a function of Mn concentration in the $Co_{1-x}Mn_xFe_2O_4$ (CMF) series. The values shown for $CoFe_{2-x}Mn_xO_4$ are from reference [13]. 130

4.8 Magnetostriction curves recorded in the parallel direction ($\lambda_{\parallel}$) as a function of magnetic field for different compositions in the $Co_{1-x}Mn_xFe_2O_4$ (CMF) series. 132

4.9 Magnetostriction curves recorded in the perpendicular direction ($\lambda_{\perp}$) as a function of magnetic field for different compositions in the $Co_{1-x}Mn_xFe_2O_4$ (CMF) series. 133

4.10 Variation of λ at different low fields and λ_{max} as a function of Mn concentration in $Co_{1-x}Mn_xFe_2O_4$. 133

4.11 Variation of volume (ω) and anisotropic strain (λ_t) for the compositions in the $Co_{1-x}Mn_xFe_2O_4$ (CMF) series. 135

4.12 Variation of slope of the magnetostriction curve and H_{max} for the measurements in the parallel (open symbols) and perpendicular (closed symbols) directions for the compositions in the $Co_{1-x}Mn_xFe_2O_4$ (CMF) series. . . . 135

4.13 Powder X-ray diffraction patterns for different compositions in the $Co_{1.2-x}Mn_xFe_{1.8}O_4$ (CMFO) and $Co_{1.2}Fe_{1.8-x}Mn_xO_4$ (CFMO) series. 137

4.14 Variation of the cubic lattice parameter with Mn content for different compositions in the $Co_{1.2-x}Mn_xFe_{1.8}O_4$ (CMFO) and $Co_{1.2}Fe_{1.8-x}Mn_xO_4$ (CFMO) series. 138

4.15 Sintering behavior of $Co_{1.2}Fe_{1.8}O_4$, and $Co_{1.1}Mn_{0.1}Fe1.8O_4$ compared with $CoFe_2O_4$. 139

4.16 Comparison of the SEM micrographs of (A) $Co_{1.2}Fe_{1.8}O_4$, (B) $Co_{1.1}Mn_{0.1}Fe_{1.8}O_4$, (C) $Co_{0.9}Mn_{0.3}Fe_{1.8}O_4$, (D) $Co_{1.2}Fe_{1.7}Mn_{0.1}O_4$, and (E) $Co_{1.2}Fe_{1.5}Mn_{0.3}O_4$. . 140

4.17 Room temperature magnetization curves for the powder samples in the $Co_{1.2-x}Mn_xFe_{1.8}O_4$ (CMFO) and $Co_{1.2}Fe_{1.8-x}Mn_xO_4$ (CFMO) series. 141

4.18 Room temperature magnetization curves for the sintered samples in the $Co_{1.2-x}Mn_xFe_{1.8}O_4$ (CMFO) and $Co_{1.2}Fe_{1.8-x}Mn_xO_4$ (CFMO) series. 141

4.19 Variation of magnetization and coercivity for the powder (a) and sintered (b) samples in the $Co_{1.2-x}Mn_xFe_{1.8}O_4$ (CMFO) and $Co_{1.2}Fe_{1.8-x}Mn_xO_4$ (CFMO) series with increasing Mn concentration. 142

4.20 Temperature dependence of magnetization for different compositions in the $Co_{1.2-x}Mn_xFe_{1.8}O_4$ (CMFO) and $Co_{1.2}Fe_{1.8-x}Mn_xO_4$ (CFMO) series. 144

4.21 Variation of Curie temperature with Mn concentration for the compositions in the $Co_{1.2-x}Mn_xFe_{1.8}O_4$ (CMFO) and $Co_{1.2}Fe_{1.8-x}Mn_xO_4$ (CFMO) series. 145

4.22 Magnetostriction measured parallel to the field direction, as a function of field, for the different compositions in the $Co_{1.2-x}Mn_xFe_{1.8}O_4$ (filled symbols) and the $Co_{1.2}Fe_{1.8-x}Mn_xO_4$ (open symbols 146

4.23 Magnetostriction measured perpendicular to the field direction, as a function of field, for the different compositions in $Co_{1.2-x}Mn_xFe_{1.8}O_4$ (CMFO) (filled symbols) and $Co_{1.2}Fe_{1.8-x}Mn_xO_4$ (CFMO)(open symbols). 147

4.24 Variation of the magnitude of maximum magnetostriction as a function of Mn concentration in $Co_{1.2-x}Mn_xFe_{1.8}O_4$ (CMFO) and $Co_{1.2}Fe_{1.8-x}Mn_xO_4$ (CFMO). 148

4.25 The variation of volume (ω) and anisotropic strain (λ_t) with Mn concentration for the samples in the $Co_{1.2-x}Mn_xFe_{1.8}O_4$ (CMFO) and $Co_{1.2}Fe_{1.8-x}Mn_xO_4$ (CFMO) series. 149

4.26 The variation of the magnetic field H_{max} at which maximum magnetostriction is obtained, as a function of Mn concentration in $Co_{1.2-x}Mn_xFe_{1.8}O_4$ (CMFO) and $Co_{1.2}Fe_{1.8-x}Mn_xO_4$ (CFMO) series. 150

4.27 The Variation of the initial slope of magnetostriction (dλ/dH) with field as a function of Mn concentration for different compositions in the CMFO and CFMO series. 152

5.1 Powder XRD patterns of different compositions in the $LaMn_{1-x}Fe_xO_3$ series annealed at (c) 200 °C, (b) 700 °C and (c) 1300 °C. The simulated XRD pattern of $LaFeO_3$ (LFO) is shown and indexed for comparison. 160
5.2 Variation of the orthorhombic lattice parameters as a function of Mn concentration in the $LaMn_{1-x}Fe_xO_3$ series for samples annealed at (a) 200 °C, (b) 700 °C and (c) 1300 °C. 162
5.3 ZFC magnetization (H = 50 Oe) curves of different compositions in $LaMn_{1-x}Fe_xO_3$ series annealed at (a) 200 °C, (c) 700 °C and (d) 1300 °C. (b) shows the normalized magnetization curves of the samples annealed at 200 °C. 163
5.4 Magnetic field dependence of magnetization recorded at 12 K for different compositions in the $LaMn_{1-x}Fe_xO_3$ series annealed at (a) 200 °C, (b) 700 °C and (c) 1300 °C. 164
5.5 IR spectra of different compositions in $LaMn_{1-x}Fe_xO_3$ series annealed at (a) 200 °C, (b) 700 °C and (c) 1300 °C. 167
5.6 Room temperature Mössbauer spectra of $LaMn_{0.5}Fe_{0.5}O_3$ annealed at a) 200 °C, b) 700 °C and c) 1300 °C. 169
5.7 Temperature variation of the inverse of the magnetic susceptibility of LMF200, LMF700, and LMF1300. 170
5.8 IR spectra of $LaMn_{0.5}Fe_{0.5}O_3$ annealed at a) 200 °C, b) 700 °C and c) 1300 °C. 172
5.9 EPR spectra of $LaMn_{0.5}Fe_{0.5}O_3$ at 300 K, for samples annealed at different temperatures. Inset, comparison of the EPR spectra of LMF700 and $La_{0.7}Ca_{0.3}MnO_3$ (LCM). 173

List of abbreviations

AFM: Antiferromagnetism
bcc: Body Centered Cubic
DMS: Diluted Magnetic Semiconductor
emu: Electromagnetic Unit
eV: Electron Volt
EPR: Electron Paramagnetic Resonance
FC: Field Cooled
fcc: Face Centered Cubic
FM: Ferromagnetism
GMR: Giant Magnetoresistance
GNP: Glycine-Nitrate-Process
$\mathbf{H}_c$: Coercivity
HMF: Hyperfine Magnetic Field
IS: Isomer Shift
IR: Infra-red
JCPDS: Joint Committee on Powder Diffraction Standards
K: Kelvin
μ_B: Bohr Magneton
M: Magnetization
$\mathbf{M}_s$: Saturation magnetization
Oe: Oersted
PCW: Powder Cell for Windows
PDP: Powder Diffraction Package
PVA: Polyvinyl Alcohol
SEM: Scanning Electron Microscopy
TEM: Transmission Electron Microscopy
TGA: Thermo-Gravimetric Analysis
TMA: Thermal Mechanical Analysis
T: Temperature
$\mathbf{T}_C$: Curie Temperature
TMA: Thermal Mechanical Analyzer
VSM: Vibrating Sample Magnetometer
XPS: X-ray Photoelectron Spectroscopy
XRD: X-Ray Diffraction
ZFC: Zero Field Cooled

Abstract

Magnetic materials are widely used in different technological applications like, power generation, communication, data storage and retrieval, sensors etc. Continuous efforts by many researchers during the past many decades have led to the discovery of many novel magnetic materials and properties like high-T_C oxide superconductors, giant and colossal magnetoresistive materials, giant magnetostrictive materials, etc. Magnetostriction is the change in dimensions of a magnetic material when it is subjected to a magnetic field. The phenomenon is reversible in the sense that an applied stress can led to a change in the magnetic state of the magnetostrictive material. This reversible effect gives magnetostrictive materials a special place among the existing smart materials. It is important to develop different alternatives to the existing materials with reduced cost, easy manufacturing and enhanced properties. Oxide based magnetic materials are suitable alternatives to the existing alloy based materials.

Substituted lanthanum manganites came into limelight after the discovery of colossal magnetoresistance in this class of oxides. $LaMnO_3$ belongs to the family of perovskites having the general formula ABO_3. The magnetic properties of $LaMnO_3$ can be altered by substituting suitable metal ions in the A-site and/or in the B-site of the perovskite lattice. Also, the magnetic properties are very much sensitive to the spin states of the ions present in the B-site of the perovskite lattice. For example, it is known that substitution of Cr, Co and Ni makes the antiferromagnetic $LaMnO_3$ ferromagnetic whereas substitution of Mn by Fe does not similar effects, though the opposite is expected. Hence it is very much desirable to understand the role of Fe in determining the magnetic properties of the substituted compositions.

The work presented in the part-I (chapter 3 and 4) of the thesis is focused towards the understanding of the various aspects related to the development of the cobalt ferrite based magnetostrictive materials. Part-II (chapter 5) of this thesis is on the studies on the processing dependent magnetic properties of the Fe substituted lanthanum manganite.

The first chapter is a brief introduction to magnetism and magnetostriction and a review of the structural and magnetic properties of the different magnetic materials used in the present study such as spinel ferrites and perovskite manganites. Special emphasis has been give on the magnetostrictive behavior of these materials.

The second chapter describes the method employed for the synthesis of the ferrite and perovskite materials studied in the present work. All the experimental methods and characterization techniques used are briefly discussed in the specific sections.

Synthesis procedures of cobalt ferrite in the bulk as well as nanocrystalline forms and its structural, magnetic and magnetostrictive properties are discussed in the third chapter. The nanocrystalline materials having particle sizes in the range of 10 to 50 nm are synthesized by different low temperature methods of synthesis. The magnetostriction studies carried out on these materials have shown that sintered cobalt ferrite obtained from powders synthesized in the nanocrystalline form exhibit enhanced magnetostriction. The studies reveled the importance of microstructural control in determining in the magnetostrictive strain of cobalt ferrite. Another part of this chapter involves studies on the effect of sintering temperature and time on the magnetostriction of ball milled cobalt ferrite. These studies also reveled that it is necessary to control the microstructure and the presence and small sized and uniform grains can lead to enhancement of the magnetostrictive strain.

Studies on the structural, magnetic, and magnetostrictive properties of Mn substituted cobalt ferrite are discussed in the fourth chapter. The effect of substitution of Fe and Co in cobalt ferrite by Mn is studied in detail on the magnetostrictive properties of two compositions $Co_{1.2}Fe_{1.8}O_4$ and $CoFe_2O_4$. A strong dependence of magnetostriction on the Mn content is observed in both cases. The substitution of Co by Mn enhances the magnetostriction for small values of x in $Co_{1.2-x}Mn_xFe_{1.8}O_4$ whereas magnetostriction decreases continuously with increasing x in $Co_{1.2}Fe_{1.8-x}Mn_xO_4$. A two fold increase in the initial slope $d\lambda/dH$, with large magnetostriction as compared to that of the unsubstituted compound, is observed when small amounts of Co is replaced by Mn. Similarly, the field at which maximum magnetostriction is obtained is also reduced by 50% by this substitution. The magnetostriction parallel to the applied field direction decreases with increasing Mn content, whereas the magnetostriction perpendicular to the field showed a marked increase for 10% of the Mn substitution. The observed magnetostrictive properties are correlated with the magnetic properties. The results suggest the possibility of tuning the magnetostrictive properties of cobalt ferrite for various applications by proper substitution.

The fifth chapter deals with studies on the structural and magnetic properties of $\mathrm{LaMn}_{1-x}\mathrm{Fe}_x\mathrm{O}_3$ ($0.0 \leq \mathrm{x} \leq 0.5$). The synthesis carried out by an autocombustion method gave single phase nanocrystalline powders. The magnetic properties of these powders were studied after annealing to various temperatures. Interesting modifications in the magnetic properties are obtained on heat treatment. The introduction of Fe weakens the ferromagnetic interactions and the composition with $x = 0.5$, show peculiar magnetic behavior indicating the presence of ferromagnetic clusters. The magnetic properties have been described on the basis of formation of clusters involving Mn^{3+} and Fe^{3+} and the degree of distribution of these clusters is sensitive to heat treatment at different temperature which in turn reflects in the magnetic behavior.

Chapter 1

Introduction

1.1 Materials Science

The progress of human civilization has been indexed based on the progress in the field of materials science. Materials science is an extremely interdisciplinary subject involving different branches such as physics, chemistry, engineering, biology, etc. The variety of different subjects such as thermodynamics, crystallography, solid state physics, polymer science, biochemistry, etc can be brought under one umbrella of materials science. New branches are still evolving with the advent of knowledge in materials science. Nanotechnology is one such example. Materials science is one of the oldest form of engineering and applied science. Understanding the basic aspects of a variety of materials such as their structure and properties are the key issues in materials science. Based upon the fundamental understanding of structure-property relationship, new materials with enhanced performance are currently being developed.

Materials can be classified depending upon their interaction with the surrounding.

Functional Materials: These materials perform a particular function for a specific application depending upon their crystallographic or electronic features. *e.g.* semiconductors, magnetic materials, etc.

Structural Materials: These materials are basically important because of their mechanical properties and other features are not much relevant.*e.g.* steel, plastic, rubber, etc.

Smart materials: This class of materials respond to their surrounding in a two way manner. They can sense the changes happening in their surrounding and send a feed back signal to take an appropriate action. These materials are also termed as intelligent materials. *e.g.* piezoelectric materials, shape memory alloys, magnetostrictive materials, magneto-rheological fluids, etc.

1.2 Magnetic Materials

Magnetic materials are all around us. The advent of the field of magnetism is mainly because of the dedicated efforts from many people who have contributed to the basic and fundamental understanding of this beautiful phenomenon. The progress in magnetic materials has come a far way from the age old knowledge of lodestone by our ancestors. Magnetic materials find a lot of applications in many present day technologies. The magnetic properties such as magnetization, coercivity and remanence determine the possibility of using a magnetic material for a particular application. Magnetic materials in different forms can be used such as oxides and alloys. Magnetic materials have found applications in almost all areas related to our day to day life. The permanent magnets such as AlNiCo, hard ferrites, Sm-Co magnets, Nd-Fe-B magnets, etc find variety of industrial applications. Soft magnetic materials, with high saturation magnetization, larger permeability and very small energy dissipation find a lot of applications in the electrical engineering and power electronics, used in the production, transportation and use of the electrical energy. The soft magnetic materials are also used in telecommunication and electronics [1]. Magnetic materials have also been used in magnetic field screening, permanent magnets for loudspeakers, generators, analog data storage in video as well as audio tapes, digital data storage in ferrite memory core, drum hard disc, floppy disc, etc. The recent advances in the field of magnetism have shown bright future for many materials to be used in advance technologies such as giant magnetoresistive materials to be used in GMR read head and MRAMS. Diluted magnetic semiconductors (DMS), which are a remarkable class of materials where magnetic ions are incorporated in a semiconductor host lattice [2–4] to be used in spintronics or magnetoelectronics where both the spin and charge of electrons are made use of [5, 6]. Thus, magnetic materials have been an indispensable part of technological revolution and will continue to play a leading role in forthcoming technologies.

1.3 Magnetism in Materials

All materials are magnetic in nature [7]. The magnetic properties arise mainly due to the electrons present in the atom, which have small magnetic moment by virtue of their motion. Nucleus also has a small magnetic moment, but it is insignificant to that of the electrons and it does not affect the gross magnetic properties.

1.3.1 Magnetic Moments of Electrons

There are two kinds of electron motions namely the orbital and the spin motion and each has a magnetic moment associated with it. The orbital motion of an electron is similar to the current in a loop of wire without resistance, and both are equivalent to the circulation of charge. Therefore, the magnetic moment of an electron due to its orbital motion is given by,

$$\mu = (\text{area of loop})/(\text{current in emu})$$

If e is the charge on the electron in *esu* and c is velocity of light, then e/c is the charge in *emu*. The current or charge passing through a given point per unit time is thus

$$((e/c)(v/2\pi r)) \tag{1.1}$$

Therefore,

$$\mu_{orbit} = \pi r^2 \left(\frac{ev}{2\pi rc}\right) = \frac{evr}{2c} \tag{1.2}$$

The angular momentum of an electron is given by,

$$mvr = nh/2\pi \tag{1.3}$$

Combining these equations, we have the orbital magnetic moment for an electron in the first Bohr orbit,

$$\mu_{orbit} = eh/4\pi mc \tag{1.4}$$

Spin is a universal property of electrons in all states of matter at all temperatures. The electrons behave as if they were spinning about its own axis, as well as moving in an orbit about the nucleus and associated with this spin are definite amounts of magnetic moments and angular momentum. The magnetic moment due to electron spin is equal to,

$$\mu_{spin} = \frac{eh}{4\pi mc} \tag{1.5}$$

where e is the charge on the electron, h is Planck's constant, m is the mass of an electron and c is the velocity of light. Substituting all the values in above equation , the magnetic moment due to the spin and orbital motion of electrons are found to be qual to 0.927×10^{-20} erg/Oe. Because it is such a fundamental quantity, this amount of magnetic moment is given a special symbol μ_B and is called as Bohr magneton.

There are some fundamental concepts associated with the field of magnetism. Magnetic moment is one such term. The magnetic moment is defined as, in a uniform magnetic field H, if a magnetic pole of strength p is placed at an angle θ to another pole and separated by a distance l, then a couple acts on the magnet moment m and is given by,

$$m = pHsin\theta(l/2) + pHsin\theta(l/2) = (pHsin\theta) \tag{1.6}$$

If $H = 1$ Oe and $\theta = 90$ °,

$$m = pl \tag{1.7}$$

The magnetic moment per unit volume is called intensity of magnetization or simply magnetization and is given by,

$$M = \frac{m}{V} \tag{1.8}$$

where V is the volume of the material. The specific magnetization is defined as,

$$\sigma = \frac{m}{W} = \frac{m}{v\rho} = \frac{M}{\rho} emu/g \tag{1.9}$$

where W is the mass and ρ is the density of the material. The magnetic properties of a material are characterized not only by the magnitude and sign of M, but also by the way in which M varies with H.

The magnetization per unit magnetic field is called the magnetic susceptibility(χ).

$$\chi = \frac{M}{H} = emu/cm^3 Oe \tag{1.10}$$

χ is also called the volume susceptibility. Depending on the values and order of susceptibility, substances have been classified into different categories. The most important ones are paramagnetism, ferromagnetism, ferrimagnetism, antiferromagnetism and superparamagnetism [7,8].

1.3.2 Diamagnetism

Diamagnetism is associated inherently with all the materials. Diamagnetism originates from the interaction of the paired electron which are lying in the inner shells of a material. Their magnetization induced by the filed is very weak, and is opposite to the applied field direction. This form of magnetism originates from the change in the electronic orbital motion under the influence of an applied magnetic field. According to Lenz's law, the induced currents give rise to an induced magnetic flux, which is in the opposite direction to the applied magnetic field. Diamagnetism is present in all the magnetic materials, but it is masked because of the contribution from the magnetic atoms. Diamagnetic materials have negative susceptibilities of the order of 10^{-6} which for practical purposes are independent of temperature.

1.3.3 Paramagnetism

The magnetism of paramagnetic substances originates from the permanent magnetic moment associated with some or all of the constituent atoms. If these moments have negligible interactions with each other, then they can orient themselves freely in any direction. This is called paramagnetism of free atoms. A paramagnetic substance is the one which has a net magnetic moment associated with its constituent atoms. On applying a magnetic field, the average direction of the moments is modified and an induced magnetization parallel to the field appears. This magnetization is lower, the higher the temperature. With increasing temperature the variation of magnetization as a function of field becomes more and more linear. In 1895, the French Physicist Pierre Curie first reported about the variation of paramagnetic susceptibilities with temperature. He stated that, mass

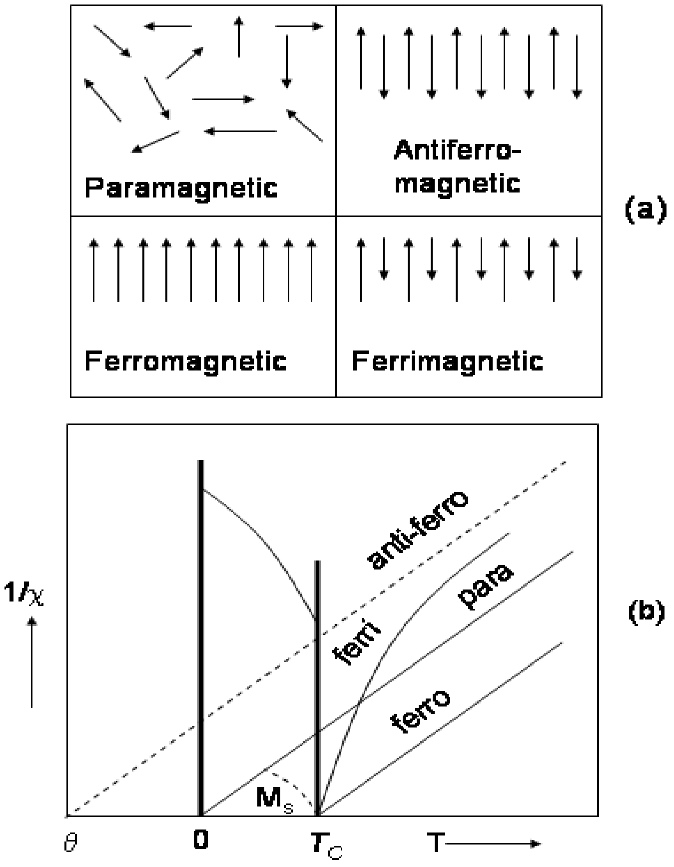

Figure 1.1: (a) Alignment of magnetic moments in different magnetic materials and (b) variation of the inverse susceptibility with temperature of para-, antiferro-,ferro- and ferrimagnetic materials.

susceptibility of a paramagnetic substance varies inversely with the absolute temperature and this is mathematically given by,

$$\chi = \frac{C}{T} \tag{1.11}$$

This equation is known as Curie's law, where C is the Curie constant. The effective magnetic moment μ_{eff} is directly related to the number of unpaired electrons present.

$$\mu_{eff} = g[J(J+1)]^{1/2}\mu_B \tag{1.12}$$

The relationship between χ and effective magnetic moment μ_{eff} is given by,

$$\chi = \frac{N\beta^2\mu_{eff}^2}{3kT} \tag{1.13}$$

where, N is Avogadro's number, β is the Bohr magneton and k is Boltzmann's constant. Substitution for N, β and K gives,

$$\mu_{eff} = \sqrt{8C} = 2.828\sqrt{C} \tag{1.14}$$

When the orbital angular momentum is quenched L = 0 and therefore J = S, as in the case for most transition metal ions. The effective magnetic moment is contributed by the spin components only and is given by,

$$\mu_{eff} = 2\sqrt{S(S+1)} \tag{1.15}$$

The alignment of magnetic moments and the variation of the paramagnetic susceptibility with temperature is shown in figure 1.1.

1.3.4 Ferromagnetism

Ferromagnetism is the most important property of magnetic materials. The ordering of the atomic magnetic moments is mainly governed by the magnetic exchange interactions [7, 9–11]. Ferromagnetism is exhibited by certain metals, alloys, and compounds of the transition metal ions (iron group, rare earth elements in which, below a certain temperature called the Curie temperature, the magnetic moments prefer to align in a common direction. In a ferromagnetic substance, in regions called as magnetic domains, all the magnetic moments are essentially aligned giving a net magnetic moment even in absence of an external magnetic field. Ferromagnetic materials behave like paramagnets above the T_C. In Curies law, it is assumed that individual magnetic moments do not interact with each other, but acted only by the applied magnetic field and thermal agitation. But Curie's law was modified by Weiss in 1907 for ferromagnetic materials. Weiss modified this law by employing the idea of a molecular field 'H_m'. This term is the internal field inside a material and acted in addition to the applied field H. Thus,

$$H_m = \gamma M \tag{1.16}$$

where γ is called the molecular field constant. Therefore, the total field in the material

$$H_t = H + H_m \tag{1.17}$$

Solving for these equations and Curie's law, Weiss postulated that

$$\chi = \frac{M}{\rho H} = \frac{C}{T - \rho C \gamma} = \frac{C}{T - \Theta} \tag{1.18}$$

This equation is known as the Curie-Weiss law, where Θ is called as Weiss constant and is a measure of the strength of the magnetic interactions. For substances obeying Curie's law, $\Theta = \gamma = 0$. The alignment of the magnetic moments and the temperature variation of the susceptibility of a ferromagnetic material is shown in figure 1.1.

1.3.5 Antiferromagnetism

In antiferromagnetic materials the magnetic moments on the adjacent atoms orient align opposite directions to each other, thereby leading to a net zero magnetic moment associated with the bulk material. They have small positive susceptibility at all temperatures, but their susceptibilities varies in a peculiar way with temperature. The theory of antiferromagnetism was developed by Neel [12]. Below a characteristic temperature , called as Neel temperature, T_N, the two sublattice undergo spontaneous magnetic ordering as in case of ferromagnetic materials, but the net magnetization is zero because of the opposing directions of the sublattices magnetizations. Under the influence of an externally applied magnetic field, a small net magnetization can be detected. Above the Neel temperature, antiferromagnetic materials behave like paramagnets. The alignment of the magnetic moments and the temperature variation of susceptibility of an antiferromagnetic material are shown in figure 1.1.

1.3.6 Ferrimagnetism

Ferrimagnetism is a phenomenon in which there is partial cancellation of the adjusting magnetic moments. Ferrimagnetism is also called as uncompensated antiferromagnetism. Ferrimagnetic materials behave like paramagnetic materials above T_C and can retain spontaneous magnetization below the Curie temperature like ferromagnetic materials. The general theory of ferrimagnetism was developed by Neel. The uncompensated sublattice magnetization give a way to have ferrimagnetic materials with different magnetic characteristics. The temperature dependencies of magnetic moments on the two sublattices are different. So, the magnetization may even change sign with changing temperature. The temperature, at which the sublattice magnetizations just cancel, is called T_{comp}.

1.3.7 Superparamagnetism

When the particle size of a magnetic material is reduced below a critical size limit, the thermal energy is not sufficient to overcome the coupling forces between the atoms, but is sufficient to change the direction of magnetization of the entire particle. This results in a fluctuating magnetization causing the magnetic moments to average to zero [13]. Thus the material behaves in a similar manner to paramagnetism, except that instead of each individual atom being independently influenced by an external magnetic field, the moment of the entire particle is aligned with the field. These particles are called superparamagnetic. Superparamagnetism occurs when the particle size is generally in between 1-10 nm. This is particularly important in the magnetic data storage technology, where the superparamagnetic effect limits the minimum size of the particles that can

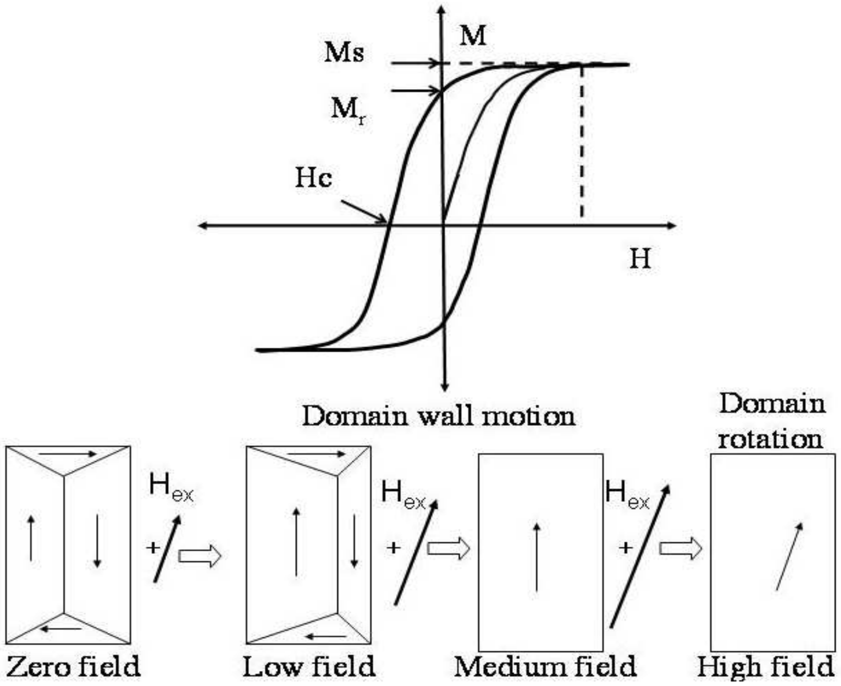

Figure 1.2: Basic magnetization process in ferromagnetic materials.

be used [14]. There are some other commercialized applications of superparamagnetic particles such as in magnetic resonance imaging(MRI), cell, DNA and protein separation, RNA fishing, targeted drug delivery, magnetic hyperthermia, magnetofaction, tunable viscosity (ferrofluid), high sensitivity sensors (GMR) etc [15–18].

1.3.8 Magnetization Process

The basic magnetization process in ferromagnetic materials is shown in figure 1.2. Any ferromagnetic or ferrimagnetic material that is at a temperature below the Curie temperature or T_C, is composed of small volume regions in which there is a mutual alignment of all the magnetic moments in the same direction. Such a region is called a domain and each domain is magnetized to its saturation magnetization. Adjacent domains are separated by domain boundaries or walls across which the direction of magnetization gradually changes. Normally domains are microscopic in size, and for a polycrystalline specimen, each grain may consist of more than a single domain. Thus, in a macroscopic piece of material, there will be a large number of domains, and all may have a different magnetization orientation. The magnitude of the magnetic field for the entire solid is the vector sum of magnetizations of all the domains. The domains are formed in order to reduce the overall magnetostatic energy of the system and are separated from one another by domain or *Bloch* walls which are high energy areas defined as transition layer that separates adjacent regions magnetized in different directions. The presence of this domain walls and their mobility both reversibly and irreversibly are directly responsible for magnetic hysteresis loop. For a ferromagnetic material, the field dependence of magnetization is nonlinear and at large values of H, the magnetization M becomes constant and reaches a saturation value called as M_s. However, once saturated, the reversal of magnetic field to zero does not bring the magnetization M, to zero. It still possesses a finite magnetization called as remnant magnetization (M_R). In order to bring the remnant magnetization to zero, a reverse field is required. The magnitude of this field is called coercivity (H_c). The M-H curve in the case of ferro/ferrimagnetic materials is called as hysteresis loop. The values of M_s, M_R and H_c determine the magnetic nature of the material. The hysteresis loop represents the energy loss during the process of magnetization and demagnetization. During one complete cycle, this amount of energy (the hysteresis loss) is proportional to the area inside the loop.

1.3.9 Magnetic Exchange Interactions

The long range ordering of the magnetic moments, exhibited by magnetic materials arises because of the different type of exchange interactions present in these materials. There are three main type of exchanges namely, dipole exchange, superexchange and the double exchange [19]. The exchange energy forms an important part of the total energy of many molecules and of the covalent bond in many solids. In a many electron system of crystal, the exchange energy between atoms i and j having total spins S_i and S_j, is given by the hamiltonian,

$$H_{ex} = -\sum_{ij} J_{ij} S_i . S_j \tag{1.19}$$

where, J_{ij} is the effective exchange integral between atoms i and j having total spins S_i and S_j. If J_{ij} is positive, H_{ex} is minimum when spins are parallel (ferromagnetic) and a maximum when they are anti-parallel (antiferromagnetic). A positive value of exchange integral is a necessary condition for ferromagnetism to occur.

$$-J_{ex} - \sum_{ij} S_i . S_j = -2zJ_{ex}S^2 \tag{1.20}$$

where z is the number of nearest neighbours.

From the Weiss field model, the relation between J_{ex} and T_C is give by [19],

$$J_{ex}/kT_C = 3/[2zS(S+1)] \tag{1.21}$$

In the case of metal oxides, the magnetic exchange forces are mediated via the oxygen atoms, and therefore the direct exchange is not possible. The two important coupling interactions are the 90° and the 180° *cation-anion-cation* superexchange. Here, the anion orbital mediate the exchange and the cation-anion-cation bond angle is either 90° or 180° and hence the name. Depending upon the nature of the e_g orbitals (considering an octahedral crystal field) of cations, the coupling results in different types of magnetic ordering. If both the e_g are half filled, it leads to antiferromagnetic alignment whereas one half filled and other empty leads to ferromagnetic alignment. The sign of the superexchange interaction can determined by using the Goodenough-Kanamori rules [19].

1.3.10 Magnetic Anisotropy

The magnetic properties of materials are strongly affected by one important property, called as magnetic anisotropy. This term simply means that the magnetic properties depend on the directions in which they are measured. There are several kinds of magnetic anisotropy such as, crystal anisotropy, shape anisotropy, stress anisotropy and exchange anisotropy. Anisotropy can also be induced by magnetic annealing, plastic deformation etc. Of these, the crystal anisotropy is intrinsic to the material. In crystalline materials the preferred directions of magnetization are called as magnetic easy axis or preferred axis. Because the applied magnetic field must do work against the anisotropy force to turn the magnetization away from the easy direction, there must be anergy stored in any crystal in the magnetization points in a non-easy direction. The anisotropy energy is defined as the amount of energy required to rotate the magnetization from a preferred or "easy" direction to a so called "hard" direction. Or in other words, crystal anisotropy can be regarded as a force which tends to bind the magnetization to directions of certain forms in the crystal [7]. In a cubic crystal, if magnetization, M_s, makes angles a, b, c with the crystal axes, and α_1, α_2 and α_3 be the cosines of these angles then, the anisotropy energy E, is given by,

$$E = K_0 + K_1(\alpha_1^2\alpha_2^2 + \alpha_2^2\alpha_3^2 + \alpha_3^2\alpha_1^2) + K_2(\alpha_1^2\alpha_2^2\alpha_3^2) + ... \tag{1.22}$$

where K_0, K_1, K_2,.. are constants for a particular material and are expressed in erg/cm^3. Higher powers are generally not needed and sometimes K_2 is so small the terms involving it can be neglected.

In the case of hexagonal crystals, the hexagonal *c* axis is the direction of easy magnetization, and any direction in the basal plane is equally hard. Therefore, the anisotropy energy E, depends on only a single angle α between the magnetization M_s, and the *c* axis and is given by,

$$E = K_0 + K_1 sin^2\theta \tag{1.23}$$

The anisotropy energy is strain dependent so that anisotropy and magnetostriction of materials are related.

1.4 Magnetostriction

When a substance is exposed to a magnetic field, its dimensions change. This effect is called as magnetostriction. The nature of this effect is shown in figure 1.2. It was discovered by Joule in 1842, who found that an iron rod increases in length when it was

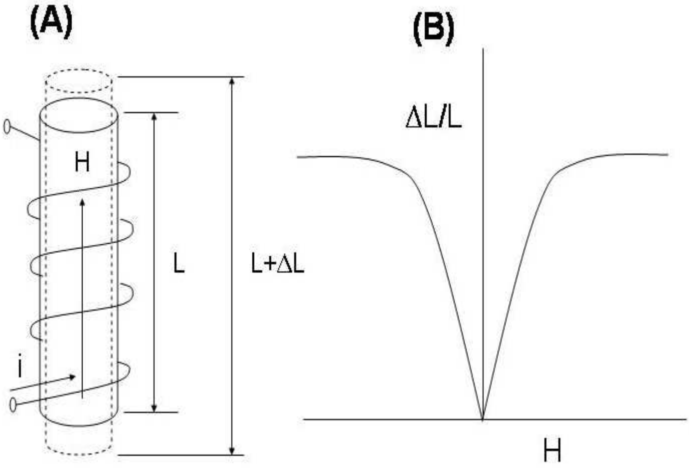

Figure 1.3: Joule magnetostriction: (A) The change in shape in response to a magnetic field H where H is proportional to the current that passes through the solenoid and (B) Relation between ΔL/L and H.

magnetized lengthwise [20]. Since the discovery of magnetostriction by Joule, there has been continuous research activities in this field and development of devices based on this effect. Magnetic anisotropy plays an important role in the magnetostriction of materials. A crystal deforms spontaneously, to lower the anisotropy energy. On the other hand very high anisotropy of a material may act as an obstacle. In this case a much higher magnetic field is required to have larger magnetostrictive strains. The fractional change in length ΔL/L is simply a strain and to distinguish it from the strain ϵ, it was given a special symbol λ.

$$\lambda = \frac{\Delta L}{L} \tag{1.24}$$

Since magnetostriction arises from the anisotropic energy, it is anisotropic and is different in different directions. The anisotropic magnetostriction in a cubic single crystal is given by [21],

$$\lambda_s = \frac{3}{2}\lambda_{100}({\alpha_1}^2{\beta_1}^2 + {\alpha_2}^2{\beta_2}^2 + {\alpha_3}^2{\beta_3}^2 - \frac{1}{3}) + 3\lambda_{111}(\alpha_1\alpha_2\beta_1\beta_2\alpha_2\alpha_3\beta_2\beta_3) \tag{1.25}$$

where α and β are the direction cosines of the magnetization and strain measurements relative to the crystal axes, respectively. λ_{100} is the saturation magnetostriction along the <100> direction and λ_{111} is the saturation magnetostriction along the <111> direction. However, in the polycrystalline materials, in which the orientation of the grains is random, the magnetostriction can be calculated by averaging the effects. In a polycrystalline cubic material the saturation magnetostriction is given by,

$$\lambda_s = \frac{2}{5}\lambda_{100} + \frac{3}{5}\lambda_{111} \tag{1.26}$$

Apart from the Joule magnetostriction there are several other effects similar to it. A widely used effect is the *Villari* effect [22]. This effect is based on the principle that when a mechanical stress is imposed on a sample, there is a change in the magnetic flux density which flows through the sample as a result of the creation of a magnetic field. This change in the flux can be detected by using pickup coils and is proportional to the applied stress. This effect is reversible and has been used in sensor applications. Another effect related to magnetostriction is the *Wiedemann* effect. The direct *Wiedemann* effect occurs when a ferromagnetic rod is simultaneously magnetized by a longitudinal field and a circular field generated by a longitudinal current, the resulting helical magnetic field causes the sample to be twisted [23]. The physical background to this effect is similar to that of the Joule effect, but instead of a purely tensile or compressive strain forming as a result of the magnetic field, there is a shear strain, which results in a torsional displacement of the ferromagnetic sample. There is also inverse Wiedemann effect. When a ferromagnet with longitudinal magnetization is subjected to a mechanical torque, the longitudinal magnetization changes and a circular magnetization is observed. This inverse Wiedemann effect is also known as *Matteucci* effect. This effect is now receiving a lot of attention because of its relevance in magnetic torque sensors [24–33].

Magnetostriction plays a very important role in almost all magnetic materials, because the magnetization process of a ferromagnetic material is always associated with some dimensional changes. Sometimes magnetostriction has to be minimized because it opposes the magnetization process thereby increasing the coercivity and the hysteresis loss. For example, in magnetic recording heads and electric transformer cores magnetostriction has to be minimized or completely eliminated. However, this phenomenon can also be used for many applications. Since magnetostriction is an atomic phenomenon, these materials have a lot of advantages. Magnetostrictive materials can be used both as sensors as well as actuators. A magnetostrictive material will elongate or contract under the influence of an external magnetic field thereby acting as an actuator. When a magnetic material is brought under some kind of external stress, its state of magnetization changes. This change in magnetic state leads to a change in the magnetic flux flowing out of these materials, thereby making these materials very good for stress sensing. This bi-directional nature of these materials, have placed them in the family of a special class of materials, namely smart materials [34]. There are several advantages for magnetostrictive smart materials such as non-contact nature of this phenomenon when compared to piezoelectric materials. Continuous research on these materials led to the use of Ni, which has a maximum magnetostriction of 50 ppm, for generating ultrasonic sound in $SONAR$ devices, at the time of second world war.

The largest known magnetostriction in any materials is that observed in rare earth metals at cryogenic temperatures. Single crystals of dysprosium and holmium exhibit magnetostrictive strain of 7500 ppm and 3500 ppm at cryogenic temperatures [35]. The magnetostrictive rare earth metals crystallize in hexagonal close packed structure. In the rare earth elements, the magnetic properties arise from the unfilled 4f shell, where as in the case of transition metals it arises from the 3d electrons. The 4f electron tend to be localized deep inside the atoms and thus they are well shielded from any direct interactions with other 4f electrons on other atomic sites. Apart from this, they also have very larger spin-orbit coupling than the transition metal ions. This results in the large anisotropy as well as larger magnetostrictive strains. However, these giant strains were observed only at cryogenic temperatures. Because of a relatively weak 4f-4f exchange, it is necessary to alloy

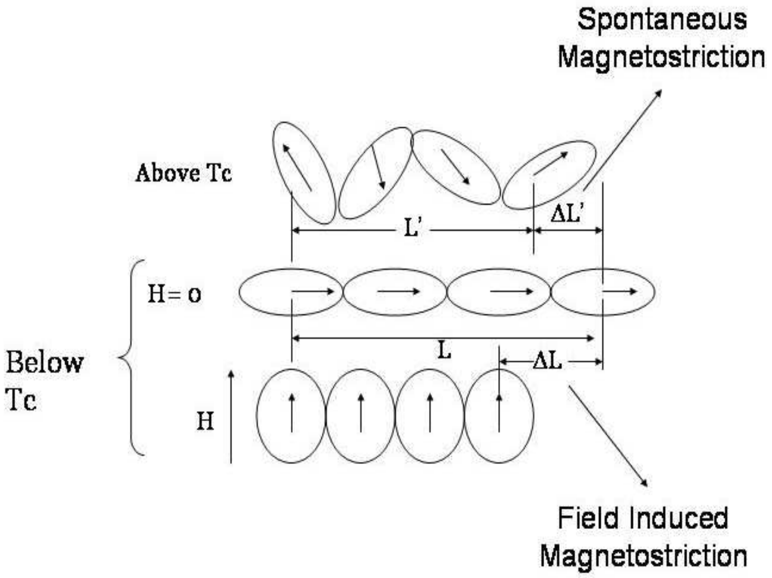

Figure 1.4: Mechanism of Magnetostriction.

these rare earth elements with 3d transition metals in which the exchange interactions are relatively strong. The discovery of giant magnetostrictive alloys at Naval Ordinance Laboratory in the form alloys of RFe_2 Laves phases, gave a new direction to the research in this area. Clark and coworkers discovered giant magnetostrictive strains in alloys $TbFe_2$ and $DyFe_2$ [36].

1.4.1 Physical origin of Magnetostriction

On atomic level, magnetostriction is related to the magnetization process with the origins similar to those of the anisotropy [37]. The origin of magnetostriction lies in spin-orbit coupling. This coupling is also responsible for crystal anisotropy. By coupling one means some kind of an interaction. The exchange interaction between two spins can be called as spin-spin coupling. Similar to spin-spin interaction, the spin-lattice and spin-orbit interactions are also important. The strength of spin-lattice coupling is too weak. There is also a coupling between spin and the orbital motion of each electron. When an externally applied magnetic field tries to align the spin of an electron, the orbit of that electron also tends be oriented. Since the orbit is strongly coupled to the lattice, it therefore resists the change in the orbit orientation. Therefore the energy required to overcome this resistance, can be called as the anisotropy energy which is required to overcome the spin-orbit coupling. This change in the orbit direction ultimately leads to changes in the lattice dimensions since the orbit is strongly coupled to the lattice, giving rise to small dimensional changes.

1.4.2 Magnetostriction in Alloys

Although this phenomenon was discovered as early as in 1842, the range of applications resulting from this were not visualized until the discovery of giant strains of nearly 1% in the rare earth metals like Tb and Dy in 1963. Magnetostriction studies on rare earth metals are very well described in the review by Doerr [38]. The origin of this magnetostriction is the large strain-dependent anisotropy of the rare earth ions (R) which are situated at the cubic sites in the RFe_2 lattice. It remains large because of the large rare-earth-iron exchange interaction which aligns the rare earth spins even at high temperatures. However, only in the case of the RFe_2 compounds the Curie temperatures are as high as 430°C [39], whereas for $TbCo_2$ and $NiTb_2$ Laves phase compounds the Curie temperatures observed are -35 and -227°C respectively [40,41]. Although very high strains are observed in $TbFe_2$, because of the high anisotropy associated with it, higher magnetic fields are required. However, the magnetization anisotropy can be totally compensated by substitution of other rare earth elements with same-sign of magnetostriction and opposite sign of anisotropy constant. It was found that replacing Tb by Dy was the most effective way to reduce the magnetization anisotropy while producing a minimal reduction in strain. Another advantage was that Dy and Tb have nearly the same atomic size and they from complete solid solution [42]. This led to the discovery of the family of the giant magnetostrictive alloys named *Terfenol-D*, $Tb_xDy_{1-x}Fe_2$. For $x = 0.27$, the anisotropy is minimized and the fields required were reduced from a impractical 25 kOe to a practical driving field of 2 kOe for $Tb_{0.27}Dy_{0.73}Fe_2$. At room temperature, strains as high as 1600 ppm are observed in Terfenol-D. Like Terfenol-D, another alloy was developed named *Samfenol-D*, which showed giant negative magnetostriction of 2000 ppm. The magnetostrictive strains can be enhanced by the application of prestress. The application of a pre-stress causes the magnetization to change the preferred direction of magnetization towards the rod axis. A detailed description of Terfenol-D and other alloy based magnetostrictive materials is reviewed in the book by Engdahl. [43]. Apart from the use of bulk materials, thin films of these alloys have also been studied because of their technological as well as fundamental interest [44]. Compared to the difficulty in the preparation of single crystals of the bulk alloys, the thin films have other advantages such as, easy formation of films with single RFe_2 phase, easy designing of films with higher magnetostrictive properties, ready installation in electronic devices, etc. Uchida *et al.* have reviewed the progress in thin films of giant magnetostrictive alloys [45].

1.4.3 Magnetostriction in Oxides

Magnetostriction of oxide magnetic materials have been studied for a long time. The magnitude of magnetostrictive strain in the oxides is not as high as that in the case of rare earth compounds because of the diluted magnetic exchange interactions due to the presence of oxygen in the lattice. There are studies on the magnetostrictive behavior of garnets, spinels and perovskite type oxides in the literature. The rare earth-iron garnets like $Tb_3Fe_5O_{12}$, $Dy_3Fe_5O_{12}$, and $Ho_3Fe_5O_{12}$ were found to exhibit very high magnetostriction up to 2400, 875, and 475 ppm respectively in the single crystalline form at a temperature close to -269 °C [46]. At room temperature, however, the magnetostrictive strains are almost negligible. Licci *et al.* have performed systematic investigation of hexagonal ferrites and found that the magnetostrictive strain measured in the same direction as that of the field is always positive except for the samples containing Fe^{2+} ions and larger strains were observed for the samples containing Ni and Co [47]. A strong spin orbit coupling causes the rare earth spins to rotate from a preferred direction as the temperature is lowered. As the orbital moment follows the rotation of spins, the 4f electron clouds also rotate. This induces a perturbation in the local electrostatic field which is partially compensated by the shifting of the surrounding oxygens leading to an overall distortion of the lattice.

Similar to the rare earth garnets, very high magnetostrictive strains are observed in perovskite oxides at low temperatures. Doped perovskite manganites ($AMnO_3$ where a is a trivalent rare earth ion) show a wide variety of magnetic field induced phenomena. The magnetic and transport properties of manganites are governed by the mixed valence of the Mn ions and is less affected by the oxygen ions, The d-electrons are involved in a variety of interactions such as double-exchange, superexchange, Jahn-Teller distortion, etc. In all these interactions the e_g electrons of the Mn^{3+} ions play a very important role. The orbital degeneracy leads to a variety of phenomena, such as magnetic, structural, and metal insulator transitions, collapse of charge order state under the influence of a magnetic field etc, and is responsible of strong magnetoelastic coupling. The first observation of very large magnetostrictive effects in perovskite manganites were made very soon after the discovery of colossal magnetoresistance in this group of materials [48, 49]. Kuwahara *et al.* observed a magnetic field induced phase transition from charge ordered antiferromagnetic state to a ferromagnetic state [50]. Dabrowski have studied the magnetostriction of $La_{1-x}Sr_xMnO_3$ and correlated the observed striction effects to the spin lattice coupling [51]. Rivadulla *et al.* have studied the magnetoelastic behavior of charge ordered manganites like $Nd_{0.5}Sr_{0.5}MnO_3$, and $La_{0.5}Ca_{0.5}MnO_3$ [52]. Similarly, Gwag *et al.* have proved the presence of strong electron-phonon and spin coupling in $(La_{1-x}Gd_x)_{0.7}Ca_{0.3}MnO_3$ [53]. Mahendiran *et al.* have observed giant anisotropic magnetostriction, as high as 1500 ppm, in $Pr_{0.5}Sr_{0.5}MnO_3$ [54], and were able to observe a magnetic field induced antiferromagnetic to ferromagnetic transition which was accompanied by a structural transition. Teresa *et al.* have studied the magnetostriction as a function of temperature for $La_{2/3}Ca_{1/3}MnO_3$ and were able to use this data as a support for the formation of magnetic polarons in this system [55]. The study of magnetostriction as a function of temperature has been utilized to understand the nature of spin-lattice coupling in manganites. Similar to manganites, perovskite type cobaltites also exhibit large magnetostrictive strains [56,57]. Apart from these studies there are many other reports on the magnetostriction studies on perovskite manganites and cobaltites [58–72]. However, these large strains in the manganites are observed only at very low temperatures and require very high magnetic fields. The requirement of very high magnetic field restricts the use of this kind of materials for practical applications for sensing and actuation. Szymczak has reviewed giant magnetostriction effects in oxides, especially in CMR materials, quasi-one-dimensional antiferromagnets and high temperature superconductors [73].

Amongst ferrimagnetic spinels, cobalt ferrite shows higher magnetostrictive strains in both single crystal as well as polycrystalline forms [74]. The first studies on the magnetostriction behavior of spinel ferrites were performed by Bozorth [75, 76] and Guillad [77]. Bickford *et al.* performed magnetostriction measurements on synthetic and natural magnetite crystals from 120K to 300K [78]. The recent studies on cobalt ferrite based materials have shown that these oxide based materials can be a suitable alternative to the costly alloy based materials. These have several advantages over alloy based materials although strains observed are less. The ease of synthesis, use of polycrystalline materials, easy molding in a desired shape, high corrosion resistance, low production cost, minimum eddy currents due to high resistivity and high Curie temperatures are some of the advantages. Recently cobalt ferrite based materials were also found to be suitable for non contact stress sensing applications [79–81].

1.4.4 Applications of Magnetostrictive Materials

Magnetostrictive materials belong to the class of smart materials. Piezoelectric materials, magneto-rheological fluid, and shape memory alloys are some other examples of smart materials. This class of materials can perform dual functions of sensing an external stimuli and responding via an actuation process. Magnetostriction can be used to convert magnetic energy in displacement, a typical example of actuation, while typical magnetic sensor effect rely on the inverse magnetostrictive effect, where the magnetic properties of the material are affected by the application of a mechanical load/stress [82]. A variety of applications have been designed based on magnetostriction. Most of the current applications are based on the use of Terfenol-D. However, Ni was used for the generation

Table 1.1: Magnetostriction, anisotropy and Curie temperature of some magnetostrictive materials [43].

Material	$\lambda_{100}(10^{-6})$	$\lambda_{111}(10^{-6})$	$\lambda_s(10^{-6})$	$K_1(10^3 J/m^3)$	$T_C(K)$
Iron	21	-21		47	1043
Nickel	-46	-24	-33	-59	631
$CoFe_2O_4$	-920	180	-260	60^*	793
$TbFe_2$			1753	>1000	700
$DyFe_2$			1560		676
Terfeno-D	90	1640	-1000	60	650-670

* This valve is sensitive to the exact stoichiometry, Co/Fe ratio and heat treatment.

of ultrasound waves in SONAR devices during world war times. Materials conventionally used for actuation are magnetostrictive elements like nickel, cobalt, iron, and their alloys. These materials possess magnetostrictive strains typically lower than 100 ppm. In recent years, after the discovery of giant magnetostrictive materials based on Terfenol-D and other rare earth based materials with giant magnetostriction, up to 2400 ppm, many new applications were proposed. Reduction mass actuator and linear motor based on terfenol have been developed [83]. Terfenol-D has also been used to build a sonar transducer. A structure has been developed to convert the elongation movement of a magnetostrictive material into a rotary motion to form a micro stepping rotary motor [84]. Magnetostriction can be used in linear motion actuators in combination with conventional technologies like hydraulic technologies. Small elongations, added step by step, can be used as a working principle in a simple pump for high-pressure fluid flow. A system combining the magnetostrictive functionality with hydraulic non-return valves has been developed [85]. The high efficiency in converting magnetic energy into mechanical energy and vice versa, enables the use of this property to be used in contact-less sensor applications. Various other application are described in the book by Engdahl [43].

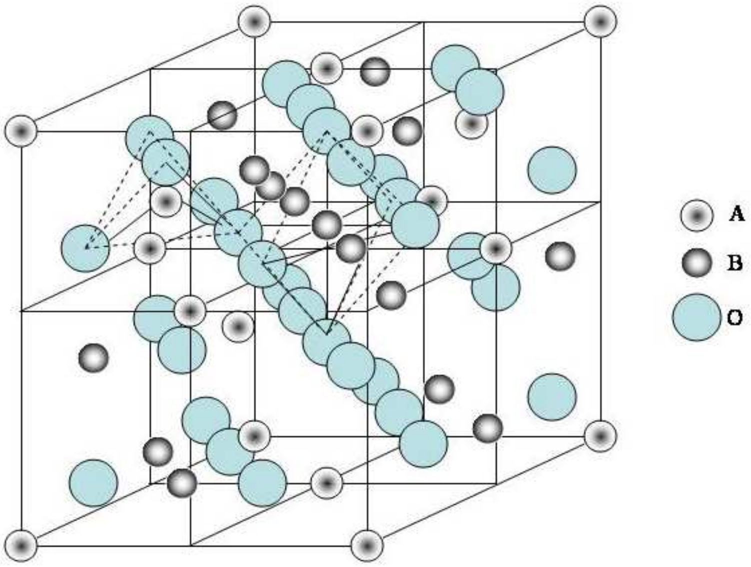

Figure 1.5: The Spinel structure.

1.5 Materials Studied In the Present Work

This thesis deals with the studies on two different types of magnetic oxides. The part one (Chapters 3 and 4) of the work presented here deals with the magnetic and magnetostriction studies on cobalt ferrite. The second part (Chapter 5) of the work deals with understanding the properties of substituted lanthanum manganite. The structural and magnetic aspects of these two classes of materials are discussed in the following sections.

1.5.1 Spinel Ferrites

Ferrites can be divided into three different classes namely spinel type ferrites, hexaferrites, and the rare earth ferrites (the garnet materials). Ferrites are ferrimagnetic materials having the reputation of industrially valuable class of oxides. Ferrites are used in permanent magnets, inductors, power transformers, channel filters, magnetic recording heads, loading coils, loud speakers, electric motors, stepping motors, pulse transformers, flyback

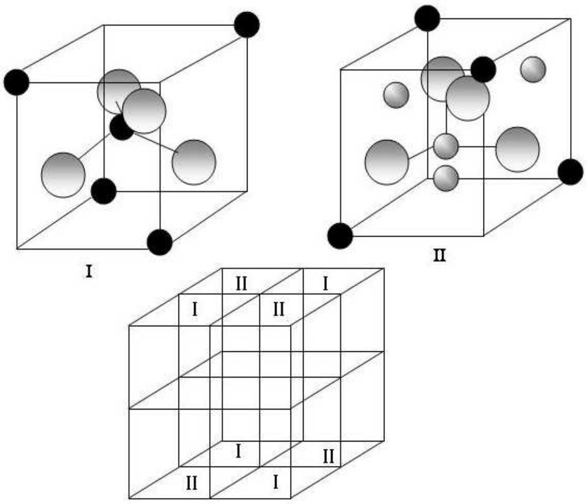

Figure 1.6: The two types of octants containing A cations in the tetrahedral (type I) and the B cations in the octahedral (type II) coordination in the unit cell divided into eight small octants.

converters, push-pull converters, waveguide in microwave region, etc. [1,86–88].

Spinel structure is derived from the mineral spinel $MgAl_2O_4$ and the spinel type oxides have the general formula AB_2O_4. Spinel ferrites have the general formula MFe_2O_4. The spinel structure is shown in figure 1.5. The spinel lattice is composed of close packed oxygen atoms in which 32 oxygen atoms form a unit cell which is the smallest repeating unit in the crystal network [89]. The oxygen ions form interstices which can be accommodated by different metal ions, There are two types of interstices formed, as shown in figure 1.6, one is called the tetrahedral or the A-site which is surrounded by four oxygen ions, and the second one is the octahedral site or the B-site. In the unit cell of 32 oxygen ions there are 64 tetrahedral and 32 octahedral sites. If all these sites are filled up by metal ions with either +2 or +3 valence, then the positive charge will be much greater than the negative charge and the structure will not be electrically neutral. So it turns out that out of the 64 tetrahedral sites only 8 are occupied and out of the 32 octahedral sites only 16 are occupied thereby maintaining the charge neutral. One unit cell contains

8 formula units MO.Fe_2O_3. The spinel ferrite space group is $O_h{}^7$ (Fd3m) [90, 91] (space group number 227). The oxygen ions in the *fcc* lattice do tend to adjust their positions in order to accommodate the difference in the radius ratio of the cations in the tetrahedral and octahedral sites. This adjustment parameter is known as *oxygen parameter* denoted as *'u'* [74, 92]. In an ideal spinel structure the angle B-O-B is about 90° and the angle A-O-B is 125°. The A-O distance is $a(x\text{-}1/4)\sqrt{3}$ and the B-O distance is $a(5/8\text{-}x)$.

The distribution of the cations in the tetrahedral and the octahedral sites is governed by many parameters such as the ionic radius, the size of the interstices, temperature, the orbital preference for specific coordination, electronic configuration, electrostatic energy (Madelung enery) and most importantly the crystal field stabilization energy. Depending upon the distribution of cations in the A and B-sites, spinel ferrites are classified further into two categories namely normal spinels and inverse spinels. In general, the cation distribution can be represented as $M_{1-x}{}^{2+}Fe_x{}^{3+}[M_x{}^{2+}Fe_{2-x}{}^{3+}]$ where the ions inside the square bracket are situated in the octahedral sites and those outside are situated on the tetrahedral sites. When $x = 0$, then all divalent ions occupy the tetrahedral or the A-sites and the spinel is called as normal spinel. The examples of normal spinel are $ZnFe_2O_4$ and $CdFe_2O_4$, in which the Zn^{2+} and Cd^{2+} ions are situated on the A-sites and all the Fe^{3+} are situated in the B-sites. When $x = 1$, the spinel is called as inverse spinel, *e.g.* $CoFe_2O_4$ and $NiFe_2O_4$. In this case the divalent Co and Ni are present in the octahedral sites. However, the value of x can lie in between 0 and 1 also. In this case the spinel is called as mixed spinel, such as $CuFe_2O_4$ and $MgFe_2O_4$. The cation distribution is sensitive to the method of synthesis and heat treatments. The magnetic, structural, and optical properties of spinel ferrites are very much dependent on the cation distribution and the microstructure of the final sintered products. Groenou *et al.* have reviewed the effect of microstructure control with emphasis on the sintering process of spinel ferrites [93].

Magnetism in Ferrites

Magnetization in ferrites occurs from the uncompensated antiferromagnetism, so the magnitude of magnetization depends on composition, cation distribution and the relative strength of the possible interactions. Since cation–cation distances are large in ferrites due to their crystal structure, direct exchange interactions are negligible. The major interaction occurs in ferrites is the superexchange interaction between octahedral and tetrahedral cations or A–O–B interactions [74, 86, 88]. The next acceptable interaction is B–O–B superexchange. However, A-O-A interaction is not coming into picture, as it is very weak [92]. The strength of exchange interactions control the saturation magnetization and the Curie temperature of the ferrites and this exchange interaction is controlled by cation distribution. The magnetic exchange forces between the metal ions in the ferrites are mediated via oxygen ions by an exchange mechanism best known as the *superexchange* interaction. If there are n identical magnetic ions per unit volume, then a fraction x is located on A-sites and a fraction y = (1-x) on the B-sites. μ_A and μ_B represent the average moment of A and B ions in the direction of field at temperature T. The ions A and B are exposed to different molecular fields, so μ_A and μ_A are not identical, even though the ions A and B are identical. Then the magnetization of the A-sublattice is $\mathrm{M}_A = x\mathrm{n}\mu_A$. The total magnetization of the two sublattices is

$$M = M_A + M_B \tag{1.27}$$

The molecular field acting on the sublattice A is

$$H_{mA} = -\gamma_{AB} M_B + \gamma_{AA} M_A \tag{1.28}$$

and molecular field acting on the sublattice B is

$$H_{mB} = -\gamma_{AB} M_A + \gamma_{BB} M_B \tag{1.29}$$

Here M_A and M_B represent the magnetizations of the A and B sublattice, respectively. The strength of the exchange interactions between A-A, B-B and A-B are represented by γ_{AA}, γ_{BB} and γ_{AB} respectively. Here the molecular field coefficients represented by γ are to be regarded as positive quantities and the negative sign corresponds to the antiparallel interaction between A and B ions, whereas the positive sign corresponds to the parallel interaction between the same site ions. The magnetization of each sublattice obeys the

Curie law,

$$M_A = \frac{C_A}{T}(H + H_{mA}) \tag{1.30}$$

$$M_B = \frac{C_B}{T}(H + H_{mB}) \tag{1.31}$$

Since the Curie constants C_A and C_B are not identical for the two different sites, the above equations are modified by introducing the term density of ferrimagnetic materials on the right hand sides and now putting the values of H_{mA} and H_{mB} in equations 1.30 and 1.31, the magnetization on the two different sites are obtained as

$$M_A = \frac{\rho C_A}{T}(H + \gamma_{AA} M_A - \gamma_{AB} M_B) \tag{1.32}$$

and

$$M_B = \frac{\rho C_B}{T}(H + \gamma_{BB} M_B - \gamma_{AB} M_A) \tag{1.33}$$

After solving these two equations, the mass susceptibility, χ, of a ferrimagnetic material is obtained as

$$\chi = \frac{M}{\rho H} = \frac{T}{C} + \frac{1}{\chi_0} - \frac{K}{T - \Theta} \tag{1.34}$$

where C = C$_A$ + C$_B$ and K is a constant. Although Θ has the dimension of temperature, it has no physical significance above the Curie temperature. Therefore,

$$\chi = \frac{C}{T - \Theta} \tag{1.35}$$

Thus, from equation 1.35, it is concluded that above the Curie temperature ferrimagnetic materials obey the Curie-Weiss law [7, 86, 94].

Cobalt ferrite, $CoFe_2O_4$, is known to have very important magnetic properties such as high saturation magnetization and coercivity. It is one of the technologically important ferrite. Earlier it was reported that cobalt ferrite is an inverse spinel [95], however detailed investigations have shown that it is not completely inverse [96]. There has been special attention to cobalt ferrite because of its high coercivity and saturation magnetization. Many novel synthesis routes have been developed for the synthesis of nanosized cobalt ferrite such as combustion method [97], micro-emulsion method [98], sol-gel synthesis, etc [99]. Also, cobalt ferrite exhibits highest magnetostriction amongst the ferrimagnetic spinels [74]. The magnetostrictive properties of cobalt ferrite have been investigated in the 1950s, both on polycrystalline material [77] as well as on single crystals [75]. Amongst ferrimagnetic spinels, cobalt ferrite has the highest value of magnetostriction in both its single crystal as well as polycrystalline forms. In single crystal form, maximum magnetostriction of 600-900 ppm has been reported depending on the composition [76, 80, 87]. For polycrystalline cobalt ferrite a maximum value close 230 ppm has been reported recently by McCallum *et al.* [80]. Efforts have been made to enhance the magnetostrictive strains further by magnetic annealing [100]. Cobalt ferrite based materials have been proposed as promising materials for stress sensing applications [79].

1.5.2 Perovskite Manganites

Ideal perovskites type oxides have the general formula ABO_3 where A-site cations are typically larger than the B-site cations and similar in size to the anions [101]. Perovskite-type oxides derive their name from the mineral called *perovskite* with the chemical formula $CaTiO_3$. It was first described in the 1830's by the geologist Gustav Rose, who named it after the famous Russian mineralogist Count Lev Aleksevich Von Perovski. The Phenomenon of ferroelectricity was first observed for a perovskite oxide, $BaTiO_3$, in the year 1945 [102]. After this discovery, extensive research work on these materials led to the discovery of many new ferromagnetic, ferroelectric and piezoelectric materials. The discovery of superconductivity in the perovskite type oxide, $Ba_xLa_{5-x}Cu_5O_{5(3-y)}$ ($x = 1$ and 0.75 and $y > 0$) [103], and *Colossal Magnetoresistance* (CMR) in the compound $La_{0.67}Ca_{0.3}MnO_x$ (x depends on the oxygen pressure during the synthesis) [104], have caught the attention of many researchers towards this family of materials. It is also interesting to note that the magnetic and electrical properties of these materials can be modified by suitable substitution of proper ions in the perovskite structure.

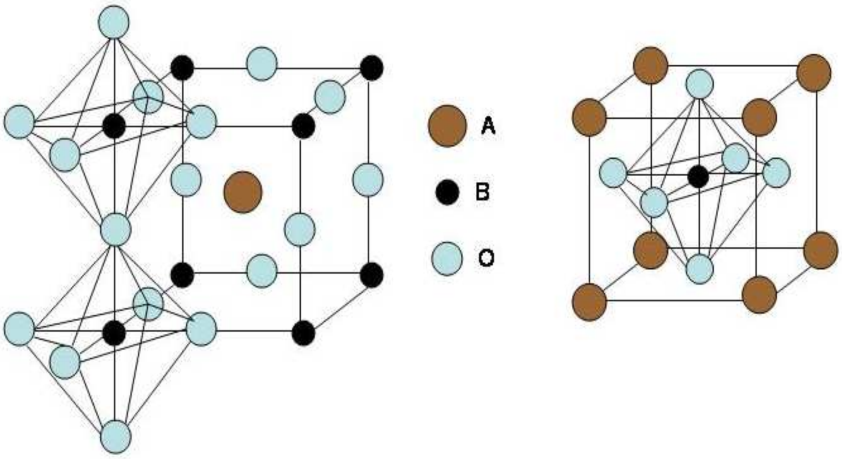

Figure 1.7: Structural features of an ideal perovskite, ABO_3.

Structural Aspects

Figure 1.7 shows that in the perovskite structure the A cations are surrounded by twelve anions in cubo-octahedral coordination and the B ions are surrounded by six anions in octahedral coordination. The oxygen anions are coordinated by two B-site cations and four A-site cations. Perovskites having the ideal structure adopt the cubic space group Pm3m (space group number 221). $SrTiO_3$ is commonly regarded as the archetypical cubic perovskite as its structure approaches closely that of the ideal ABO_3 compound. In the case of perovskite oxides, Goldschmidt defined the tolerance factor [105] as,

$$t = \frac{r_A + r_O}{\sqrt{2}(r_A + r_O)} \tag{1.36}$$

which is unity for ideal sized cations. The perovskite structure occurs only within the range $0.75 < t < 1.00$.

However, the perovskite structure is rarely cubic, due to unavoidable misfit in the packing of atoms, if the atoms A and B are not of the ideal relative sizes. The A and B cations must in themselves be stable in twelve fold and six fold coordinations. This implies that the ionic radii for a A-site ions r$_A > 0.90$ Å, and r$_B > 0.51$ Å. If $0.75 < t < 0.9$, then a cooperative buckling of the corner shared octahedra with an enlarged unit cell is observed [106]. On the other hand, if $0.9 < t < 1$, then buckling of the octahedra is not observed, instead smaller distortions to rhombohedral symmetry occur. This size mismatch can not be compensated by the relative shifts in the atomic positions so as to keep the symmetry intact (as in case of spinels). Instead, a structure with lower symmetry is formed such as rhombohedral, orthorhombic, monoclinic and tetragonal. These structures are temperature dependent and they can reversibly or irreversibly convert to different structures at different temperatures as in the case of $BaTiO_3$ [102]. The structural distortions in manganites arise mainly because of two factors. The A-size cation mismatch and the Jahn-Teller effect of the B-site ions (such as Mn^{3+}). The structural changes can also be induced by collective electrons as is commonly seen in the case of ferroelectric materials like $BaTiO_3$. Such materials undergo structural transitions from orthorhombic to rhombohedral, because of the displacement of the Ti ions along the [111] direction of the crystal.

The Jahn-Teller (JT) effect plays an important role in determining the structural features of the perovskite type manganites $AMnO_3$. This effect distorts the MnO_6 octahedra in order to produce long and short Mn-O bonds. The distortion of this kind results from the well known Jahn-Teller theorem which states that, for a non liner molecule, in an electronically degenerate state, distortion must occur to lower the symmetry, to remove the degeneracy and lower the energy.

In $LaMnO_3$, the Mn^{3+} ions show the Jahn-Teller effect, in which the MnO_6 octahedra distorts in such a way as to produce long and short bonds. This occurs below a characteristics temperature (T_{JT}). The most effective distortion is the basal plane distortion (called Q_2 mode) in which the one diagonally opposite O-pair is displaced outward and the other is displaced inwards as shown in figure 1.8. It has been shown that a JT distortion involving a displacement of the oxygen ions > 0.1 Å leads to the splitting of the e_g band of the manganite and opens a gap at the fermi level. The parent compound, $LaMnO_3$ is a Jahn-Teller distorted compound. Below 900 K, the rhombohedral structure of $LaMnO_3$

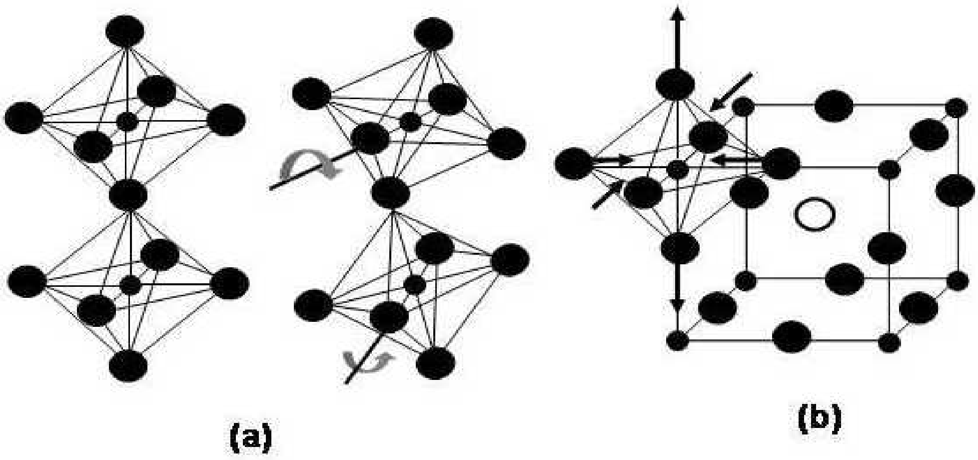

Figure 1.8: Structural distortions in perovskites. (a) due to cation size mismatch and (b) due to Jahn-Teller effect

changes to O'-orthorhombic, associated with the freezing of dynamic distortion. This can be regarded as an order-disorder transition, where the static Jahn-Teller effect becomes dynamic [107, 108]. Here, the O'-orthorhombic structure with $c/a<\sqrt{2}$ indicates that the Jahn-Teller distortions are superimposed on an O-orthorhombic crystal with $c/a>\sqrt{2}$, which is already distorted due to ionic-size mismatches [109]. Nevertheless, the impact of these localized electronic effects on the structure is of ten times less, when compared to that from the ionic size/charge effects. The Mn-O-Mn bond angles are about 155° in $LaMnO_3$ [110].

Magnetic Properties

In the parent compound $LaMnO_3$, the cooperative buckling of the MnO_6 octahedra due to the ionic size mismatch gives rise to orthorhombic structure [111]. The so called "internal pressure" created because of the cation size mismatch can be reduced by the incorporation of Mn^{4+} ions, which has a relatively smaller ionic size. This has been supported by the observation of an abrupt decrease in the Mn^{4+} content, when smaller ions like Al^{3+} and

Co^{3+} are substituted for Mn [112, 113]. The additional charge due to Mn^{4+} is supposedly compensated by the presence of excess oxygen. In reality, there is no such provision to accommodate excess oxygen, in the perovskite structure. Therefore this actually refers to cation deficiency, and is represented as $La_{1-x}Mn_{1-y}O_3$. This cation deficient compounds are expressed as $LaMnO_{3\pm\delta}$, where δ represents the "excess" and the negative sign gives the deficiency of oxygen.

The JT distortion leads to the formation of two new e_g orbitals in $LaMnO_3$, namely, $3x^2$-r^2 and $3y^2$-r^2, formed by linear combination of $3x^2$-y^2 and $3z^2$-r^2 with the help of Q_2 mode of Jahn-Teller active mode of vibration [114]. Now, hybridization with the oxygen 2p orbitals gives anti-bonding nature to these new orbitals. Thus, e_g orbital extending along the longer Mn-O bond has lower energy and results in the ordering of $3x^2$-r^2 and $3y^2$-r^2 orbitals in the *ab*-planes [115]. In short, Mn^{3+}-O-Mn^{3+} exchange interactions become anisotropic and results in A-type antiferromagnetic spin ordering below 135 K, but with a positive Θ. In the A-type ordering, ferromagnetically ordered adjacent Mn-planes are coupled antiferromagnetically resulting in no net magnetic moment.

The structural, magnetic and transport properties of A-site substituted $LaMnO_3$ in the series $La_{1-x}A_xMnO_3$, have been vastly studied in the recent past. Divalent ions having suitable ionic radii, like Ca^{2+}, Sr^{2+}, Pb^{2+}, can be substituted for La. This introduces equivalent amount of Mn^{4+} ions in the structure, in order to maintain the charge neutrality and to reduce the JT distortion. The material becomes ferromagnetic at a finite x and metallic below T_C [116, 117]. Apart from the interesting magnetic and structural properties, these hole doped manganites also exhibit the CMR effect [118–120].

In the manganites, important type of exchange is the superexchange, where the oxygen p orbitals mediate the exchange through the Mn-O-Mn linkage whose ideal bond angle is 180° [121]. Depending upon the nature, symmetry, and occupancy of the e_g orbitals, the coupling results in various types of magnetic ordering; the governing factors being the Pauli antisymmetric principle and Hund's rule of spin multiplicity. If the e_g orbitals on both the Mn ions are half filled, an antiferromagnetic type of exchange results and if e_g orbital of one Mn ion is vacant, with the other half filled, a ferromagnetic

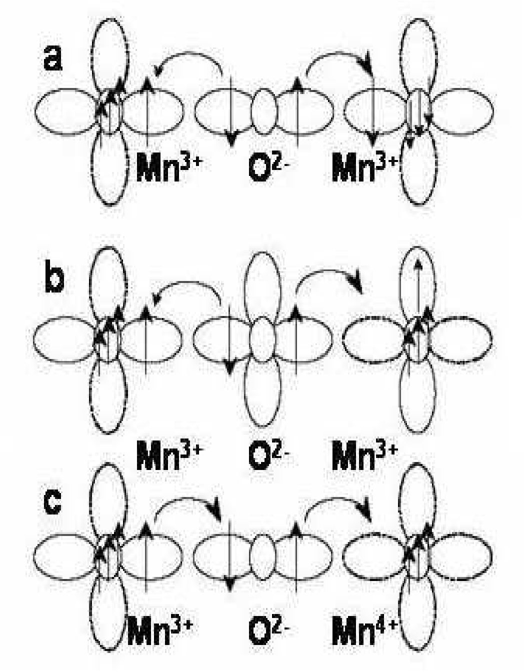

Figure 1.9: Different types of exchange in manganites.(a) and (b) superexchange (c) double exchange.

type of exchange results. Figure 1.9(a) and (b) show the superexchange mechanism in manganites. However, certain correlated phenomena like co-existence of metal-insulator transition and ferromagnetic-paramagnetic transition could not be explained by the simple superexchange scenario. Hence, the concept of double exchange was suggested for explaining this behavior in certain hole-doped manganites. The origin of ferromagnetism in manganites has been explained by Zener in the so called *double exchange* mechanism (DE) [122], which was further developed by various researchers [123, 124]. The double exchange mechanism involves the real transfer of an electron from the partially filled e_g orbital of Mn^{3+} to the empty e_g orbital of Mn^{4+}, via the intermediate oxygen ion. DE results in the initial and final states of the same energy. During DE, the spin of the hopping electron is kept intact *via* Hund's rule coupling. All these salient features of the DE were believed to be the reason for metallic conductivity and CMR effect of $La_{1-x}A_xMnO_{3\pm\delta}$ compounds below the ferromagnetic transition temperature. The schematic of the double exchange mechanism is shown in figure 1.9(c).

B-site Substituted $LaMnO_3$

The substitution in the A-site of $LaMnO_3$ cause changes in the spin states of the Mn ions situated in the B-site. Therefore, the magnetic properties can be controlled by direct substitution at the B-site by different metal ions like in $LaMn_{1-y}D_yO_3$ where M is a smaller metal ion. Depending upon the nature of magnetic interactions between the Mn^{3+} and the other substituted ions, the magnetic properties will change. The substitution at B-site can be broadly classified into two classes, based upon the nature of the substituent ion namely d^0 or d^{10} substituents in which the d orbitals are either empty or full and substituents having empty d orbitals.

Substitution of Ions With Empty or Filled d Orbitals

The effect of substitution of various non-magnetic ions such as Li^+, Na^+, Mg^{2+}, Sc^{3+}, Sn^{4+}, Zn^{2+}, Ga^{3+}, Al^{3+}, and Ti^{4+} has been reported in the literature. In principle, these ions do not directly take part in magnetic exchange. However, they affect the magnetism and crystal structure of the parent phase via the size effect as well as because of the dilution of the magnetic interactions. Depending upon the size of the substituent ions, the Mn-O-Mn bond angle may change, which in turn affects the strength of the superexchange interaction. The difference in the ionic size or ionic charge as compared to that of Mn^{3+} may lead to ordering of these ions in the B-site of the perovskite lattice. However, if the ionic sizes and charges are same, then they may not show a site preference, instead a random distribution may take place. The effect of substituting monovalent ions like Li^+ [125–127] and Na^+ ions [128, 129] has been studied. The Li^+ ions introduces equivalent amount of Mn^{4+}, however, the magnetic and transport properties are different than those observed for $La_{1-x}A_xMnO_3$ containing equivalent amount of Mn^{4+}, showing insulating, spin-glass behavior. Substitution of Na^+ showed a weak and broad ferromagnetic transition, incipient at around 300 K. The Mg^{2+} substitution showed an orthorhombic structure and an increase in T_C, up to 20% Mg content was observed by Kutty and Philip [126]. The substitution of Zn^{2+} ions has been reported by Hebert *et al.* [127] and Hu *et al.* [130]. These two reports contradict each other in terms of magnetic behavior. According to Hebert *et al.* the T_C increases initially up to $x = 0.15$ and then decreases for $x = 0.2$. This initial increase was attributed to the destruction of the orbital ordering in $LaMnO_3$ by Zn substitution [127]. Hu *et al.* reported a continuous decrease in the T_C with increasing Zn content and explained on the basis of ferromagnetic cluster formation [130]. Substitution of the trivalent ion Sc^{3+} induces ferromagnetism because of the destruction of the orbital ordering in $LaMnO_3$ [131]. The effect of substituting Ga^{3+} up to $x = 0.5$ in $LaMn_{1-x}Ga_xO_3$ has been studied by several authors [109, 114, 127, 132–134]. It was found that Ga^{3+} ions order in the (001) plane exhibiting an O'-orthorhombic structure and a spin-glass or a canted spin-glass to ferromagnetic transition is observed for $x = 0.2$ [109, 127, 132–134]. The effect of substitution of Al^{3+} ions was first studied by Jonker [135] and reported a monoclinic structure for the compositions. Recently, however, O-orthorhombic structure has been reported by Goodenough *et al.* [131]. The substitution of tetravalent ions like Sn^{4+} and Ti^{4+} has also been reported. In the case of Sn^{4+} substitution, a decrease in the magnetization and a rhombohedral structure have been observed [136] along with the presence of SnO_2 impurity for $x \geq 0.15$ [137]. The Ti substituted compositions were found to have orthorhombic structure [126], and a decreasing magnetic moment and T_C were observed with increasing Ti content.

Substitution of Ions with Partly Filled *d* Orbitals

The effect of vanadium substitution for Mn, $LaMn_{1-x}V_xO_3$, in the composition range (0.1 $\leq x \leq$ 0.9) has been reported by Teplykh *et al.* [138]. All the compositions in the series were found to have an orthorhombic structure. These compositions exhibit spin-glass behavior coexisting with short range magnetic ordering. The smaller size of the V^{3+} ion as compared to that of Mn^{3+} may help to reduce the internal pressure. The destruction of the orbital ordering resulting from a random occupancy of the V ions can produce isotropic Mn^{3+}-O-Mn^{3+} exchange, in addition to the positive Mn^{3+}-O-V^{3+} superexchange leading to short range ferromagnetism.

The effect of substituting Co, Ni and Cr has been studied in detail by several authors. The structural studies on Cr substituted samples reported a monoclinic structure for the Mn rich samples [116, 139]. However, recent studies have shown rhombohedral [140–142] and O'-orthorhombic [143] structure in this compositional range. For higher Cr concentrations, an orthorhombic structure has been reported recently [139, 140, 144, 145]. The composition with lower Cr content were found to be ferromagnetic and the T_C decreases with increasing Cr content [143, 144]. At higher Cr concentrations different magnetic behaviors such as ferromagnetic cluster formation [143] and ferrimagnetic behavior [139] have been reported. The substitution of Co also shows a blend of crystal structures depending upon the Co content. Co rich compositions have been reported to exhibit rhombohedral structure [146, 147] and Mn rich compositions show orthorhombic structure [147, 148]. The magnetic studies performed on Co substituted samples showed the ferromagnetic nature of the compositions. Depending upon the spin states, there are three positive superexchanges reported for the ferromagnetic behavior of $LaMn_{1-x}Co_xO_3$, viz. Mn^{3+}-O-Mn^{3+}, Mn^{4+}-O-Mn^{3+} and Mn^{4+}-O-Co^{2+} exchanges. The substitution of Ni in the series $LaMn_{1-x}Ni_xO_3$ shows orthorhombic structure for Mn rich compositions [127, 149, 150]. In these compositions, the ferromagnetic ordering temperature increases with x and a maximum T_C is obtained for $x = 0.5$. However, both the Co and Ni substituted samples are reported to show mixed phase behavior [109,151,152]. The existence of two different ferromagnetic phases has been reported in the case of $LaMn_{0.5}Co_{0.5}O_3$ and $LaMn_{0.5}Ni_{0.5}O_3$ with different ordering temperatures depending upon the spin states of the ions [153,154].

The substitution of Fe for Mn has been reported to have orthorhombic [148,155–157] as well monoclinic structures. However, Tong *et al.* have reported rhombohedral structure for $0.0 \leq x \leq 0.3$ in $LaMn_{1-x}Fe_xO_3$, which then transforms to orthorhombic structure for higher Fe content [158]. The magnetic properties of Fe substituted compositions show very interesting features. In the low concentration range, the parallel alignment of the magnetic moments is not observed [159, 160] and the magnetic transition temperature decreases along with the broadening of the magnetic transition to a wide temperature range with increasing x. The substitution of Mn by Fe in the $La_{1-x}A_xMnO_3$ system, which is already ferromagnetic and metallic, destroys ferromagnetism and conductivity with increasing Fe^{3+} ion concentration [156,161–165]. Reports on $LaMn_{1-x}Fe_xO_3$ show that Fe is present in the trivalent high spin state. Fe^{3+} has the same ionic size as that of Mn^{3+}, due to which it may be randomly distributed in the B-site of the perovskite lattice. Such a random occupancy increases the probability for Fe^{3+}-O-Fe^{3+} antiferromagnetic exchange interactions. Mn^{3+}-O-Fe^{3+} (HS) exchange is predicated to be strongly ferromagnetic [19]. The influence of Fe^{3+}-O-Fe^{3+} on the above ferromagnetic exchange and the random occupancy of Fe^{3+} in the Mn-site of the manganite are evident from the studies on a thin film sample of $LaMn_{0.5}Fe_{0.5}O_3$, where Mn and Fe ions are found to be ordered to a considerable extent [166–168]. Joly *et al.* have studied the effect of Fe substitution for Co on the high T_C phase of $LaMn_{0.5}Co_{0.5}O_3$ and explained the observed magnetic behavior based on the random distribution of Mn and Fe ions in the B-site of the perovskite lattice [169].

Thus, the magnetic properties of lanthanum manganites are very sensitive to the spin states of the metal ions present in the A-site as well as in the B-site of the perovskite lattice. Also, the processing temperatures can lead to evolution of different magnetic phases having different spin states of the metal ions present.

1.6 Scope of the Present Work

1.6.1 Magnetostrictive Investigations on Cobalt Ferrite

The importance of magnetic materials in present day's technologies is tremendous. The development of suitable magnetic materials with enhanced magnetic properties can help in constructing new devices with superior performance. The applications of magnetostrictive materials can be recognized by the tremendous potential of Terfenol-D. However, the need to overcome certain disadvantages of this alloy based magnetostrictive material, has motivated the investigation towards finding a suitable alternative material. Recent developments in this field have shown that cobalt ferrite is a promising material for developing oxide based magnetostrictive materials. However, there are only very few reports on the systematic investigation of the magnetostriction of cobalt ferrite. In the present work a detailed analysis has been carried out in order to understand the relationship between the magnetostriction of cobalt ferrite and other factors.

1.6.2 Magnetic Properties of $LaMn_{1-x}Fe_xO_3$

The perovskite manganites show magic interplay between the spin, charge and electronic degrees of freedom. The magnetic properties of manganites have shown interesting properties like colossal magnetoresistance (CMR) and magnetocaloric effect. Perovskite manganites have also been reported to show giant magnetostriction close to the Curie temperature. The magnetic properties of the manganites are very sensitive to substitution of different cations in the A-site as well as B-site of the perovskite structure. The antiferromagnetic insulator $LaMnO_3$, can be turned into a ferromagnetic by substitution of Co^{3+}, Ni^{3+} and Cr^{3+} in the B-site. However, the substitution of Fe^{3+}, even though Fe^{3+} is magnetic in nature, in the B-site destroys the ferromagnetic ordering. The work performed in the present study analyzes the effect of Fe substitution for Mn in $LaMnO_3$. The magnetic properties of Fe substituted $LaMnO_3$ have been studied after processing a low-temperature synthesized sample at different high temperatures. The results presented here show that the magnetic properties are sensitive to processing temperatures, and the distribution of Mn^{3+} and Fe^{3+} ions in the perovskite lattice depends on the processing temperature. The present study also highlights the different role played by Fe ions as compared to other metal ions like Co, Ni and Cr.

References

[1] E. du Trmolet de Lacheisserie, D. Gignoux and M. Schlenker (Eds.), *Magnetism: Materials and Applications* (Springer, 2003).

[2] J. K. Furdyna, *J. Appl. Phys.* 64 (1988) R29.

[3] H. Ohno, H. Munekata, T. Penny, S. von Molnar and L. L. Chang, *Phys. Rev. Lett.* 68 (1992) 2664.

[4] G. A. Prinz, *Science* 282 (1998) 1660.

[5] S. A. Wolf, D. D. Awschalom, R. A. Buhrman, J. M. Daughton, S. von Molnar, M. L. Roukes, A. Y. Chtchelkanova and D. M. Treger, *Science* 294 (2001) 1488.

[6] G. A. Prinz, *J. Magn. Magn. Mater.* 200 (1999) 57.

[7] B. D. Culity, *Introduction to Magnetic Materials* (Addison-Wesley Publishing Company, Inc. Massachusetts, 1972).

[8] A. R. West, *Solid State Chemistry and its Applications* (John Wiley & Sons, Singapore, 2003).

[9] R. C. O'Handley, *Modern Magnetic Materials* (Wiley-Interscience Publication, New York, 2000).

[10] K. H. J. Buschow and F. R. De Boer, *Physics of Magnetism and Magnetic Mateirlas* (Kluwer Academic /Plenum Publishers, New York, 2003).

[11] E. du Tremolet de Lacheisserie, D. Gignoux and M. Schlenker (Eds.), *Magnetism Fundamentals* Kluwer Academic Publishers, 2003).

[12] L. Neel, *Annales de physique* 18 (1932) 5-105.

[13] J. L. Dormann, D. Fiorani and E. Tronc, *J. Magn. Magn. Mater.* 202 (1999) 251.

[14] R. Wood, *IEEE Trans. Magn.* 36 (2000) 36.

[15] R. Hergt, W. Andra, C. G. d'Ambly, I. Hilger, W. A. kaiser, U. Richter and H. -G. Schmidt, *IEEE Trans. Magn.* 34 (1998) 3475.

[16] X. Batle and A. Labarta, *J. Phys. D: Appl. Phys.* 35 (2002) R15.

[17] A. Moser, K. Takano, D. T. Margulies, M. Albrecht, Y. Sonobe, Y. Ikeda, S. Sun and E. E. Fullerton, *J. Phys. D: Appl. Phys.* 35 (2002) R157.

[18] V. Skumryev, S. Stoyanov, Y. Zhang, G. Hadjipanayis, D. Givord and J. Nogues, *Nature* 423 (2003) 850.

[19] J. B. Goodenough, *Magnetism and Chemical Bond* (John Wiley & Sons: New York, 1963).

[20] J. P. Joule, *Ann. Electr. Magn. Chem.* 8 (1842) 219.

[21] D. C. Jiles, *Introduction to Magnatism and Magnetic Materials* (Chapman, & Hall, New York, 1998).

[22] E. Villari, *Ann. Phys. Chem.* 6 (1865) 87.

[23] G. Wiedemann, *Ann. Phys. Chem.* 117 (1862) 193.

[24] A. Beth, W. W. Meeks, *Rev. Sci. Instr.* 25 (1954) 603.

[25] H. HaSe and R. Shoji, *US Patent* 5442966 (1994).

[26] I. Sasada, A. Hiroike and K. Harada, *IEEE Trans. Magn., MAG-20* 951 (1984).

[27] K. Mohri, *IEEE Trans. Magn., MAG-20* 924 (1984).

[28] M. Liniers, V. madurga, M. Vazquez and A. Hernando, *Phys. Rev.* B 31 (1985) 4425.

[29] I. J. Garshelis and C. A. Jones, *J. Appl. Phys.* 85 (1999) 5468.

[30] W. J. Fleming, *IEEE Trans. Vehi. Tech.* 38 (1989) 159.

[31] M. J. Sablik and D. C. Jiles, *IEEE Trans. Magn.* 35 (1999) 498.

[32] M. J. Sablik and D. C. Jiles, *J. Phys. D: Appl. Phys.* 32 (1999) 1971.

[33] W. J. Fleming, *Society of Automotive Engineers* 890482 and 890483 (1989).

[34] C. A. Rogers, *Sci. Am.* 122 (1995) 65.

[35] S. Legvold, J. Alstad and J. Rhyne, *Phys. Rev. Lett.* 10 (1963) 509.

[36] A. E. Clark and H. S. Belson *Phys. Rev.* B 5 (1972) 3642.

[37] S. Chikazumi, *Physics of Magnetism* (John Wiley & Sons Inc, New York, 1964).

[38] M. Doerr, M. Rotter and A. Lindbaum, *Adv. Phys.* 54 (2005) 1.

[39] K. H. J. Buschow and R. P. van Stapele, *J. Appl. Phys.* 41 (1970) 4066.

[40] J. Farrell and W. Wallace, *Inorg. Chem.* 5 (1966) 105.

[41] A. Abrahams, R. Bernstein, J. Sherwood, J. Wernick and H. Williams, *J. Phys. Chem. Solids.* 25 (1964) 1069.

[42] K. A. Gschneidner, *J. Less Common Metals* 114 (1985) 29.

[43] G. Engdahl, *Handbook of Giant Magnetostrictive Materials* (Academic Press, Sandiego, 2000).

[44] E. du Trmolet de Lacheisserie, k. Mackay, J. Betz and J. C. Peuzin, *J. Alloy. Comp.* 275-277 (1998) 685.

[45] H. Uchida, Y. Matsumura, H. Uchida and H. Kaneko, *J. Magn. Magn. Mater.* 239 (2002) 540.

[46] F. Sayetat, *J. Magn. Magn. Mater.* 58 (1986) 334.

[47] F. Licci and S. Rinaldi, *J. Appl. Phys.* 52 (1981) 2442.

[48] M. R. Ibarra, P. A. Algarabel, C. Marquina, J. Blasco and J. Garcia, *Phys. Rev. Lett.* 75 (1995) 3541.

[49] J. M. D. Teresa, J. Blasco, M. R. Ibarra, J. Garcia, C. Marquina, P. A. Algarabel and A. D. Moral, *J. Appl. Phys.* 79 (1996) 5175.

[50] H. Khuwahara, Y. Tomioka, A. Asamitsu, Y. Mortitomo and Y. Tokura, *Science* 270 (1995) 961.

[51] B. Dabrowski, L. Gladczuk, A. Wisniewski, Z. Bukowski, R. Dybzinski, A. Szewczyk, M. Gutowsla and H. Szymczak, *J. Appl. Phys.* 87 (2000) 3011.

[52] F. Rivadulla, L. E. Hueso, D. R. Miguens, P. Sande, A. Fondado, J. Rivas, M. A. Lopez-Quintela and C. A. Ramos, *J. Appl. Phys.* 91 (2002) 7412.

[53] J. S. Gwag, H. Kim and J. W. Kim, *J. Appl. Phys.* 93 (2003) 1142.

[54] R. Mahendiran, M. R. Ibarra, C. Marquina, B. Garcia-Landa, L. Morellon, A. Maignan, B. Raveau, A. Arulraj and C. N. R. Rao, *Appl. Phys. Lett.* 82 (2003) 242.

[55] J. M. D. Teresa, M. R. Ibarra, J. Blasco, J. Garcia, C. Marquina, P. A. Algarabel, Z. Arnold, K. Kamenev, C. Ritter and R. van Helmolt, *Phys. Rev.* B 54 (1996) 1187.

[56] M. R. Ibarra, R. Mahendiran, C. Marquina, B. Garcia-Landa and J. Blasco, *Phys. Rev.* B 54 (1998) R327.

[57] I. O. Tryonchauk, N. V. Samsonenko, A. Nabialek and H. Szymczak, *J. Magn. Magn. Mater.* 168 (1997) 309.

[58] D. N. Argyriou, J. F. Mitchell, C. D. Potter, S. D. Bader, R. Kleb and J. D. Jorgenson, *Phys. Rev.* B 55 (1997) R111965.

[59] R. V. Demin, L. I. Koroleva and A. M. Balbashov, *Phys. Lett.* A 231 (1997) 279.

[60] Y. F. Popov, A. M. kadomtseva, G. P. Vorob'ev, V. Y. Lvanov, A. K. Mukhin, A. K. Zvezdin and A. M. balbashov, *J. Appl. Phys.* 83 (1998) 7160.

[61] B. Garcia-Landa, J. M. De. Terrsa, M. R. Ibarra, C. Ritter, R. Drost and M. R. Lees, *J. Appl. Phys.* 83 (1998) 7664.

[62] A. K. Pradhan, B. K. Roul, Y. Feng, Y. Wu, S. Mohanty, D. R. Sahu and P. Dutta, *Appl. Phys. Lett.* 78 (2001) 1598.

[63] D. A. Filippov, R. Z. Levitin, A. N. Vasil'ev, T. N. Voloshok, H. kageyama and R. Suryanarayanan, *Phys. Rev.* B 65 (2002) 100404.

[64] H. Ogawasara, M. Matsukawa, M. Yoshizawa, M. Apostu, R. Suryanarayanan, G. Dhalenne, A. Revcolevschi, K. Itoh and N. Kobayashi, *J. Magn. Magn. Mater.* 226-230 (2001) 990.

[65] C. Marquina, M. R. Ibarra, A. I. Abromovich, A. V. Michurin and L. I. Koroleva, *J. Magn. Magn. Mater.* 226-230 (2001) 999.

[66] A. Abramovich, L. Koroleva, A. Michurin, O. Gorbenko and A. kaul, *J. Magn. Magn. Mater.* 242-245 (2002) 648.

[67] A. Abramovich, L. Koroleva and A. Michurin, *J. Magn. Magn. Mater.* 258-259 (2003) 319.

[68] J. Wu and S-Y. Zhang, *J. Magn. Magn. Mater.* 264 (2003) 102.

[69] R. V. Demin, L. I. Korelva, R. V. Privezentsev and N. A. Kozlavskaya, *Phys. Lett.* A 325 (2004) 426.

[70] D. Serrate, J. M. D. Teresa, P. A. Algarabel, C. Marquina, L. Morellon, J. Blasco and M. R. Ibarra, *J. Magn. Magn. Mater.* 290-291 (2005) 843.

[71] M. Doerr, G. Remenyi, M. Rotter, S. Sahling, M. Saint-Paul and M. Loewenhaupt, *J. Magn. Magn. Mater.* 290-291 (2005) 906.

[72] B. A. Hunter, B. J. Kenned and T. Vogt, *Phys. Rev.* B 69 (2004) 020410.

[73] H. Szymczak, *J. Magn. Magn. Mater.* 211 (2000) 186.

[74] J. Smith and H. P. J. Wijn, *Ferrites* (Philiphs Technical Library, Eindhoven, 1953)

[75] R. M. Bozorth and R. W. Hamming, *Phys. Rev.* 89 (1953) 865.

[76] R. M. Bozorth, E. F. Tilden and A. J. Williams, *Phys. Rev.* 99 (1955) 1788.

[77] C. Guillad, *Rev. Mod. Phys.* 25 (1953) 64.

[78] L. R. Bickford, J. Pappis and J. L. Stull, *Phys. Rev.* 99 (1955) 1210.

[79] Y. Chen, J. E. Snyder, K. W. Dennis, R. W. McCallum and D. C. Jiles, *J. Appl. Phys.* 87 (2000) 5798.

[80] R. W. McCallum, K. W. Dennis, D. C. Jiles, J. E. Snyder and Y. H. Chen, *Low Temp. Phys.* 27 (2001) 266 .

[81] J. A. Paulsen, A. P. Ring, C. C. H. Lo, J. E. Snyder and D. C. Jiles, *J. Appl. Phys.* 97 (2005) 044502.

[82] M. Pasqale, *Journal of Magnetics* 8 (2003) 60.

[83] C. H. Joshi, *Proceedings of Conference Actuator* (Germany, June, 2000).

[84] J. M. Varnish, D. P. Naik, J. B. Restorff and J. P. Teter, *IEEE Trans. Magn.* 27 (1991) 5355.

[85] D. A. Bushko and G. H. Goldie, *IEEE AES Syst. Mag.* 21 (1991) 5.

[86] B. Viswanathan and V. R. K. Murthy, *Ferrite Materials: Science and technology* (Narosa Publishing House, New Delhi, 1990).

[87] I. C. Heck, *Magnetic Materials and their Applications* (Butterworth & Co. Pub. Ltd, London, 1974).

[88] A. Goldman, *Modern Ferrite Technology* (Van Nostrand Reinhold, New York, 1990).

[89] K. E. Sickafus and J. M. Wills, *J. Am. Ceram. Soc.* 82 (1999) 3279.

[90] F. S. Galasso, *Structure and Properties of Inorganic Solids* (Pergamon Press, Oxford, 1970).

[91] R. W. G. Wyckoff, *Crystal Structures: Miscellaneous Inorganic Compounds, Silicates and basic structural information* Vol.4, 2nd ed. (Interscience Publishers, New York, 1968), pp. 540.

[92] R. Valenzuela, *Magnetic Ceramics, Chemistry of Solid State Materials* Series Ed. B. Dunn, J. W. Goodby and A. R. West, (Cambridge Univ. Press, Cambridge, 1994).

[93] A. B. V. Groenu, P. F. Bongers and A. L. Stuyts, *Mater. Sci. Eng.* 3 (1968-69) 317.

[94] B. Lax and K. J. Button, *Microwave Ferrites and Ferrimagnetics* (McGraw Hill Book Company, New York, 1962).

[95] R. J. Teitel and M. Cohen, *Trans. AIME* 188 (1950) 1028.

[96] G. A. Sawatzky, F. VAN DER Woude and A. H. Morrish, *J. Appl. Phys.* 39 (1968) 1204.

[97] C. H. Yan, Z-G. Xu, F.-X. Cheng, Z. -M. Wang, L. -D. Sun, C. -S. Liao and J. -T. Jia, *Solid. State. Commun.* 111 (1999) 287.

[98] E. J. Choi, Y. Ahn, S. Kim, D. H. An, K. U. Kang, B-G. Lee, K. S. Baek and H. N. Oak, *J. Magn. Magn. Mater.* 262 (2003) L198.

[99] G. B. Ji, H. L. Su, S. L. Tang and B. L. Xu, *Chem. Lett.* 34 (2005) 86.

[100] C. C. H. Lo, A. P. Ring, J. E. Snyder and D. C. Jiles, *IEEE Trans. Magn.* 41 (2005) 3676.

[101] R. H. Mitchel, *Perovskites: Modern and Ancient* (Almaz Press, Thunder Bay, Canada 2002).

[102] A. Von Hippel, *Rev. Mod. Phys.* 22 (1950) 221.

[103] J. G. Bednorz and K. A. Muller, *Z. Phys. B: Condens. Matter* 64 (1986) 189.

[104] S. Jin, T. H. Tiefel, M. McCormack, R. A. Fastnacht, R. Ramesh and L. H. Chen, *Science* 264 (1994) 413.

[105] V. M. Goldschmidt, *Akad. Oslo. J. Natur.* 2 (1926) 7.

[106] H. D. Megaw, *Trans. Farady Soc.* A42 (1946) 133.

[107] J. B. Goodenough, *Annu. Rev. Mater. Sci.* 28 (1998) 1.

[108] J. M. D. Coey and D. Khalafalla, *Phys. Stat. Sol.* (a) 11 (1971) 229.

[109] J. B. Goodenough, A. Wold, R. J. Arnott and N. Menyuk, *Phys. Rev.* 124 (1961) 373.

[110] J. B. A. A. Elemans, B. Van Laar, K. R. Van Der Veen and B. O. Loopstra, *J. Solid State Chem.* 3 (1971) 238.

[111] K. Terakura, I. V. Solovyev and H. Sawada, in: *Colosssal Magnetoresistve Oxides* Y. Tokura, (Ed.), (Gordan and Breach Science Publishers, The Netherlands, 2000).

[112] R. V. Krishnan and A. Banerjee, *J. Phys.: Condens. Matter* 12 (2000) 3835.

[113] Z. El-Faldi, M. R. Metni, F. Sapina, E. Martinez, J. V. Folgado, D. Beltran and A. Beltran, *J. Mater. Chem.* 10 (2000) 437.

[114] E. J. Cussen, M. J. Rosseinsky, P. D. Battle, J. C. Burley, L. E. Spring, J. F. Vente, S. J. Blundell, A. I. Coldea and J. Singleton, *J. Am. Chem. Soc.* 123 (2001) 1111.

[115] T. F. Mitchell, D. N. Argyriou and J. D. Jorgensen in: *Colosssal Magnetoresistve Oxides* Y. Tokura, (Ed.), (Gordan and Breach Science Publishers, The Netherlands, 2000).

[116] G. H. Jonker and J. H. van Santen, *Physica* 16 (1950) 377.

[117] J. H. van Santen and G. H. Jonker, *Physica* 16 (1950) 599.

[118] C. N. R. Rao and B. Raveau (Eds.), *Colosssal Magnetoresistance, Charge Ordering and Related Properties of Manganese Oxides* (World Scientific, Singapore, 1998).

[119] J. M. D. Coey, M. Viret and S. van Molnar, *Adv. Phys.* 48 (1999) 167.

[120] Y. Tokura (Ed.), *Colosssal Magnetoresistve Oxides* (Gordan and Breach Science Publishers, The Netherlands 2000).

[121] J. B. Goodenough, *Phys. Rev.* 100 (1955) 564.

[122] C. Zener, *Phys. Rev.* 82 (1951) 403.

[123] P. W. Anderson and H. Hasegawa, *Phys. Rev.* 100 (1955) 675.

[124] P. -G. de Gennes, *Phys. Rev.* 118 (1960) 141.

[125] Z. S. Gonen, J. Gopalakrishanan, S. A. Sirchio, B. W. Eichhorn, V. Smolyaninova and R. L. Greene, *J. Solid State Chem.* 159 (2001) 68.

[126] T. R. N. Kutty and J. J. Philip, *J. Phys.: Condens. Matter* 12 (2000) 7747.

[127] S. Hebert, C. Martin, A. Maignan, R. Rotoux, M. Hervieu, N. Nguyen and B. Raveau, *Phys. Rev.* B 65 (2002) 104420.

[128] N. R. Washburn, A. M Stacy and A. M Portis, *Appl. Phys. Lett.* 70 (1997) 1622.

[129] N. R. Washburn, A. M Stacy and A. M Portis, *J. Phys. Chem.* B 104 (2000) 1447.

[130] L. Hu, W. Tong, H. Zhu and Y. Zhang, *J. Phys.: Condens. Matter* 15 (2003) 2033.

[131] J. B. Goodenough, R. I. Dass and J. Zhou, *Solid State Sciences* 4 (2002) 297.

[132] J. Topfer and J. B. Goodenough, *Eur. J. Solid State Inorg. Chem.* 34 (1997) 467.

[133] J. -S. Zhou, H. Q. Yin and J. B. Goodenough, *Phys. Rev.* B 63 (2001) 184423.

[134] B. Vertruyen, S. Hebert, A. Maignan, C. Martin, M. Hervieu and B. Raveau, *Cryst. Engineering* 5 (2002) 299.

[135] G. H Jonker, *Physica* 22 (1956) 707.

[136] L. Morales, A. Caneiro, R. D. Sanchez and D. Vega, *J. Magn. Magn. Mater.* 226-230 (2001) 806.

[137] L. Morales, A. Caneiro, D. Vega, R. Zysler, H. Lanza and R. C. Mercader, *J. Solid State Chem.* 168 (2002) 100.

[138] A. E. Teplykh, A. N. Pirogov, A. Z. Men'shikov and G. V. Bazuev, *Physica* B 276-278 (2000) 574.

[139] U. H. Bents, *Phys. Rev.* 106 (1957) 225.

[140] M. Hrovat, S. Bernik, J. Holc, D. Kuscer and D. Kolar, *J. Mater. Sci. Lett.* 16 (1997) 143.

[141] H. Taguchi, S. -I. Matsu-ura, M. Nagao and H. Kido, *Physica* B 270 (1999) 325.

[142] L. W. Zhang, G. Feng, H. Liang, B. S. Cao, Z. Meihong and Y. G. Zhao, *J. Magn. Magn. Mater.* 219 (2000) 236.

[143] R. Gundakaram, A. Arulraj, P. V. Vanitha, C. N. R. Rao, N. Gayathri, A. K. Raychaudhuri and A. K. Cheetham, *J. Solid State Chem.* 127 (1996) 354.

[144] Y. Sun, W. Tong, X. Xu and Y. Zhang, *Phys. Rev.* B 63 (2001) 174438.

[145] J. Deisenhofer, M. Paraskevopoulos, H. -A. K. von Nidda and A. Loidl, *Phys. Rev.* B 66 (2002) 054414.

[146] G. H. Jonker, *J. Appl. Phys.* 37 (1996) 1424.

[147] V. Narasimhan, H. V. Keer and D. K. Chakrabarty, *Phys. Stat. Sol.* (a) 89 (1985) 65.

[148] M. A. Gilleo, *Acta. Cryst.* 10 (1957) 161.

[149] A. Wold, R. J. Arnott and J. B. Goodenough, *J. Appl. Phys.* 29 (1958) 387.

[150] N. V. Minh, S. -J. Kim and I. -S. Yang, *Physica* B 327 (2003) 208.

[151] I. O. Troyanchuk, L. S. Lobanovsky, D. D. Khalyavin, S. N. Pastushonok and H. Szymczak, *J. Magn. Magn. Mater.* 210 (2000) 63.

[152] N. Y. Vasanthacharya, P. Ganguly, J. B. Goodenough and C. N. R. Rao, *J. Phys. C: Solid State Phys.* 17 (1984) 2745.

[153] P. A. Joy, Y. B. Khollam and S. K. Date, *Phys. Rev.* B 62 (2000) 8608.

[154] V. L. J. Joly, P. A. Joy, S. K. Date and C. S. Gopinath, *Phys. Rev.* B 65 (2002) 184416.

[155] Y. Wu, Z. Yu and S. Liu, *J. Solid State Chem.* 112 (1994) 157.

[156] J. J. Blanco, L. Lezama, M. Insausti, J. Gutierrez, J. M. Barandiaran and T. Rojo, *Chem. Mater.* 11 (1999) 3464.

[157] M. Pissas, G. Kallias, E. devlin, A. simopoulos and D. Niarchos, *J. Appl. Phys.* 81 (1997) 5770.

[158] W. Tong, B. Zhang, S. Tan and Y. Zhang, *Phys. Rev.* B 70 (2004) 014422.

[159] Y. Miwa, A. Yamamoto, K. Oda and H. Otsuka, *Trans. Mater. Res. Soc. Jpn.* 25 (2000) 1057.

[160] K. Oda, Y. Miwa and H. Ohtsuka, *Hyperfine Interact.* 139-140 (2002) 569.

[161] K. H. Ahn, X. W. Wu, K. Liu and C. L. Chien, *Phys. Rev.* B 54 (1996) 15299.

[162] L. Righi, P. Gorria, M. Insausti, J. Gutierrez and J. M. Barandiaran, *J. Appl. Phys.* 81 (1997) 5767.

[163] L. Righi, P. Gorria, M. Insausti, J. Gutierrez and J. M. Barandiaran, *J. Appl. Phys* 81 (1997) 5767.

[164] J. Gutierrez, A. Pena, J. M. Barandiaran, J. L. Pizarro, T. Hernandez, L. Lezama, M. Insausti and T. Rojo, *Phys. Rev.* B 61 (2000) 9028.

[165] M. Rubinstein, D. J. Gillespie, J. E. Snyder and T. M. Tritt, *Phys.Rev.* B 56 (1997) 5412.

[166] H. Tanaka, N. Okawa and T. Kawai, *Solid State Commun.* 110 (1999) 191.

[167] K. Ueda, H. Tabata and T. Kawai, *Phys. Rev.* B 60 (1999) R12561.

[168] K. Ueda, Y. Muraoka, H. Tabata and T. Kawai, *Appl. Phys. Lett.* 78 (2001) 512.

[169] V. L. Joseph Joly, S. D. Bhame, P. A. Joy and S. K. Date, *J. Magn. Magn. Mater.* 261 (2003) 433.

Chapter 2

Experimental Methods

2.1 Introduction

This chapter discusses the different methods of synthesis and various experimental techniques used for the characterization of different materials studied in the present work. Such techniques involve the methods of synthesis of the oxides under study and characterization of the structure, microstructure, magnetic properties, sintering behavior, density measurements, magnetostriction measurements, etc. In the following discussions and all other chapters, the unit of temperature for material processing and magnetic measurements above room temperature is expressed in degrees Celsius as most of the thesis deals with the processing of materials at higher temperatures. For magnetic measurements below room temperature, the unit of temperature is expressed in degrees Kelvin.

2.2 Synthesis

There are several methods available for the synthesis of oxide materials in the bulk as well as nanosized forms such as ceramic, sol-gel, citrate precursor method, combustion, co-precipitation, etc [1, 2]. The most commonly used method is the ceramic or the high-temperature method. In the present work the different oxide materials were synthesized in the bulk as well as nanosized forms by using different methods, especially the conventional ceramic method and the glycine-nitrate autocombustion method. Apart from these two synthesis methods, the citrate precursor route and the coprecipitation methods were also been used for the synthesis of nanocrystalline cobalt ferrite.

2.2.1 Ceramic Method

Cobalt ferrite and substituted cobalt ferrites were mostly synthesized by the solid state or the ceramic method of synthesis which is one of the commonly used method for preparing metal oxides and other solid materials. In the ceramic or solid state process, the constituent oxides, carbonates, oxalates, etc., are weighed in the required stoichiometric ratio and are mixed thoroughly using a mortar and pestle with the help of a mixing medium [1, 3, 4]. After thorough grinding, the ground dry powder is pre-calcined at a higher temperature. After the pre-calcination, the resulting powder is ground again and is repeatedly fired at elevated temperatures, with intermediate grindings, till the desired compound is obtained. Many a times the powder is compacted in the form of a pellet to ensure better reactivity between the constituents. In the present work cobalt ferrite and Mn substituted cobalt ferrites have been prepared from Fe_2O_3, $CoCo_3$ and MnO_2. Stoichiometric amounts of these starting materials were mixed with the help of acetone as the mixing medium. The dry mixed powders were first pre-calcined at 1000 °C for 12 hours and then furnace cooled. The resulting powders were then ground at then again heated at 1000 °C for 24 hours and 1100 °C for 72 hours with intermediate grinding after every 24 hours of heating.

2.2.2 Ball Milling

Ball milling is an important method for the preparation of materials both for the investigation of fundamental physical properties and for a number of possible commercial applications [5]. Ball mills rotate around a horizontal axis, partially filled with the material to be ground plus the grinding medium. Different materials are used as the medium, including ceramic balls, flint pebbles and stainless steel balls. An internal cascading effect reduces the material to a fine powder. The amount of milling determines the particle size distribution which in turn affects the material homogeneity and the final microstructure after sintering [6]. In the present study, cobalt ferrite powder was prepared using cobalt carbonate and iron oxide as starting materials. Stoichiometric amounts were weighed and properly mixed in a ball mill for 24 h, using acetone as the mixing medium. Stainless steel balls with diameter 20 mm were used. This mixed powder was then preheated at 1000 °C for 12 h and again heated for 12 h after an intermediate grinding. Final heating was performed in a programmable furnace at 1100 °C for 72 h with 2 intermediate grindings after every 24 h. The final powder obtained was balled milled for 8 h in order to reduce the particle size of the ferrite powder. Ball milling was performed using stainless steel balls in a plastic container with distilled water as milling medium. The milled powder was further sieved through 100 and 200 mesh sieves and used for further characterization and sintering studies.

2.2.3 Low-Temperature Methods

Glycine-Nitrate Autocombustion Method

Apart from the conventional ceramic method, the materials in the present study were also synthesized by the low-temperature routes such as the autocombustion method of synthesis involving the metal nitrates as oxidizing reagents. The combustion method is very useful for synthesizing homogeneous materials at very low temperatures. The autocombustion process of synthesis offers several distinct advantages over other methods of synthesis. It ensures the mixing of metal ions at a molecular level thereby leading to homogeneous powders. Also, shorter reaction times, low temperatures involved, large scale synthesis, high phase purity, fine particle nature of the products obtained, are some of the salient features of this method. In the combustion method fuels like glycine, urea, citric acid, hydrazine, glycerol, etc, are used along with oxidizing agents such as metal nitrates [7–15]. The amino acid, *glycine* plays two major roles in the synthesis. Firstly, it forms a complex with metal ions involved, acting as a bidentate ligand. The two different end groups *i.e.*, the carboxylic group and the amino group can be utilized for complex formation. The zwitterionic character of glycine allows effective complexation with metal ions of varying ionic size. Also it enhances the solubility of metal ions thereby avoiding selective precipitation when water is evaporated. The method is actually self-sustainable after the reaction is initiated and owing to the exothermic nature of the reaction, high internal temperature ensures the crystallization and formation of the oxides [7, 16, 17]. The complete combustion reaction for the divalent and trivalent metal nitrates can be represented as shown in equations 2.1 and 2.2 respectively.

$$M(NO_3)_2 + \frac{10}{9}C_2H_5O_2N = MO + \frac{20}{9}CO_2 + \frac{25}{9}H_2O + \frac{14}{9}N_2 \tag{2.1}$$

$$2M(NO_3)_3 + \frac{30}{9}C_2H_5O_2N = M_2O_3 + \frac{60}{9}CO_2 + \frac{75}{9}H_2O + \frac{42}{9}N_2 \tag{2.2}$$

The substituted perovskite manganites studied in the present work as well as cobalt ferrite were synthesized by the glycine-nitrate autocombustion method. For the synthesis of oxides, stoichiometric quantities of the corresponding metal nitrates were individually dissolved in minimum amount of distilled water. The metal to glycine ratio was maintained as 1:2. The solutions of the respective metal nitrates and glycine were mixed together in a large crystallizing dish. The final mixed solution (in the crystallizing dish) was kept over a hot plate for evaporation and autocombustion, at a temperature of $\sim$200 °C. A viscous gel formed at the bottom of the dish after the complete evaporation of water subsequently underwent autocombustion producing a fluffy mass within few seconds (as-synthesized product). The obtained powder was then used for different studies.

Coprecipitation Method

This method is a precursor method for the formation of oxides, in which metal ions (usually nitrates or chlorides of corresponding metal ions) are precipitated together as decomposable salts by adding excess of precipitating reagent. The aqueous solution of metal ions can be precipitated in the form of hydroxides, oxalates, carbonates, etc. This method ensures the molecular level mixing of the starting components and lead to smaller sized particles. The precipitate after thorough washings can be thermally decomposed at a relatively lower temperature to give the corresponding oxides. The uniform mixing during precipitation reduces the temperature for the diffusion of ions during the solid state reaction. The advantages of coprecipitation method are its ability to deliver products having greater homogeneity, greater reactivity, high purity, fine particle size along with the elimination of higher temperatures required for calcining. In the present work, the synthesis of cobalt ferrite powder was carried out using cobalt and iron nitrates taken in the stoichiometric ratio and dissolved in distilled water. 20% KOH solution was added drop wise to this solution under constant magnetic stirring. A precipitate formed was filtered and washed several times with distilled water until the pH of the filtrate was ∼7. The precipitate was dried overnight in an oven at 100 °C which eventually converted to a black powder.

Citrate Method

The citrate gel method is commonly used for the synthesis of oxides. In this method the soluble metal salts are used and citric acid is used as a complexating agent. For the synthesis of cobalt ferrite using the citrate precursor method, stoichiometric amounts of metal nitrates were dissolved in distilled water. Water solution of citric acid was added to the mixed metal ions solution keeping the metal to citric acid ratio as 1:2. The solution was evaporated on a water bath and finally a thick gel was formed. This precursor was dried overnight in an oven at 100 °C and the dried precursor was calcined at 500 °C for 4 hours to get the cobalt ferrite powder.

2.3 Characterization and Measurement Techniques

2.3.1 Powder X-Ray Diffraction

The materials studied in the present work have been phase identified by the powder X-ray diffraction (XRD) method. X-ray diffraction is the most important and useful technique in the field of solid state chemistry. Powder XRD is used to determine the structure of the crystalline materials without the need for large single crystals. The XRD pattern is the finger print of a crystalline material [18, 19] as this technique gives information on the structure, phase and purity of a material. The Bragg's law is used widely to treat diffraction from crystals. The Bragg's law is given as

$$n\lambda = 2dsin\theta \tag{2.3}$$

where d is the spacing between two adjacent lattice planes, λ is the wave length of the X-radiation, n is an integer (=1) and θ is known as the diffraction angle or Bragg's angle [18].

It is known that the width of a diffraction peak increases when the crystallite size is reduced below a certain limit ($<$ 100 nm). Therefore, XRD patterns can be used to estimate the average size of very small crystallites, from the measured width of the peaks in the diffraction patterns. The commonly accepted formula for the determination of crystallite size from XRD line broadening is the Scherrer formula [18],

$$t = \frac{0.9\lambda}{\beta cos\theta_B} \tag{2.4}$$

where t is the thickness of the crystallites (in Å), λ is the X-ray wavelength, θ_B is the diffraction angle and β is the width of the diffraction peak. Generally, there will be a contribution to line broadening from the instrument due to various factors and this natural line width is corrected as

$$\beta^2 = \beta_M^2 - \beta_S^2 \tag{2.5}$$

where β_M is the measured peak width at half peak height and β_S is the contribution from the instrumental line broadening, in radians. β_S is obtained from the width of the XRD pattern of a standard bulk material. The thickness of the crystallite or the average crystallite size t is generalized as the average particle size in the following chapters.

In the present study, the phase analysis of the samples was carried out using a Philips PW 1830 diffractometer, and using Ni-filtered Cu Kα radiation. The wavelength of Cu Kα radiation is 1.5418 Å. The diffractometer was calibrated with reference to standard Si wafer. For the general phase analysis the scan rate used was 4 °/minute. The lattice parameters and d-spacings were calculated using the computer programs, Powder Diffraction Package (PDP) [20] and PowderCell for Windows (PCW) [21].

2.3.2 Transmission Electron Microscopy (TEM)

Transmission electron microscopy (TEM) is an imaging technique whereby a beam of electrons is focused onto a specimen causing an enlarged version to appear on a fluorescent screen or a layer of photographic film, or to be detected by a CCD camera. TEM operates on the same basic principles as the light microscope but uses electrons instead of light. Virtually, TEM is useful for determining size, shape and arrangement of the particles which make up the specimen. Moreover, it is highly useful for determination of the lattice planes and the detection of atomic-scale defects in areas of few nanometers in diameter with the help of selected area electron diffraction (SAED) technique [22, 23]. The d-spacing between lattice planes of crystalline materials can be calculated from a SAED pattern using the relationship,

$$dr = \lambda L \tag{2.6}$$

where L is the distance between the specimen and the photographic plate, λL is known as the camera constant and r is the radius of diffracted rings. It is easy to measure r directly from the photographic plate, and λL can be established from the instrument by calibrating it with a standard material (usually Ag), and hence one can easily get d values. Since each d value corresponds to a specific lattice plane for a specific crystal structure, a minimum description of the crystal structure of a crystalline specimen can be obtained from a SAED pattern. In some cases, SAED pattern is more helpful as compared to XRD, due to the limited detection limit of XRD instruments.

In the present work, the TEM measurements were performed on a Jeol model 1200 EX instrument operating at 120 kV, camera length of 80 cm and field limited aperture of 100 μm. Prior to TEM measurements, the samples were dispersed in a suitable organic solvent (isoamyl acetate, acetone, toluene, etc.) and a drop of the solution was poured on carbon-coated TEM grids. The film formed on the TEM grids was allowed to dry for 2 minutes following which the extra solvent was removed using a blotting paper and the TEM measurements were performed.

2.3.3 Scanning Electron Microscopy (SEM)

The scanning electron microscope (SEM) is a very useful instrument to get information about topography, morphology, composition and microstructural information of materials. It is a type of electron microscope capable of producing high resolution images of a sample surface. Due to the manner in which the image is created, SEM images have a characteristic three-dimensional appearance and are useful for judging the surface structure of the sample. The SEM has compensating advantages, including the ability to image a comparatively large area of a specimen and the ability to image bulk materials [24]. SEM images are much easier to interpret than TEM images, and many SEM images, beyond their scientific value, are actually beautiful. Particle topology of the powder samples and microstructure of the sintered samples in the present study were obtained using a Leica Stereoscan-440 scanning electron microscope. For the analysis of a powder sample's morphology, the sample powder was spread on an Al holder using isoamyl acetate. On the other hand, sintered pellets were fractured to expose the inner portion and mounted on a specimen mounting stub. Silver paste was used to connect the sample to the sample holder for electrical conduction. A thin layer of gold was coated on the surface of the sample to avoid charging of the specimen.

2.3.4 Thermo-Mechanical Analysis

Thermo mechanical analyzer (TMA) is an instrument used to measure thermo mechanical characteristics such as thermal expansion, thermal contraction, and softening of various materials. Moreover, this technique is highly useful to measure the stress and strain of polymers. TMA provides measurement of penetration, expansion, contraction and extension of material as a function of temperature. It consists of a probe connected

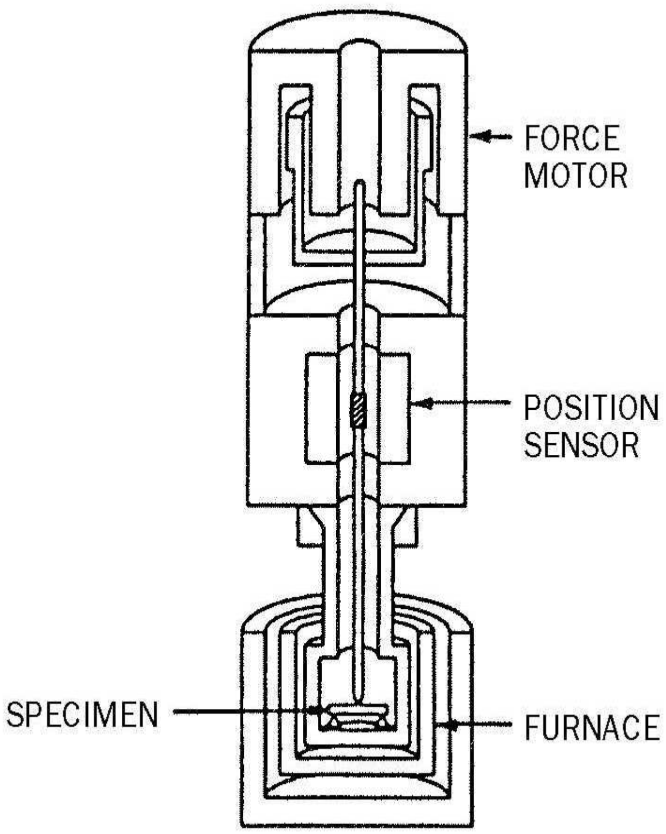

Figure 2.1: Schematic diagram for a Thermo-Mechanical Analyzer.

mechanically to the core of a linear variable differential transformer. The core is coupled to the sample by means of a quartz probe that contains a thermocouple for measurement of sample temperature. Any movement of the sample is translated in to moment of transformer core and result in a output signal, proportional to the displacement of the probe. In the penetration and expansion modes, the sample rests on a quartz stage surrounded by a furnace. Under no load, expansion with temperature is observed. We can calculate the coefficient of linear expansion from the slope of the resulting curve. A weight tray attached to the upper end of the probe allows a predetermined force to be applied to the samples to study variation under load. Probes with small tip and loaded with weight tray are used for sensitive detection of softening temperature and glass transition. Larger tip diameters and zero loading are used in the expansion mode. Sample sizes usually range from few microns of coating to $\sim$1 cm thick solid.

In the present study, a Perkin-Elmer instrument, Pyris Diamond TMA (Thermal Mechanical Analyzer) was used to study the sintering behavior of the ferrite samples in terms of rate of liner shrinkage as a function of temperature. The temperature range employed is 30 °C to 1475 °C (the actual sample temperature attained was 1350 °C) at a heating rate of 10 °C/min. An alumina rod was used as the TMA probe. A thin sample pellet ($\sim$5 mm) was kept inside an alumina sample tube on an alumina plate and a constant force, 100 mN, was applied to it. An independently connected linear voltage differential transformer (LVDT) and core detected the changes in sample length as a function of temperature.

2.3.5 Mössbauer Spectroscopy

The Mössbauer spectroscopy technique is being used in many analytical, biological, geological and engineering research areas [25,26]. It is a branch of spectroscopic study, where resonant absoption of γ rays by the nuclei of atoms of a sample is studied. The Mössbauer spectroscopy is used as a fingerprint technique in mineralogy and geochemistry. Moreover, the existence of chemically, crystallographically or magnetically inequivalent sites are generally revealed by the appearance of distinct components arising from the different absorption peaks in a Mössbauer spectrum. There are basically two types of information that can be derived from a Mössbauer spectrum. The relative and absolute line energies are determined by electronic effects on the nuclear energy levels. These effects are generally lumped together as 'hyperfine parameters' and they are the isomer shift (or chemical shift, *IS*), electric quadruple hyperfine interaction (quadruple splitting, *QS*), and magnetic dipole hyperfine interaction (or magnetic hyperfine field, *HMF*) [26].

The room temperature Mössbauer spectra of the Fe substituted lanthanum manganite samples in the present work were obtained using an Austin Scientific Associates S-600 Mössbauer spectrometer coupled to a Canberra-95 multichannel analyzer. A Co^{57} in Rh matrix was used as the Mössbauer source. The spectrometer was calibrated with natural iron foil. The isomer shift is reported with respect to Fe metal and the data were analyzed using a standard computer program.

2.3.6 Infrared spectroscopy

The atoms in a molecule do not remain in a fixed relative position and vibrate about some mean position. Due to this vibrational motion if there is a periodic alternation in the dipole moment then such mode of vibration is infrared (IR) active. The IR region of the electromagnetic spectrum is 100 to 1 μ_m wavelength. The vibrating molecule absorbs energy only from radiation with which it can coherently interact, *i.e.* the radiation of its own oscillation frequency. The appearance or non-appearance of certain bands in an IR spectrua at certain vibrational frequencies gives valuable information about the structure of a particular molecule. The frequency of vibration is given by the relation

$$\nu = \frac{1}{2\pi}\sqrt{\frac{k}{\mu}} \tag{2.7}$$

where k is force constant and μ is reduced mass.

In the present work, the IR studies were carried out on the manganite samples using a Perkin Elmer Spectrum-One FTIR Spectrometer in the frequency range 400 to 4000 cm^{-1} by properly mixing the sample with spectroscopic grade KBr.

2.3.7 Electron Paramagnetic Resonance

When unpaired electrons exist in a substance, their spins are aligned at random in the absence of a field. When placed in a magnetic field , however, they will each have a preferred direction and, since the spin quantum number of an electron is 1/2 each can be thought of spinning either clockwise or anticlockwise about the field direction. EPR spectroscopy essentially measures the energy required to reverse the spin of an unpaired electron. This energy difference between the two spin states $m_s = +1/2$ and $m_s = -1/2$ corresponds to the frequencies in the microwave region. Thus, for a particular applied field strength, the absorption of microwave radiation of a particular frequency results in the resonance. However, in a typical EPR spectrometer, the experiments are generally carried out at a fixed frequency of microwave radiation and varying the magnetic field. Two common frequencies used are in the X-band range (∼9.5GHz, where a field strength of approximately 3400 gauss is used) and the Q-band frequency (35GHz, where a field strength of approximately 12,500 Gauss is employed) [27]. In the present work the measurements have been carried out using a Bruker ER-200D-SRC spectrometer at the X-band frequency regime at room temperature.

2.3.8 Density Measurements

Densities of the sintered discs were calculated from the volume (calculated from the measured diameter and thickness of the discs using a vernier calipers) and the weight of the discs as well as by the Archimedes method. These two methods gave comparable values of the densities. The relative density was calculated from the ratio of the measured density to the theoretical density calculated from the crystal structure parameters. The theoretical density is calculated from the relation

$$\rho = \frac{m}{V} \tag{2.8}$$

$$m = \frac{Z \times M}{N} \tag{2.9}$$

where M is the molecular weight, Z is the number of formula units per unit cell, N is Avagadro's number and V is the volume of the unit cell. For example, the theoretical density of $CoFe_2O_4$ can be calculated as shown below. The molecular weight of $CoFe_2O_4$ is 234.63 g. Spinel ferrites have eight formula units per unit cell. Therefore, the molecular weight of one cell is 8 × 234.63 = 1877.04 g. The volume of a cube of side length is a^3. The cubic unit cell length, a, of $CoFe_2O_4$ is 8.38 Å. Therefore, the volume volume of a unit cell is a^3 = 588.48 $Å^3$. 1 $Å^3 = 10^{-24}$ cm^3, and therefore, NV = 354.44 cm^3.

$$Density(D) = \frac{Mass}{Volume} = 1877.04/354.44 = \mathbf{5.2957} g/cm^3 \tag{2.10}$$

2.3.9 Magnetic measurements

The magnetic characteristics of the different materials as a function of the applied field at different temperatures and as a function of temperature at different applied field strengths were measured on a *Vibrating Sample Magnetometer* (VSM). A VSM is a device in which a sample is vibrated in an uniform magnetic field, and the induced voltage in a properly positioned set of coils, which is proportional to the magnetization of the material, is detected. The instrument allows precise magnetization measurements to be made as a function of magnetic field strength, temperature, and crystallographic orientation [28,29].

An EG&G PAR 4500 vibrating sample magnetometer was used in the present work. The magnetometer was calibrated using a standard Ni sample. Field dependance of magnetization was measured up to a maximum field of ± 15 kOe. For high temperature measurements, an electrically heated oven was attached to the VSM to heat the sample above room temperature. Here, a constant magnetic field is applied and the magnetization is measured by varying the temperature at a constant heating rate of 2 °C/min.

A closed cycle helium cryostat was used for low temperature measurements (12-300 K). The sample holder used for room temperature and low temperature measurements is made of a non-magnetic polymer material, Kel-F (poly(cholorotriflouro)ethelene). For the zero field cooled (ZFC) measurements, the sample was first cooled to the lowest possible temperature (12 K) in zero magnetic field and magnetization was recorded while warming

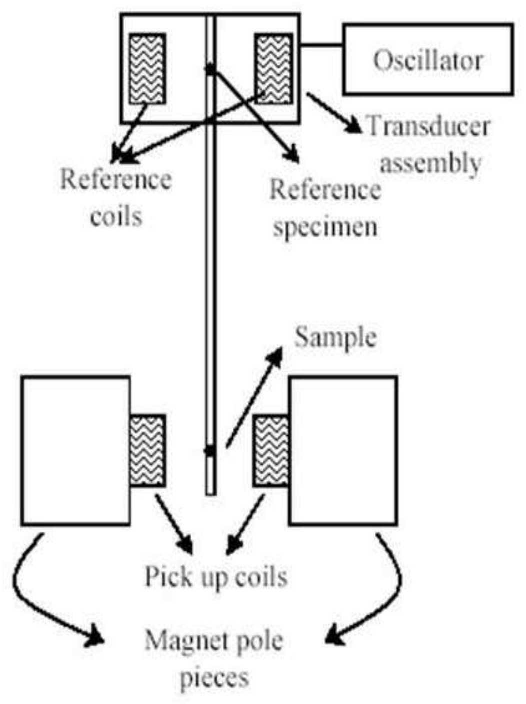

Figure 2.2: Schematic diagram of the VSM components.

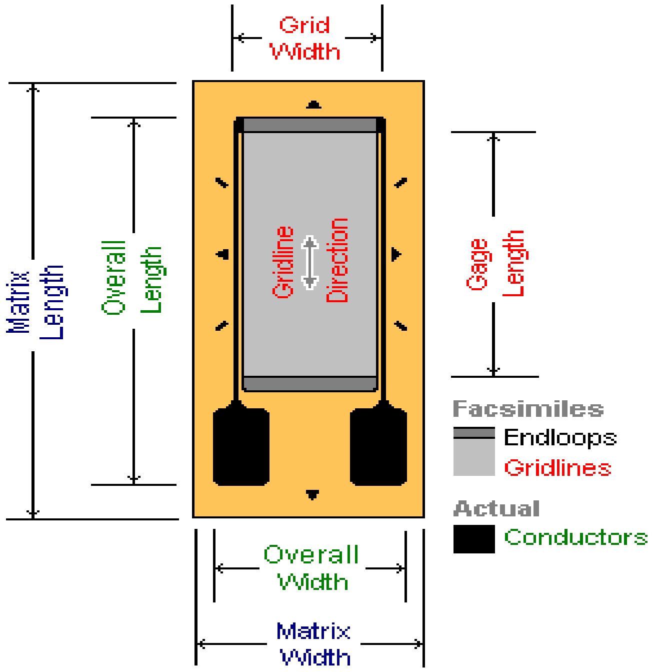

Figure 2.3: Schematic diagram of a strain gage.

the sample. In the field cooled (FC) magnetization measurements, the sample was cooled under an applied field and the magnetization was measured while heating in the same field.

Magnetostriction measurements

There are a number of methods available for the measurement of magnetostriction and continuous investigation in this field is still giving rise to new methods. Magnetostriction can be measured by direct and indirect methods such as by using strain gages, capacitance transducers and interferometers. The indirect methods are Beckner-Kersten method and the SMAR *i.e.* small angle magnetization rotation [30], with variety of techniques such as, capacitance dilatometry [31–33], direct displacement method, stress dependence of hysteresis loop [34], laser deflection method [35], etc.

The most commonly used method for the measurement of magnetostrictive strain is by uisng strain gages. This method was developed by Goldman [36]. Briss *et al.* have shown that strain gages can be successfully used for magnetostriction measurements in the temperature range -196 to 400°C [37]. A strain gage is made up of a thin resistive wire wound back and forth on a polyamide film as shown in figure 2.3. The reason for running the wire back and forth is to increase the length thereby enhancing the sensitivity without enlarging the gage unit. The change in resistance of the gage as a function of applied magnetic is recorded and converted into the magnetostrictive strain by using the relation

$$\frac{\Delta L}{L} = \frac{\Delta R/R}{G.F.} \tag{2.11}$$

where L is the initial length of the specimen, Δ L is the change in length in a magnetic field, R is the gage resistance at zero applied magnetic field, Δ R is the change in the gage resistance at a known applied magnetic field strength and G.F. is the gage factor. Usually the gage factor is provided by the manufacturer. Wheatstone bridge technique developed by Sullivan, had the advantage of minimizing the drift and noise in the magnetostriction measurements [38]. Several researchers have made use of the strain gage technique for measurements of magnetostriction of ferrites and other magnetostrictive materials. This technique has been successfully used for measurements of magnetostrictive strains in single crystals [39] as well as polycrystalline materials.

The samples used for magnetostriction measurements were pelletized into specific shapes and then sintered. The samples can be either disc shaped pellets or rods as shown in figure 2.4. In order to check for the contribution from the demagnetization factor, the magnetostriction measurements were carried out on circular rod shaped specimens with different dimensional ratios (10 mm dia × 25 mm length, 10 mm dia × 15 mm length and 13 mm dia × 5 mm thickness). The strain gage was mounted on the surface of the pellet with dimensions 13 mm × 5 mm and on the sides, after grinding the sides and making a flat surface, for the other two. The gage was mounted with special binding solutions on polished surfaces. The strain gages used in the present study were obtained from Vishay Micromeasurements, USA, (gage type EK-09-062-AP, matrix size of 6.6 mm × 4.1 mm,

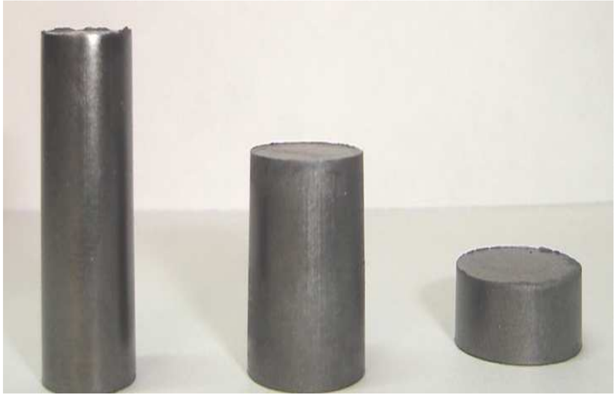

Figure 2.4: Different shapes of cobalt ferrite samples used for magnetostriction measurements.

gauge size 2.90 mm × 1.57 mm). The calibration of the strain gage was carried out by measuring the magnetostriction of Ni metal. Measurements were made on a non-magnetic ceramic dis as well as on a brass disc of size and shape similar to the sample pellets to find the contribution from the magnetoresistance of the gage and was found to be negligible up to a maximum magnetic field strength of 10 kOe. The gage resistance was measured using a wheatstone bridge arrangement as well as by using four probe resistance measurement using a Keithley 2010 multimeter. The measured magnetostriction values were found to be almost the same for different sized specimens by using the two different resistance measurement techniques. Therefore, for ease of measurements, the pellet shaped specimens were used and the size of the specimen was kept constant at 13 mm × 5 mm. Also, the multimeter technique for measuring the resistance was used for all samples.

Magnetostriction measurements were carried out on both parallel($\lambda_{\parallel}$) and perpendicular ($\lambda_{\perp}$) to the direction with respect to the applied magnetic field. The volume and anisotropic magnetostrictions were calculated using the relations $\omega = \lambda_{\parallel}$ - $\lambda_{\perp}$ and $\lambda_t = \lambda_{\parallel} + 2\lambda_{\perp}$.

References

[1] C. N. R. Rao, *Chemical Approaches to the synthesis of Inorganic Materials* (Wiley Eastern Ltd., New Delhi, 1994).

[2] O. Masala and R. Seshadri, *Annu. Rev. Mater. Res.* 34 (2004) 41.

[3] K. J. Standley, *Oxide Magnetic Materials, Monographs on the Physics and Chemistry of Materials* Ed. by W. jackson, H. Frohlion, N. F. Mott and E. C. Bullard, (Oxford University Press, London, 1962).

[4] M. M. Schieber, *Experimental Magnetochemistry: Nonmetallic Magnetic Materials* (North-Holland Publishing Company, Amsterdam, 1967).

[5] R. A. Dunlap, D. A. Small, G. R. MacKay, J. W. OBrien, J. R. Dahn and Z. H. Cheng, *Can. J. Phys.* 78 (2000) 211.

[6] A. Goldman, *Modern Ferrite Technology* (Van Nostrand Reinhold, New York, 1990).

[7] K. Suresh and K. C. Patil, *J. Solid State Chem.* 99 (1992) 12.

[8] L. A. Chick, G. D. Maupin and L. R. Pederson, *Nanostr. Mater.* 4 (1994) 603.

[9] (a) J. J. Moore and H. J. Feng, *Prog. Mater. Sci.* 39 (1995) 243. (b) J. J. Moore and H. J. Feng, *Prog. Mater. Sci.* 39 (1995) 275.

[10] T. Mimani and K. C. Patil, *Mater. Phys. Mech.* 4 (2001) 134.

[11] K. C. Patil, S. T. Aruna and T. Mimani, *Curr. pinion Solid State Mater. Sci* 6 (2002) 507.

[12] E. E. Sileo, R. Rotelo and S. E. Jacobo, *Physica* B 320 (2002) 257.

[13] A. C. F. M. Costa, E. Tortella, M. R. Morelli and R. H. G. A. Kiminami, *J. Magn. Magn. Mater.* 256 (2003) 174.

[14] J. Huang, H. Zhuang and W. Li, *J. Magn. Magn. Mater.* 256 (2003) 390.

[15] J. C. Toniolo, M. D. Lima, A. S. Takimi and C. P. Bergmann, *Mater. Res. Bull.* 40 (2005) 561.

[16] L. A. Chick, L. R. Pederson, G. D. Maupin, J. L. Bates, L. E. Thomas and G. J. Exarhos, *Mater. Lett.* 10 (1990) 6.

[17] L. R. Pederson, G. D. Maupin, W. J. Weber, D. J. McReady and R. W. Stephens, *Mater. Lett.* 10 (1990) 437.

[18] B. D. Cullity, *Elements of X-Ray Diffraction* (2nd ed. Addison-Wesley, Reading, 1978).

[19] A. R. West, *Solid State Chemistry and its Applications* (John Wiley & Sons, Singapore, 2003).

[20] M. Calligaris and S. Geremia, *Powder Diffraction Package program* (International Centre for Theoretical Physics, University of Trieste, Italy).

[21] W. Kraus and G. Nolze, *PowderCell for Windows (PCW), version 2.4* (The software is freely available from http://www.ccp14.ac.uk.)

[22] G. Thomas, *Transmission Electron Microscopy of Metals* (John Wiley & Sons, Inc, New York, 1962).

[23] D. B. Williams and C. B. Carter, *Transmission Electron Microscopy: A Textbook for Materials Science* Vol. I-IV, (Plenum Press, New York, 1996).

[24] J. Goldstein, D. Newbury, D. Joy, C. Lyman, P. Echlin, E. Lifshin, L. Sawyer and J. Michael, *Scanning Electron Microscopy and X-ray Microanalysis* 3^{rd} Ed., (Kluwer Academic/Plenum Publishers, New York, 2003).

[25] G. M. Bancroft, *Mössbauer Spectroscopy: An Introduction for Inorganic Chemists and Geochemists* (McGraw-Hill Book Company Ltd., London, 1973).

[26] *Applications of Mössbauer Spectroscopy* Vol. I, Ed. by R. L. Cohen, (Academic Press, New York, 1976).

[27] A. Bencini and D. Gatteschi, *EPR of Exchange Coupled Systems* (Springer-Verlag, Heidelberg, 1990).

[28] B. D. Cullity, *Introduction to Magnetic Materials* (Addison-Wesley Publishing Company, Massachusetts, 1972).

[29] S. Foner, *Rev. Sci. Inst.* 30 (1959) 548.

[30] K. Narita, J. Yamasaki and H. Fukunaga, *IEEE Trans. Magn.* MAG-16 (1980) 435.

[31] M. Rotter, H. Müller, E. Gratz, M. Doerr and M. Koewenhaupt, *Rev. Sci. Instr.* 69 (1998) 2742.

[32] P. T. Squire and M. R. J. Gibbs, *J. Phys. E: Sci. Instrum.* 20 (1987) 499.

[33] V. T. Cherepin, N. I. Glavatska, I. N. Glavatsky and V. G. Gaveiljuk, *Meas. sci. Technol.* 13 (2002) 174.

[34] R. Becker and M. Kersten, *Z. Phys.* 64 (1930) 660.

[35] Q. Y. Yan, R. J. Gambino, S. Sampath and Q. Huang, *J. Appl. Phys.* 97 (2005) 033902

[36] J. E. Goldman, *Phys. Rev.* 72 (1947) 529.

[37] R. R. Briss and E. W. Lee, *J. Sci. Instrum* 37 (1960) 225.

[38] M. sullivan, *Rev. Sci. Inst.* 51 (1980) 382.

[39] R. M. Bozorth and R. W. Hamming, *Phys. Rev.* 89 (1953) 865.

PART-I

Chapter 3

Magnetostriction Studies on $CoFe_2O_4$

3.1 Introduction

The magnetic and electrical properties of ferrites are sensitive to the changes in their chemical composition as well as microstructure, which are greatly influenced by the manufacturing process [1, 2]. For example, controlling the grain size has a larger impact on the magnetic permeability and power loss in the case of Mn-Zn and Ni-Zn ferrites [2]. Different processing parameters such as use of external additives during sintering, heating rate, cooling rate, sintering time and sintering atmosphere, affect the performance of these materials [3]. It is known that the sintering behavior of the ferrite is considerable affected by the particle size of the starting powders. The particle size in the starting powders can be reduced to sub-micron or nanosized levels by using ball milling technique [4, 5] or by employing different low temperature methods of syntheses [6, 7]. The sintering behavior of powders containing sub-micron or nanoparticles is different as compared to their bulk counterparts. Nanosized ferrite particles have more sinterability due to their fine particle nature as well as the high surface to volume ratio [8, 9]. The sintered products derived from nanocrystalline ferrite powders exhibit improved magnetic permeability which depends on the microstructure, density, porosity, grain size, etc., as compared to the materials sintered from the bulk counterparts [2, 8, 10].

Magnetostriction studies on ferrimagnetic spinels have been initiated in the 1950s

[11–16]. Domenicali has studied the magnetostriction of magnetite in order to study the crystallographic transitions at low temperature [11]. Bickford *et al.* have analyzed the magnetostriction behavior of magnetite and cobalt substituted magnetite [14], and showed that polycrystalline cobalt containing magnetite exhibits very high strains. The magnetostriction constants of single crystals of MFe_2O_4, where M stands for Mn, Fe, Co, Ni, and Zn in various proportions, have been determined by Bozorth using the method of strain gages [15]. These studies were mainly oriented towards understanding the effect of material anisotropy, crystal symmetry, and magnetic annealing on the magnetostriction constants of spinel ferrites.

Amongst the spinel ferrites, cobalt ferrite shows very high value of magnetostrictive strain [17]. There is a recent interest in the studies of cobalt ferrite based magnetostrictive materials mainly because of the possibility of using these materials for stress sensing applications. Though the magnetostrictive properties of bulk cobalt ferrite prepared by the conventional method has been studied in detail, there is a need to understand the effect of different processing parameters such as the processing conditions, microstructure, sintering aids on the magnetostrictive behavior of cobalt ferrite. In all the reported work on the magnetostriction studies on polycrystalline cobalt ferrite, the material is sintered at a high temperature of 1400 °C and above and there is no information available on the relationship between sintering conditions, microstructure and magnetostriction. Also, there are no systematic studies performed to understand the effect of sintering temperature on the magnetostrictive properties of cobalt ferrite.

The current research interest in nanosized cobalt ferrite based materials is mainly due to the potential applications in high-density information storage and magneto-optical devices, because of their strong anisotropy, high saturation magnetization and coercivity [18, 19]. Apart from the conventional ceramic method of synthesis and ball milling process [20–22] which give sub-micron sized particles, cobalt ferrite can be prepared by a variety of low temperature wet chemical methods, such as coprecipitation [23–25], sol-gel [26–28], micro-emulsion [29–31], oxalic acid precursor [32], urea as precursor [33], combustion synthesis [34, 35], complexometric synthesis [36], hydrothermal synthesis [37, 38], redox process [39], and many more as reported in the literature [40–42]. However, the magnetostriction behavior of cobalt ferrite sintered using powders synthesized in the nanocrystalline form has not been studied so far. It is expected that such studies will help in optimizing the processing parameters for developing magnetostrictive materials based on cobalt ferrite.

The objective of this work is to understand the effect of processing conditions on the magnetic and magnetostrictive behavior of cobalt ferrite.

3.2 Preliminary Studies on $Co_xFe_{3-x}O_4$

Previous studies on polycrystalline samples of cobalt ferrite $Co_xFe_{3-x}O_4$ for $x < 1$ have shown that maximum magnetostriction decreases with decreasing Co content. A maximum magnetostriction value of 110 ppm is reported for compositions close to $x = 1$ in the series [13]. In the present work, different compositions are prepared with higher Co content in order to understand the effect of Co on the magnetostriction in the series $Co_xFe_{3-x}O_4$ and identify the compositions exhibiting maximum value of magnetostriction. These studies are performed to select the compositions for further detailed studies. The compositions in the series $Co_xFe_{3-x}O_4$ ($x = 0.8$, 1.0, 1.1, 1.2 and 1.3) were synthesized by the conventional ceramic method of synthesis. The synthesis was carried out on a small scale (15 gm batch) using iron oxide and cobalt carbonate as starting materials. These starting materials were mixed together in an agate mortar using acetone as a mixing medium. The mixture was initially calcined at 1000 °C for 12 h and further heat treatments were carried out at 1000 °C for 12 h and 1100 °C for 48 h with intermediate grinding after 24 h.

3.2.1 Powder XRD Analysis

The phase purity of the different compositions was analyzed using powder X-ray diffraction. Figure 3.1 shows the XRD patterns of the compositions with $x = 1.0$. 1.1 and 1.2. The XRD patterns of the samples are compared with the simulated pattern $CoFe_2O_4$ in the figure. All the samples show the formation of spinel type phase confirming the formation of the desired compositions. The cubic lattice parameter is found to slightly decrease with increasing cobalt concentration. Similar decrease in the lattice parameter has been reported for different compositions in the $Co_xFe_{3-x}O_4$ series synthesized by the conventional ceramic and low-temperature methods [43, 44].

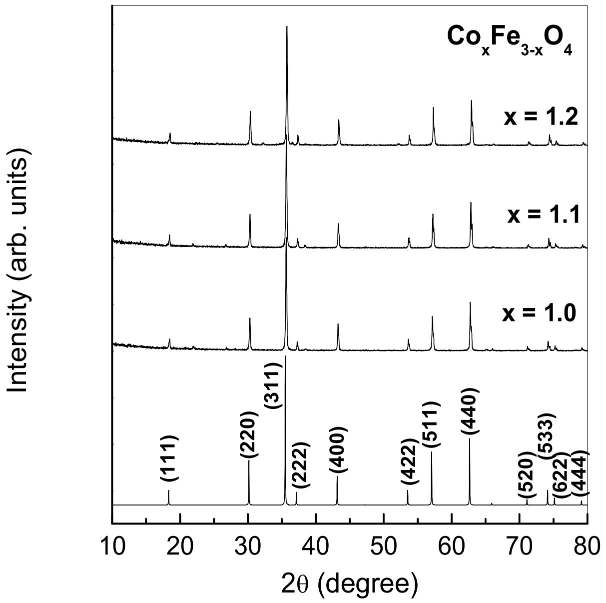

Figure 3.1: Powder X-ray diffraction patterns for the samples in the Co$_x$Fe$_{3-x}$O$_4$ series. The simulated pattern is shown and indexed for comparison.

3.2.2 TMA Analysis

The sintering behavior of the compacted powders is studied using a thermal mechanical analyzer. The samples were used in the form of thin discs and heated at a constant heating rate of 10 °C/min up to a maximum temperature of 1350 °C. The sintering curves of three different compositions are compared in Figure 3.2. All three compositions show almost identical sintering behavior. As can be seen from the figure, effective sintering starts above 1000 °C and sintering is not completed even at the maximum studied temperature of 1350 °C. Hence the final powders were pressed in to the form of disc shaped pellets and sintered at 1100 °C for 8 h for microstructure and magnetostriction measurements. The densities of the sintered pellets were measured and were found to be close to 85% of the X-ray density of the corresponding compositions. The SEM photograph of CoFe$_2$O$_4$ sintered at 1100 °C shown in figure 3.5 suggests a very porous microstructure with very small grains. It is obvious that the material is not sintered properly after sintering at 1100 °C for 8 h.

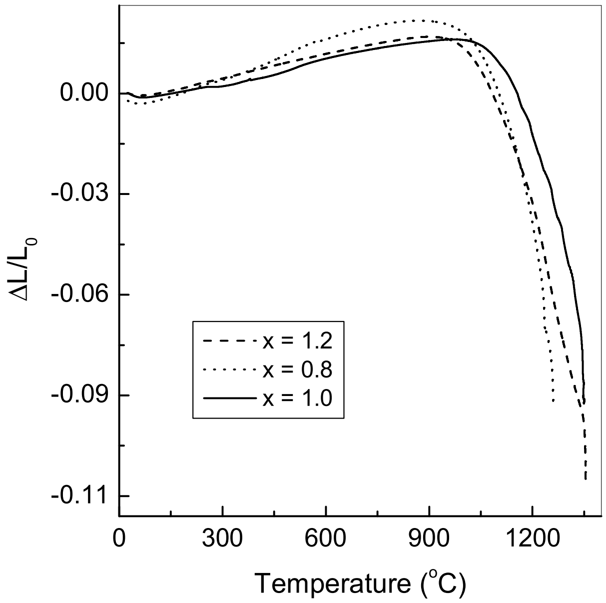

Figure 3.2: Sintering behavior for the samples in the $Co_xFe_{3-x}O_4$ series.

3.2.3 Magnetic Measurements

The field dependence of magnetization up to a maximum magnetic field of 15 kOe, measured at room temperature, is shown in figure 3.3. Maximum magnetization at 15 kOe is observed for the composition with $x = 1.0$ and is about 84 emu/g which is found to be in agreement with the values reported of bulk cobalt ferrite at room temparture [45]. With increasing cobalt concentration, the saturation magnetization is decreased. The decrease in the saturation magnetization is expected because of the lower magnetic moment of Co^{2+} (3 μ_B) as compared to that of Fe^{3+} (5 μ_B). Similarly, the coercivity is found to increase with increasing cobalt concentration, indicating increase in the anisotropy of these compositions which can be attributed to the presence more number of Co^{2+} ions.

3.2.4 Magnetostriction Studies

The magnetostriction curves of the different compositions recorded up to a maximum magnetic field strength of 6.0 kOe are shown in figure 3.4. The measurements were performed in the direction of the applied magnetic field ($\lambda_{\parallel}$) and the values are negative. Small and positive values were obtained when measured in the perpendicular direction

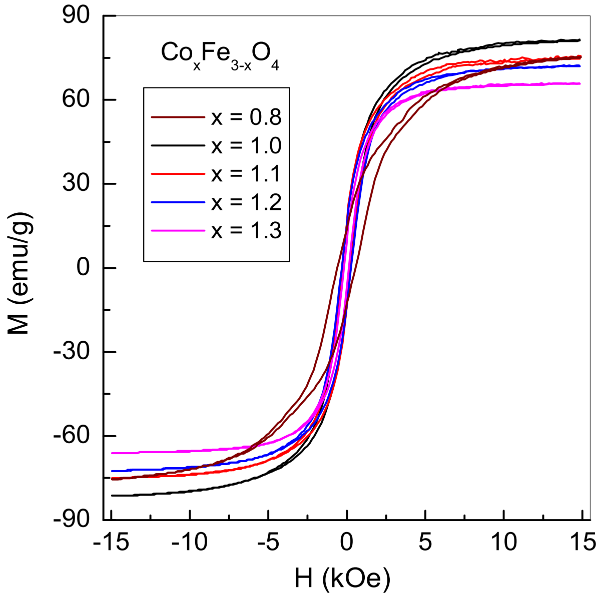

Figure 3.3: Room temperature magnetization curves for the samples in the $Co_xFe_{3-x}O_4$ series.

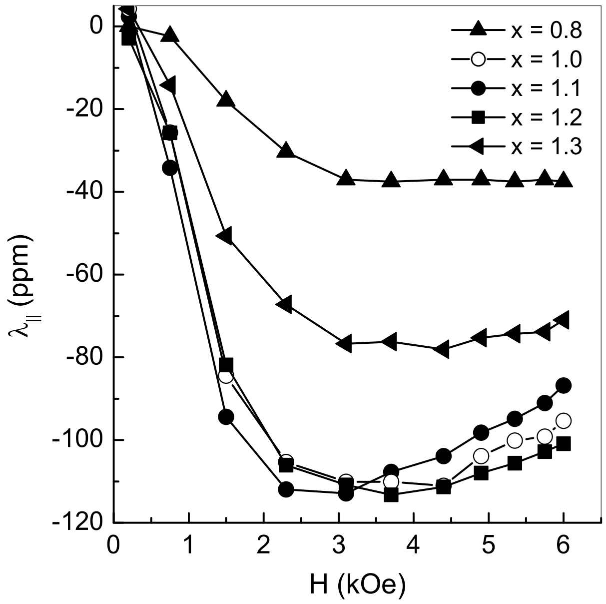

Figure 3.4: Magnetostriction measured in the direction parallel to the applied field for different compositions in the $Co_xFe_{3-x}O_4$ series.

($\lambda_\perp$). As can be seen from the figure, maximum value of magnetostriction is obtained when $1.0 \leq x \leq 1.2$. Maximum strain of ~110 ppm is observed for the compositions with $1.0 \leq x \leq 1.2$. The smaller values of magnetostriction observed here as compared to the recent reports on $CoFe_2O_4$ (225 ppm) [46, 47] may be due to the difference in the processing conditions of these compositions. In the present case the powders are sintered at 1100 °C for 8 h and are found to be much more porous. Similarly the TMA analysis also revealed that higher sintering temperatures are required in order to have a material with sufficiently large compact density. Cobalt ferrite is sintered at a very high temperature of around 1450 °C in the recent reports [46, 47]. Therefore, for further magnetostriction studies the samples were sintered at 1450 °C.

3.3 Studies on $CoFe_2O_4$

The preliminary studies showed that maximum magnetostrictive strains are observed for $1.0 \leq x \leq 1.2$ in the $Co_xFe_{3-x}O_4$ series. Since the initial studies indicated that higher sintering temperatures might be required to properly sinter the samples, the composition with $x = 1.0$ is sintered at a higher temperature of 1450 °C, for 10 minutes, as reported by McCallum *et al.* [46]. The magnetic and magnetostrictive properties of this composition are further studied in detail.

3.3.1 Microstructural Analysis

The SEM photographs of $CoFe_2O_4$ sintered at 1100 °C for 8 h, used in the initial studies, and the one sintered at 1450 °C for 10 minutes are compared in figure 3.5. Micrograph (A) shows the compact sintered at 1100 °C and micrograph (B) shows the one sintered at 1450 °C. As can be clearly seen from these photographs, the material sintered at 1450 °C shows a comparatively dense microstructure as compared to the compact sintered at 1100 °C for 8 h. Micrograph (A) shows a very porous microstructure and no grain growth is observed. Sintered density close to 90% of the theoretical density is obtained after sintering at 1450 °C where as it was only 85% for the material sintered at 1100 °C. A very recent report on the sintering studies on cobalt ferrite indicated that temperatures higher than 1400 °C are required for proper sintering of cobalt ferrite [22].

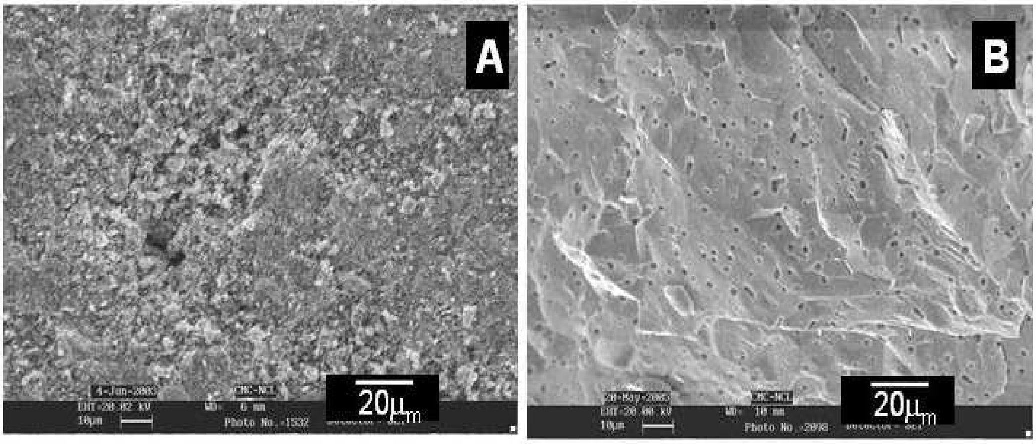

Figure 3.5: Comparison of the SEM photographs for the composition $CoFe_2O_4$ sintered at 1100 °C for 8 hours (A) and 1450 °C for 10 minutes (B).

3.3.2 Magnetic Measurements

The field dependence of magnetization, recorded at room temperature, for the powder and the sample sintered at 1450 °C are shown in figure 3.6. The sintered sample shows a slightly enhanced magnetization as compared to the powder sample and a smaller coercive field. The inset of the figure shows the temperature dependence of magnetization recorded in a magnetic field strength of 50 Oe for the sintered sample. The Curie temperature is obtained as 520 °C which is in agreement with the value reported in the literature for cobalt ferrite [48].

3.3.3 Magnetostriction Studies

The room temperature magnetostriction curve of the $CoFe_2O_4$ sample sintered at 1450 °C is shown in figure 3.7. The measurement is carried out up to a maximum magnetic field strength of 10 kOe at room temperature. Measurements were made in the parallel ($\lambda_{\|}$) as well as the perpendicular ($\lambda_{\perp}$) directions with respect to the applied magnetic field. As can be seen from the figure, magnetostriction in the parallel direction ($\lambda_{\|}$) is improved to a maximum value of $\sim$140 ppm as compared to the value of 113 ppm observed for the sample sintered at 1100 for 8 h in the initial studies on $CoFe_2O_4$. Therefore, for further

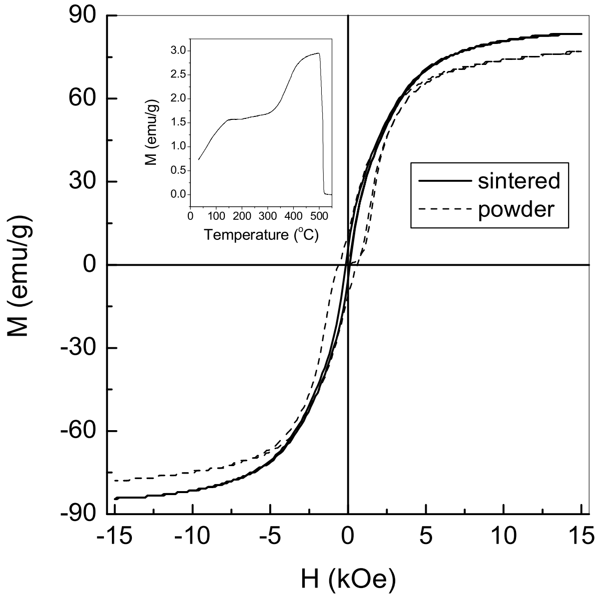

Figure 3.6: Field dependence of magnetization for the powder and sintered cobalt ferrite. The inset shows the M-T curve recorded for the sintered sample.

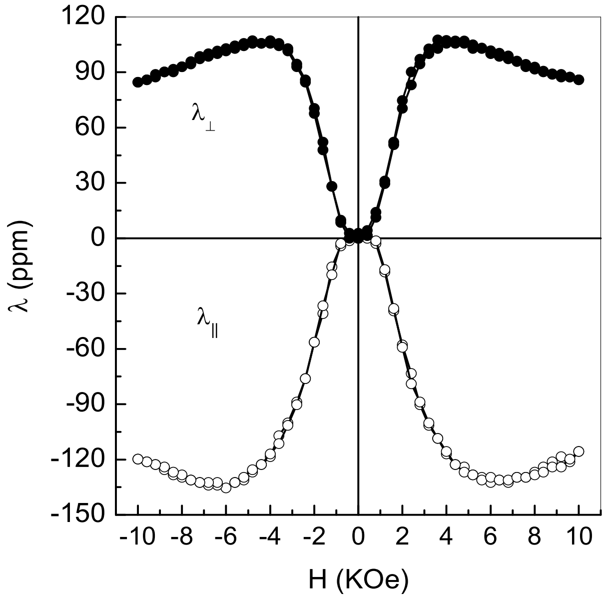

Figure 3.7: Magnetostriction curves of $CoFe_2O_4$ sintered at 1450 °C for 10 minutes, measured in the parallel and perpendicular directions.

studies on nanosized cobalt ferrite, the sintering temperature was kept the same as 1450 °C.

3.4 Studies on Nanosized $CoFe_2O_4$

The magnetic properties of ferrites change drastically when synthesized in the nanocrystalline form when compared to their bulk counterparts. Also, the sintering behavior of the nanosized powder particles is expected to be different when compared to the bulk materials. As has been mentioned in the introduction of this chapter, cobalt ferrite can be synthesized in the nanosized form by many different methods. As discussed, sintered products from nanocrystalline powders are known to show improved permeability and loss factor. However, not much efforts have been made to understand the effect of particle size of the starting powder on the magnetostrictive properties of the ferrites. To compare the magnetic and magnetostrictive behavior of sintered cobalt ferrite derived from nanocrystalline powders, the powders are synthesized by three different low-temperature routes. The results are then compared with the sintered material derived from the powders synthesized by the conventional ceramic method.

3.4.1 Synthesis

The synthesis methods employed for obtaining the nanoparticles are described below. The synthesis was carried out using three different low temperature methods of synthesis *i.e.* the coprecipitation method (CPP), citrate precursor route (CIT), and the glycine nitrate combustion route (GNP). The experimental procedures used for the synthesis are as follows. For the synthesis of cobalt ferrite by the different methods, all the required chemicals used were of AR grade.

Autocombustion Method

The autocombustion process of synthesizing metal oxides using the corresponding metal nitrates as the oxidizer and glycine as the fuel, known as the glycine-nitrate process (GNP) [49], is used here. For the synthesis of cobalt ferrite, stoichiometric quantities of the corresponding metal nitrates $Fe(NO_3)_3.9H_2O$ and $Co(NO_3)_2.6H_2O$ were individually dissolved in minimum amount of distilled water. The metal to glycine ratio is maintained as 1:2, as reported [49]. The solutions of the respective metal nitrates and glycine were mixed together in a large crystallizing dish. The final mixed solution (in the crystallizing dish) was kept over a hot plate for evaporation and autocombustion, at a temperature of ~200 °C. A viscous gel formed at the bottom of the dish after the complete evaporation of water subsequently underwent autocombustion producing a fluffy mass within few seconds (as-synthesized product). The obtained powder was then used for different measurements.

Citrate Precursor Method

For the synthesis using the citrate precursor method (CIT), stoichiometric amounts of cobalt nitrate and ferric nitrate were dissolved in distilled water. Water solution of citric acid was added to the metal ion solution keeping the metal to citric acid ratio as 1:2 [50] The solution was evaporated on a water bath and finally a thick gel was formed. This precursor was dried overnight in an oven at 100 °C and the dried precursor was calcined at 500 °C for 4 hours to get the cobalt ferrite powder.

Coprecipitation Method

In the coprecipitation method (CPP), cobalt and iron nitrates were taken in the stoichiometric ratio and dissolved in distilled water and mixed together. 20% KOH solution was added drop wise to this solution under constant magnetic stirring. A precipitate formed was filtered and washed several times with distilled water until the pH of the filtrate was ~7. The precipitate was dried overnight in an oven at 100 °C which eventually converted to a black powder.

3.4.2 Powder XRD Analysis

The Powder XRD patterns for the samples synthesized by the three different methods are shown in figure 3.8. The XRD pattern for the sample synthesized by the standard ceramic route is also shown for comparison. All the reflections in the XRD patterns correspond to that of cobalt ferrite and no additional reflections are observed for the samples indicating the phase purity of the samples. The reflections of the samples synthesized by the citrate and coprecipitation methods are very broad and that of the sample synthesized by the

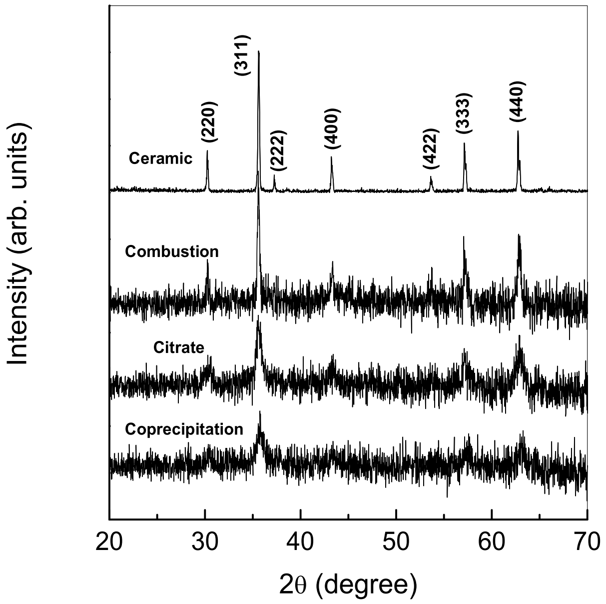

Figure 3.8: X-ray diffraction patterns of the samples synthesized by the low-temperature routes along with the one synthesized by the ceramic process.

combustion method are broader than that of the the sample prepared by the ceramic route, indicating the presence of smaller crystallites in the low-temperature synthesized powders.

The average crystallite size is calculated using the Scherrer formula. The crystallite sizes calculated are 12, 15 and 45 nm for the samples synthesized by coprecipitation, citrate and combustion methods, respectively. Kikukawa *et al.* also reported comparable crystallite size for cobalt ferrite particles synthesized by the GNP method for a glycine:natrate ratio closer to 0.5 [35]. The larger crystallite size observed for the combustion synthesized sample is likely to be due to the very high flame temperature, which may lead to growth of the particles during the combustion process. Temperatures as high as 1500 °C may be reached during the combustion process involving glycine as a fuel [49].

3.4.3 TMA Analysis

The sintering curves of the samples prepared by the different low-temperature methods are shown in figure 3.9. The sintering process of the compacts derived from nanocrystalline powders is expected to be different from that derived from the micron sized particles

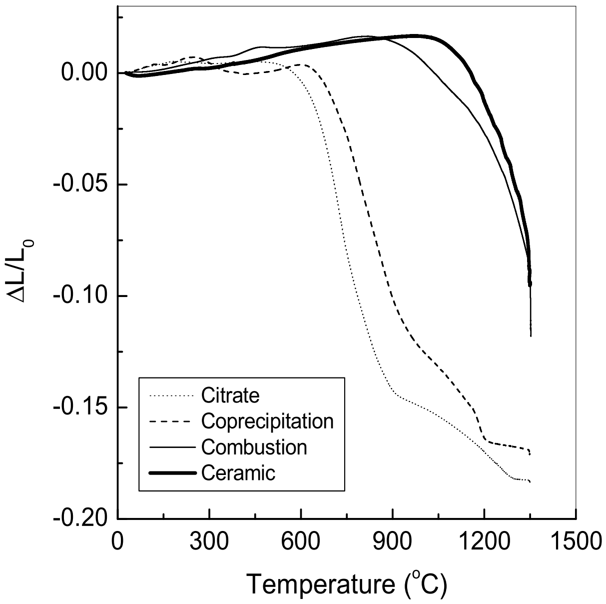

Figure 3.9: Sintering behavior of cobalt ferrite prepared by different methods.

derived by the ceramic method because of the high surface energy and larger surface area associated with the nanoparticles [51, 52]. Hsu *et al.* reported that the samples of NiCuZn ferrite synthesized by chemical coprecipitation method can be sintered at a relatively low temperature of around 800 °C [51]. Yue *et al.* have studied the sintering behavior of MgZnCu ferrite prepared via sol-gel combustion process and found that the ferrite material can be sintered at a relatively low temperature of 950 °C [52]. As is evident from figure 3.9, the sintering behaviors of the samples synthesized by the coprecipitation (CPP) and citrate (CIT) methods are some what different from the ones synthesized by combustion and ceramic methods. The sintering process in the case of CPP and CIT samples starts at 700 °C and effective sintering takes place above 1300 °C. For the combustion synthesized sample, the sintering behavior is almost identical with that of the bulk sample. Although the crystallite size calculated from the XRD data is 45 nm for this sample (also TEM studies showed the presence of nanometer sized particles, see figure 3.11) the sintering behavior is not that expected. This unexpected behavior can be explained based on the synthesis conditions. During the combustion process the local temperatures can be very high. According to Chick *et al.*, the internal temperatures during the combustion process can reach as high as 1500 °C depending upon the molar ratio of nitrates and glycine used [49]. In the present case 2 moles of glycine is used per mole of metal ions. The ratio is close to a glycine/nitrate ratio of 0.5 in which case the flame temperature will be very high. This high temperature generated during a short time makes the particles more sintered and hence the surface of the particles become non-active, as in the case of the ceramic samples, although the particle sizes are smaller. Similar sintering characteristics have been reported for oxide ceramics synthesized by the combustion technique using other fuels such as urea [53] or glycine as in the present case and ceramic samples. For example, Shi *et al.* have shown that the difference between the sintering temperature for combustion and ceramic samples is only 60 °C, though the particle size of the combustion synthesized sample is much less than that of the sample synthesized by using the ceramic method [54].

Since the sintering studies showed that the samples are not completely sintered up to a maximum studied temperature of 1350 °C (see figure 3.9), for comparison of the properties of the sintered samples, all the four samples were sintered under identical conditions at a temperature of 1450 °C for 10 minutes. The densities of these sintered pellets are measured by measuring the volume and weight of these disks.

3.4.4 SEM and TEM Analysis

The morphology and particle size of the powders synthesized by the three low temperature methods are studied using SEM and TEM. For the ceramic sample, particle size is obtained from the scanning electron micrograph. The SEM photographs of the samples are shown in figure 3.10. As can be seen from the figure, the powder synthesized by the combustion method is highly porous. This can be attributed to the generation of large volume of gases during the combustion reaction which occurs in a very short time [49, 55]. The ceramic sample shows the presence of micron sized particles, whereas the powders prepared by the citrate and coprecipitation methods show the presence of very large lumps and they are found to be agglomerates of small spherical particles.

Since the exact particle size determination was not possible from the scanning electron micrographs, the TEM images are obtained for the low-temperature synthesized samples. Figure 3.11 shows the transmission electron micrographs for the low-temperature synthe-

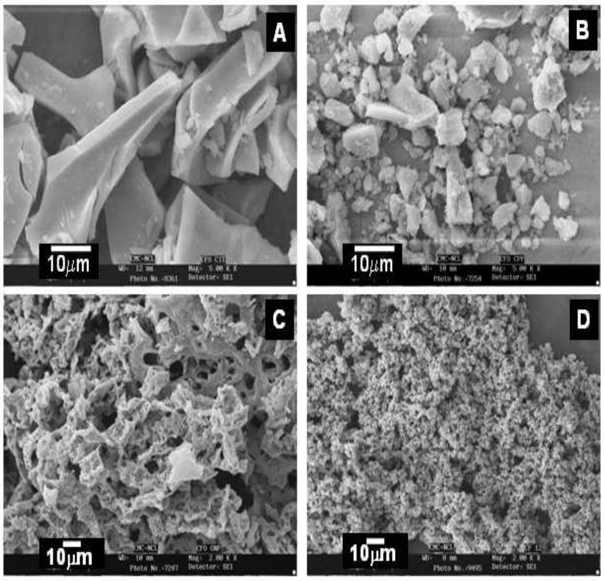

Figure 3.10: SEM photographs of the powders prepared by (A) citrate method, (B) coprecipitation method, (C) combustion method and (D) ceramic method.

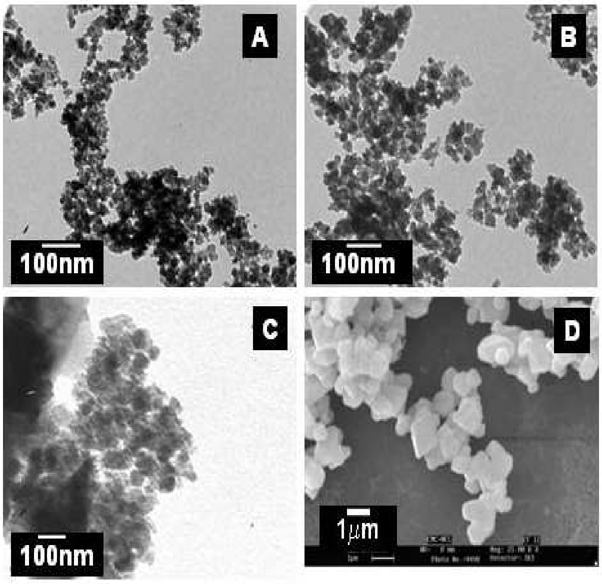

Figure 3.11: Transmission electron micrographs of cobalt ferrite prepared by (A) citrate, (B) coprecipitation and (C) combustion methods and (D) SEM photograph of the powder synthesized by the ceramic method.

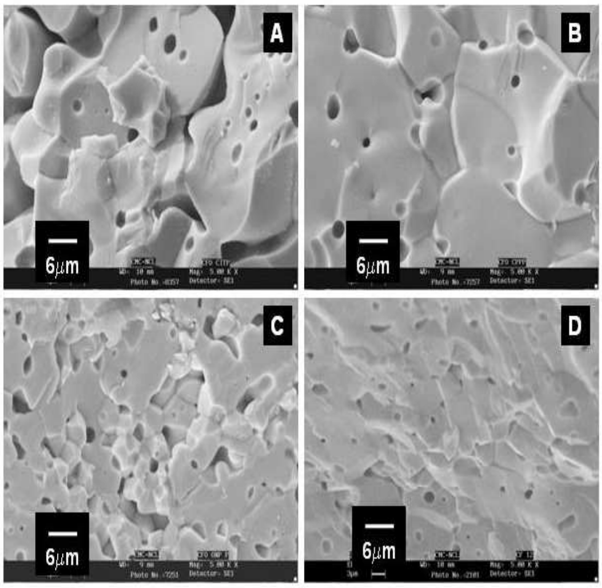

Figure 3.12: SEM photographs of the sintered samples synthesized by (A) citrate, (B) coprecipitation, (C) combustion, and (D) ceramic methods.

sized samples along with the SEM photograph of the ceramic sample for comparison. The TEM images reveal the nanoparticle nature of all the low-temperature synthesized samples. The particles synthesized by the coprecipitation method are highly agglomerated. The individual particles are of average size of 10 nm. The particles synthesized by the citrate method have average particle size of around 15 nm. The combustion synthesized samples show very large agglomerates of particles having sizes above 30 nm. These particle sizes are comparable to the average crystallite sizes calculated from the XRD patterns. The average particle size of the sample prepared by the ceramic method is found to be 0.9 μ_m.

The SEM microstructures of the sintered products obtained from the corresponding powders are shown in figure 3.12. The SEM images show that there are differences in the microstructures of the sintered samples. The micrograph C of the combustion synthesized sample shows the presence of smaller grains whereas the micrograph D of the ceramic sample looks like a part of bigger grain, in which no clear grains are visible. For the samples prepared by coprecipitation and citrate methods, clear grains with different sizes are visible. The grains in the sample prepared by the citrate precursor method are found

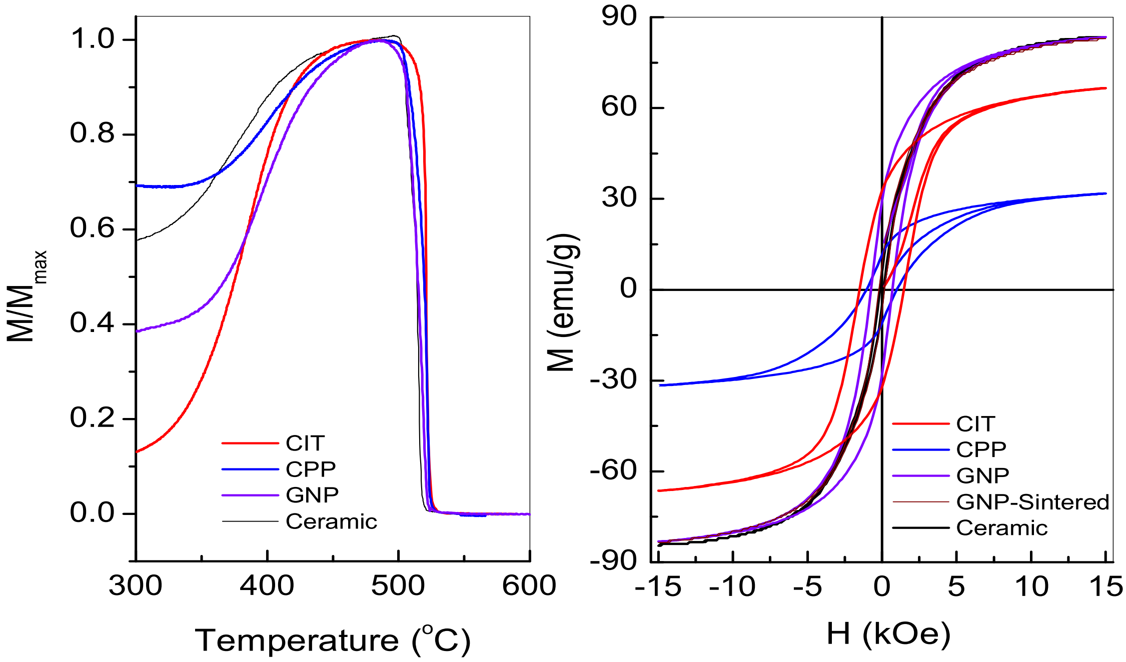

Figure 3.13: Variation of magnetization as a function of temperature (left) and magnetic field at room temperature, for the samples synthesized by the low-temperature and ceramic routes.

to be slightly bigger than that in the sample synthesized using the combustion method and smaller than those prepared by the coprecipitation method.

3.4.5 Magnetic Measurements

The temperature dependence of magnetization recorded in an applied magnetic field of 50 Oe and the field dependence of magnetization recorded at room temperature for all the samples are shown in figure 3.13. The saturation magnetization at 15 kOe and the coercivity of the samples are compared in Table 3.1. All the samples prepared by the different synthesis routes show almost identical Curie temperature, comparable to the value reported for cobalt ferrite ∼ 520°C [48]. The magnetization at 15 kOe for the sample synthesized by the combustion method is found to be ∼80 emu/gm which is almost comparable to the value for cobalt ferrite synthesized by glycine-nitrate process as reported by Kikukawa *et al.* [35]. It is observed that the saturation magnetization of

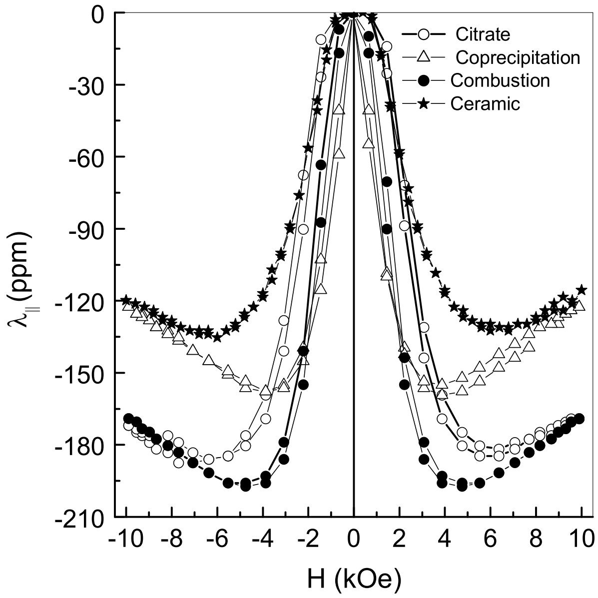

Figure 3.14: Magnetostriction as a function of magnetic field recorded in the parallel direction to the applied magnetic field.

the powder sample synthesized by the combustion method is almost identical to that of the sintered products. The coercivity and saturation magnetization of the ceramic and combustion samples are almost comparable. However, the samples synthesized by citrate and coprecipitation methods show a reduced value of magnetization of 66.7 and 31.9 emu/gm, respectively. The higher value of magnetization for the combustion synthesized sample is due to the larger particle size of this sample.

3.4.6 Magnetostriction Studies

Magnetostriction is measured at room temperature up to a maximum magnetic field strength of 10 kOe in both parallel as well as the perpendicular directions to the applied magnetic field. The magnetostriction curves recorded for cobalt ferrite prepared via different synthesis routes in the parallel and perpendicular directions to the applied magnetic field are shown in figure 3.14 and figure 3.15, respectively. The highest magnetostriction is obtained for the sample synthesized by the autocombustion method and the lowest value is obtained for the sample synthesized by the ceramic method. Cobalt ferrite prepared by the combustion method shows an enhanced magnetostriction of 197

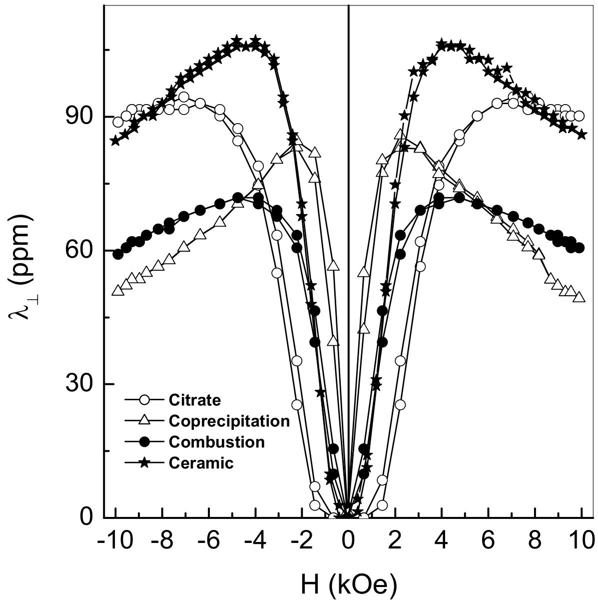

Figure 3.15: Magnetostriction as a function of magnetic field recorded in the perpendicular direction to the applied magnetic field.

ppm. In fact all the samples prepared by the low temperature methods show higher values of magnetostriction as compared to the sample prepared by the conventional ceramic method. The magnitudes of the magnetostrictive strains are 197, 184, 159 and 134 ppm for the cobalt ferrite samples prepared by combustion, citrate, coprecipitation and ceramic methods, respectively. Apart from the difference in the maximum magnetostriction, the magnetic field required to achieve the maximum value of the magnetostriction (H_{max}), and the magnetostriction at low magnetic field strengths are also found to be different. The magnetic field required to achieve the maximum strain is 4.7, 5.5, 3.8 and 6.8 kOe for the samples synthesized by combustion, citrate, coprecipitation and ceramic methods, respectively.

The magnetostriction curves recorded in the perpendicular direction ($\lambda_\perp$) also show some different behavior. The magnitude of maximum magnetostriction are 71, 94, 85 and 105 ppm for the samples prepared by combustion, citrate, coprecipitation and ceramic methods, respectively. The field required to achieve these maximum magnetostrictive strains are also found to be different for all the samples. Though the ceramic sample shows higher strain in the perpendicular direction amongst all the samples, a magnetic field of

Table 3.1: Summary of particle size from XRD (d_{XRD}) and TEM (d_{TEM}), H_c, M_s, Percentage sintered density (D), grain size (G) and magnitude of maximin magnetostriction $\lambda_{\|}$, for the samples synthesized by coprecipitation (CPP), citrate (CIT), combustion (GNP) and ceramic (CER) methods.

Synthesis Method	Powder samples				Sintered samples				
	d_{XRD} (± 1nm)	d_{TEM} (nm)	M_s (emu/g)	H_c (Oe)	D (%)	G μm	M_s (emu/g)	H_c (Oe)	$\lambda_{\|}$ (ppm)
CPP	12	10	31.9	1022	92	23	80.0	158	159
CIT	15	18	66.7	1490	77	17	81.4	241	184
GNP	45	35	83.5	710	84	8	83.5	206	197
CER	–	900*	77.0	600	96	> 25	83.7	135	134

* from SEM

4 kOe is required to achieve this value. However, relatively lower magnetic fields of 2.2 and 3.8 kOe are required for the coprecipitation and the combustion synthesized samples, respectively. The coercivity, magnetization, grain size form SEM and the magnetostrictive strain observed in the parallel direction are compared in Table 3.1.

A comparison of the different parameters listed in Table 3.1 indicates that there is no correlation between the magnetostriction and any other parameters, except for the grain size of the sintered materials. Guillaud has earlier shown that for $Co_{0.76}Fe_{2.24}O_4$, magnetostriction is independent of density and coercivity [13]. A close comparison of the magnitude of the observed magnetostrictive strains with the microstructures of the sintered pellets shows that there is some sort of dependence of magnetostriction on the microstructure. The sample having the smallest grains show the maximum magnetostriction, and the magnetostriction decreases with increasing grain size. For example, the sample synthesized by the autocombustion method has a grain size of 8 μ_m and it shows the highest value of magnetostriction of 197 ppm, and the ceramic sample having a grain size larger than 25 μ_m exhibits the lowest magnetostriction of 135 ppm. The samples prepared by the citrate and coprecipitation methods have the grain size of 17 and 23 μ_m and show magnetostriction of 184 and 159 ppm, respectively, thus supporting the dependance of magnetostriction on the grain size. These results indicate that controlling the microstructure is one of the ways to control the magnetostrictive properties of cobalt ferrite and in order to achieve higher values of magnetostrictive strains the presence of smaller and uniform sized grains in the sintered product will be helpful.

3.5 Studies on Ball Milled $CoFe_2O_4$

The magnetostriction studies performed on sintered cobalt ferrite derived from nanosized powders showed a strong dependence of magnetostrictive strain on the microstructure of the sintered compact. These results suggest the need to understand the effects of processing conditions which can control the microstructure of sintered cobalt ferrite. Although the strain obtained for the sample derived by the combustion method is as high as 200 ppm, the preparation of the nanosized ferrite powders on a larger scale is comparatively difficult by this method as compared to the reduction of size by the ball milling process. Ball milling can lead to reduction in the particle size of the materials. Ball milling process is a very simple technique for the preparation of ultra-fine ferrite particles in large quantities on an industrial scale [56]. Therefore, cobalt ferrite synthesized by the ceramic process in larger quantities is ball milled to reduce the particle size. The effect of different parameters such as sintering temperature, dwell time and sintering aids is studied on the magnetostrictive behavior of the sintered products derived from the ball milled powders. It was expected that this will help in optimizing the processing parameters for developing magnetostrictive materials based on cobalt ferrite.

3.5.1 Synthesis

$CoFe_2O_4$ was synthesized by the conventional ceramic method. Stoichiometric amounts of $CoCO_3$ and Fe_2O_3 were mixed in a ball mill for 24 h. The resulting mixture was calcined at 1000 °C for 12 h and further heated at the same temperature after an intermediate grinding. This was followed by heating the powder at 1100 °C for 72 h with three intermediate grindings. The final powder obtained was balled milled for 8 h in order to further reduce the particle size. Ball milling was performed using stainless steel balls in a plastic container with distilled water as milling medium. The milled powder was sieved first through a 100 mesh and then through a 200 mesh. The sintering behavior was analyzed using a Thermal Mechanical Analyzer (TMA), in the temperature range of 30 °C to 1350

°C. Disc shaped pellets were made from the ball milled powder by cold uniaxial pressing in a stainless steel die and the pellets were then sintered at four different temperatures (1100, 1200, 1300 and 1400 °C for different dwell times of 4 h, 8 h, 16 h and 24 h. The furnace was heated to the required temperature at the rate of 4 °C/min and was cooled back to room temperature at the same rate after sintering for different dwell times. Densities of the sintered discs were calculated from the volume (calculated from the measured diameter and thickness of the discs using a vernier calipers) and the weight of the discs as well as by the Archimedes method. These two methods gave comparable values of the densities. To study the effect of sintering aids on the microstructure and magnetostriction, pellets were sintered by adding 1% of sintering aids like TiO_2, Y_2O_3 and Nb_2O_5 to the ball milled cobalt ferrite powder. The powder as well as the sintered materials were analyzed for their magnetic, magnetostrictive and microstructural features.

3.5.2 Powder XRD Analysis

The powder XRD pattern of the ball milled cobalt ferrite powder is shown in figure 3.16. All the reflections correspond to the spinel structure which confirmed the phase purity of the sample. The lattice constant is obtained by refining the XRD pattern as 8.382 Å, which is in agreement with the value reported for bulk cobalt ferrite (8.38 Å) [48].

3.5.3 TMA Analysis

Figure 3.17 shows the sintering behavior of the ball milled powder. The sintering curve for the powder with out ball milling is also shown for comparison. As can be seen from the figure, the sintering behavior of the balled milled sample shows a different behavior as compared to the one without ball milling. For the ball milled powder, effective sintering starts at a lower temperature of of 950 °C and continuous linear shrinkage is observed above 1050 °C. The sintering is not complete till the maximum temperature of 1350 °C. Nearly 12% shrinkage is observed till this maximum temperature. Such an incomplete sintering behavior can be due to the larger particles of cobalt ferrite used in the present study. The percentage shrinkage observed for the sample is comparable to the recent report by Rafferty *et al.* [22]. In order to achieve complete flattening of the sintering curve, which indicates complete sintering, the particle size has to be reduced to about

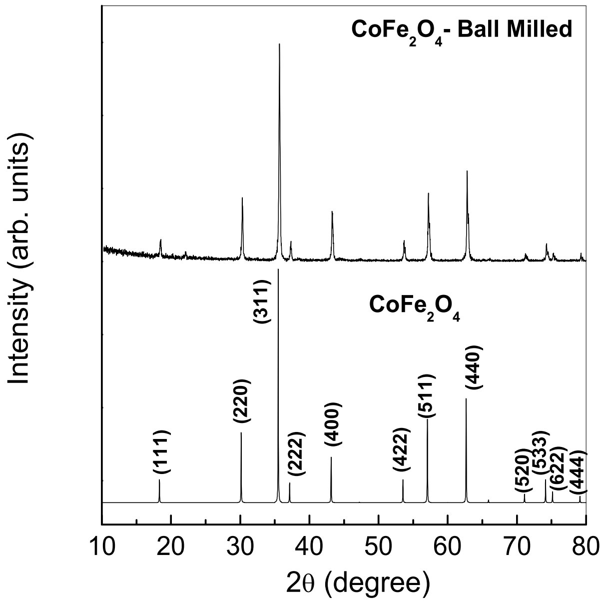

Figure 3.16: Powder XRD pattern of ball milled cobalt ferrite and the simulated pattern for cobalt ferrite.

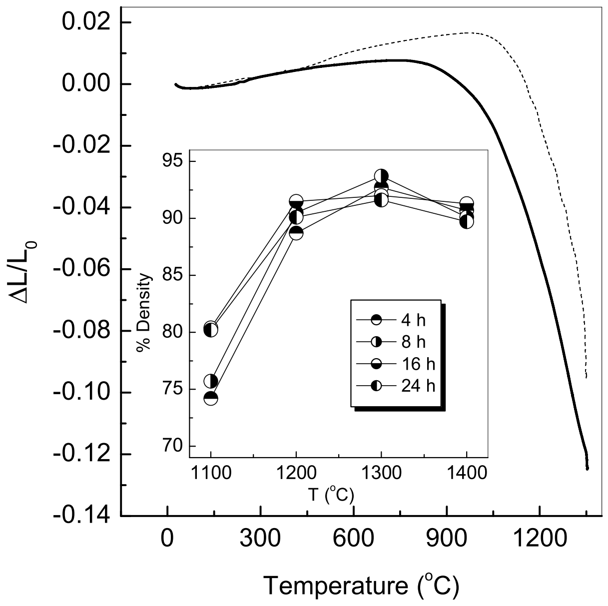

Figure 3.17: Sintering behavior of the ball milled powder (solid line) and powder prepared from standard ceramic technique (dashed line) recorded using TMA. Inset shows the density of the sintered pellets as a function of temperature.

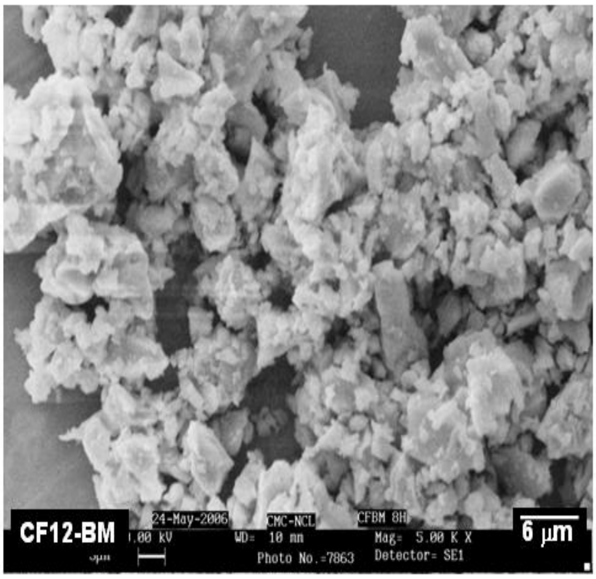

Figure 3.18: Scanning electron micrograph of the cobalt ferrite powder ball milled for 8 hours.

2μm [22].

The inset in figure 3.17 shows the variation of the density of the sintered discs as a function of sintering temperature. The density is expressed as the percentage of theoretical density of cobalt ferrite (5.296 g/cm^3). Lower densities are observed for the samples sintered at 1100 °C. The sample sintered at 1100 °C for 4 h shows the lowest density of $\sim$74%. The difference between the densities of the samples sintered for 4 h and 24 h decreases with increasing sintering temperature. However, at a given temperature, the density initially increases with sintering time and then decreases, so that the maximum density is obtained for the samples sintered for 8 h. There is not much variation in the sintered densities with dwell time when sintered at 1400 °C. A maximum sintered density of 93% is obtained for samples sintered at higher temperatures.

3.5.4 Microstructural Analysis

The scanning electron micrograph of the ball milled powder is shown in figure 3.18. The particles are found to be agglomerated but the average particle size is found to be around 5 μm. The microstructure of the samples sintered for different temperatures and dwell times are shown in figure 3.19. As can be seen from the figure, there is a systematic variation in the microstructure with increasing dwell time and sintering temperature. Systematic microstructural changes are observed with increasing dwell time at a specific sintering temperature. The sample sintered at 1100 °C shows the presence of very small grains. The SEM studies reveal that the grain size increases drastically when the sintering temperature is increased above 1200 °C and indicate large grain growth when sintered above 1300°C. The samples sintered at 1400 °C, however, show relatively porous microstructures. The relatively lower densities of the samples sintered at 1400 °C can be, therefore, attributed to the increased porosities of these samples. Such an increase in the porosity of the ferrite materials at higher sintering temperatures has been observed in the case of Mn-Zn ferrite powders prepared by hydrothermal route by Rozman *et al.* [57]. This behavior has been attributed to the release of oxygen from the spinel lattice.

Scanning electron micrographs of the samples sintered at 1100 °C for 8 h with 1% additives are shown in figure 3.20. A comparison of the micrographs of the samples sintered with out any additive, and sintered with TiO_2, with Y_2O_3 and with Nb_2O_5 shows that no noticeable grain growth has taken place with the additives, except when Nb_2O_5 is used. However, the TiO_2 added sample exhibits a less porous microstructure when compared to the virgin sample and the porosity remains almost the same when Y_2O_3 is used as the additive. The densities of the samples sintered with Nb_2O_5, TiO_2, and Y_2O_3 are obtained as 91%, 80%, and 76%, respectively, compared to the density of 75% for the virgin sample. Thus, better sintered density with out any grain growth is attained for the TiO_2 added sample.

3.5.5 Magnetic Measurements

The room temperature magnetization curves of the sintered samples are shown in figure 3.21. The magnetization is not saturated at the highest field of 15 kOe used for the measurement. The magnetization of the sample sintered at 1100 °C is not much improved from that of the powder sample (∼78 emu/g). This may be attributed to the lower density and highly porous nature of the samples sintered at this temperature. As the sintering temperature is enhanced to 1200 °C and upwards an enhanced magnetization of around 81 emu/gm is observed. There is a continuous decrease in the coercivity with increasing

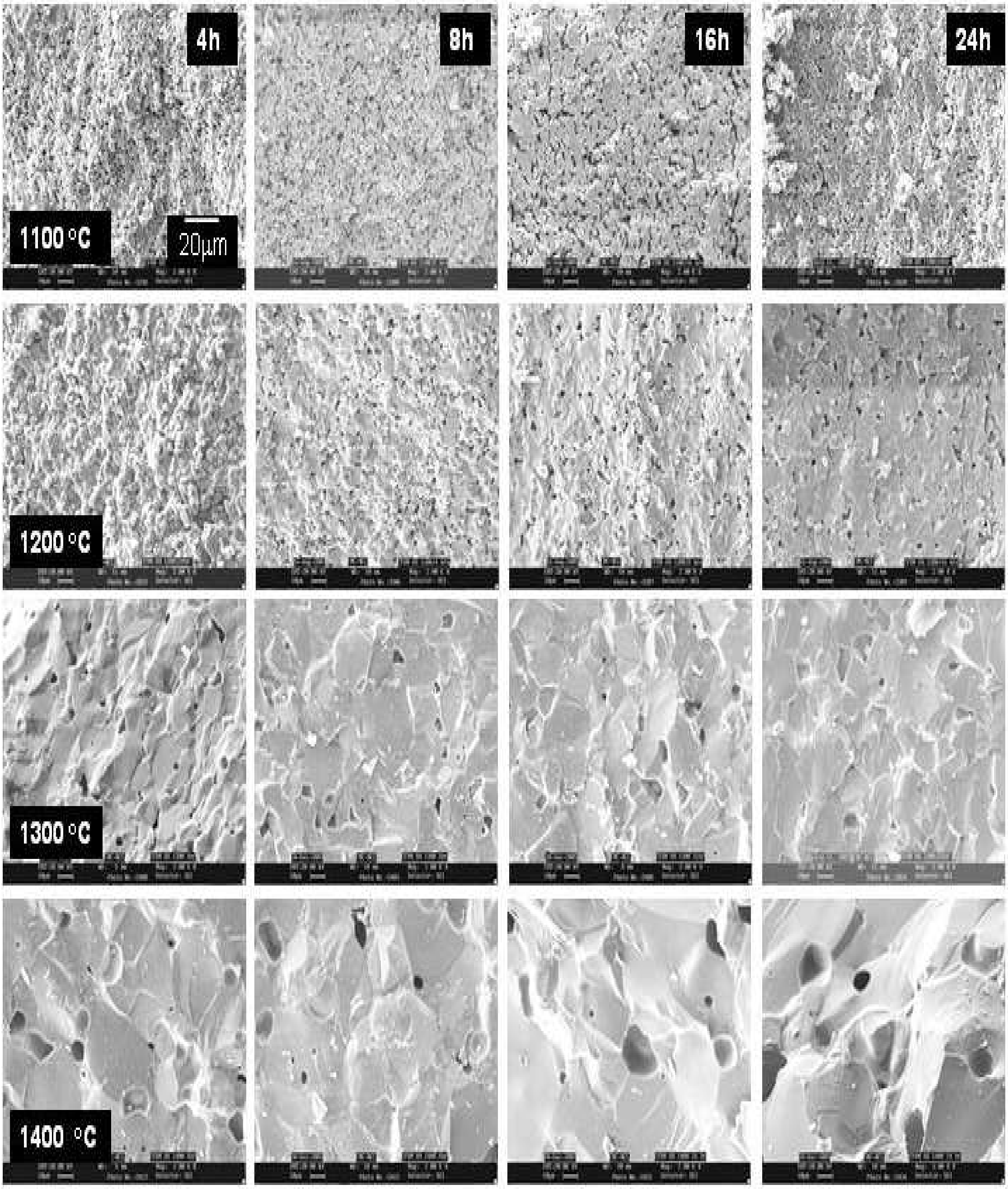

Figure 3.19: Scanning electron micrographs of the samples sintered at various temperatures for different dwell times.

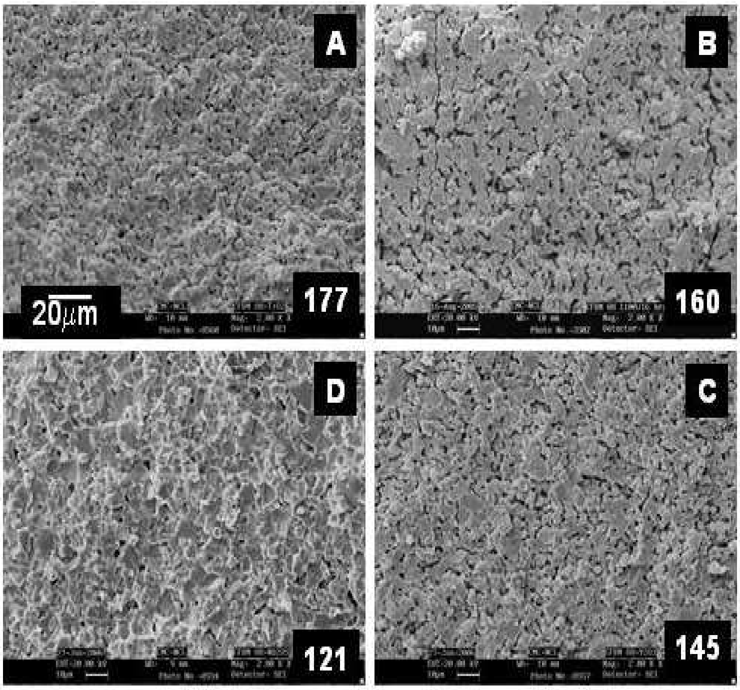

Figure 3.20: Scanning electron micrographs of the samples sintered at 1100 °C for 8 h, with the presence of 1% additives, (A) TiO_2, (B) no additive (C) Y_2O_3, and (D) Nb_2O_5.

sintering temperature and this is due to the increase in the grain size as evidenced from the SEM photographs. The variation of coercivity and magnetization with sintering temperature is shown in figure 3.22. Na *et al.* have studied the effect of cation distribution on the magnetic properties of cobalt ferrite [58]. According to their report, the coercivity and magnetization of cobalt ferrite were found to change with the quenching temperature. Such changes were correlated with the varying distribution of Co and Fe ions in the octahedral and tetrahedral sites of the spinel structure.

The temperature dependence of magnetization of some of the sintered samples is shown in figure 3.23. The observed Curie temperatures are much less than that obtained for the samples synthesized in smaller quantities by the ceramic and low-temperature methods (520 °C, see figure 3.13). The Curie temperatures observed for the samples sintered at different temperatures are listed in Table 3.3. The lower and different Curie temperatures obtained for the ball milled samples is likely to be due to the difference in the distribution of the ions in the spinel lattice. Different Curie temperatures between 450 to 525 °C have been already reported for cobalt ferrite [59–62]. Changing the degree of cation distribution

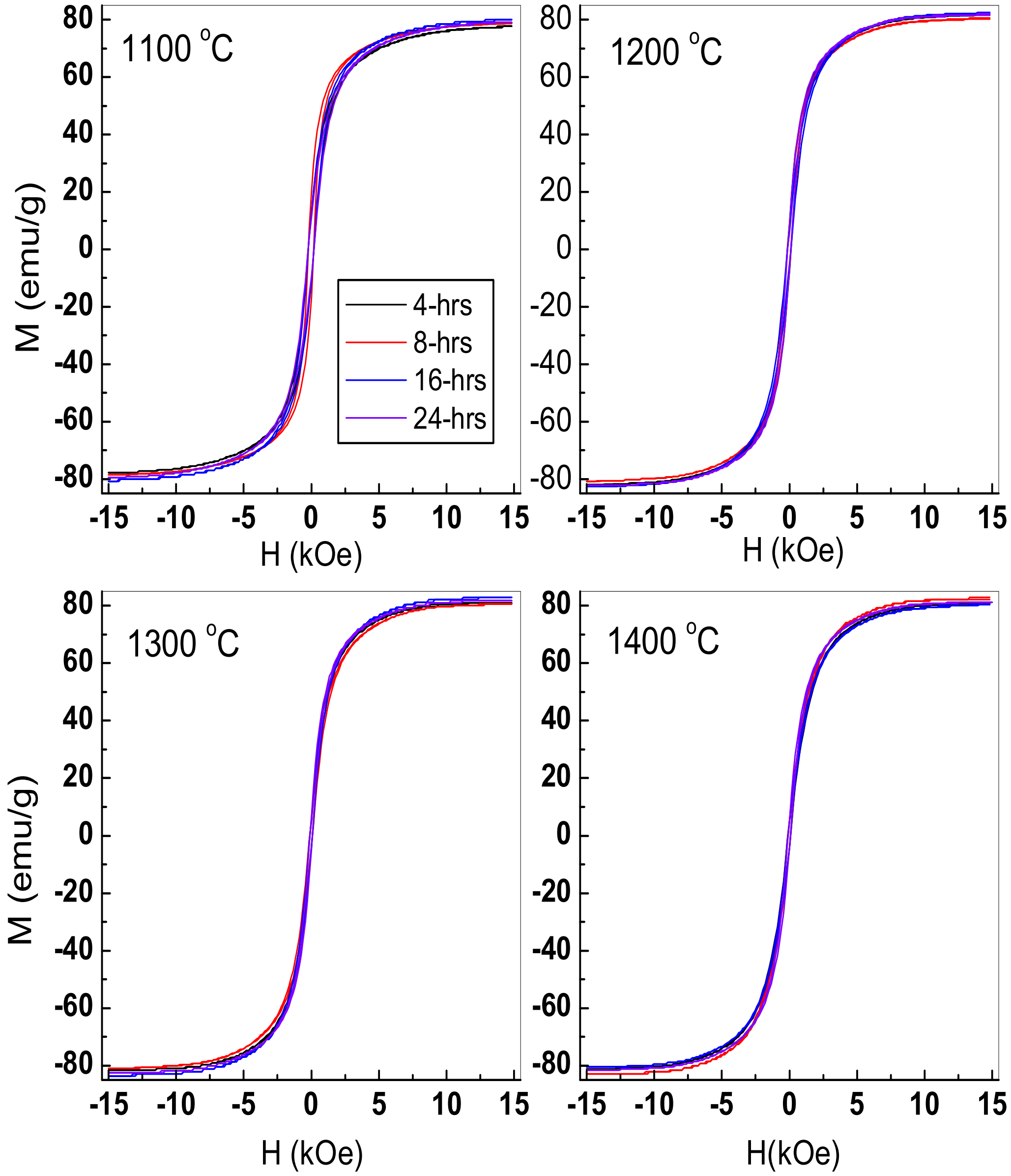

Figure 3.21: Room temperature magnetization curves for the samples sintered at various temperatures as indicated.

Table 3.2: Comparison of the Curie temperatures of samples sintered at different temperatures and duration.

Sintering Temp (°C)	Sintering Time (h)	T_C (°C)
1100	4	483
1200	8	473
1300	16	478
1400	24	477

is expected to considerably affect the magnetic transition temperature of the ferrites [63]. The effect of sintering temperature on the magnetic properties of cobalt ferrite has been studied by Rieck and Thijssen [64]. Paulsen *et al.* showed that varying the sintering temperature may lead to a slightly modified cation distribution of Co and Fe ions thereby reducing the Curie temperature [65].

3.5.6 Magnetostriction Studies

The magnetostriction curves measured at room temperature in the parallel direction with respect to the applied magnetic field, up to a magnetic field strength of 10 kOe are shown in figure 3.24. The value of magnetostriction is dependent on the sintering temperature as well as the sintering time. The observed maximum magnetostriction values are ranging between 130 to 165 ppm. The maximum value of magnetostriction is observed for the sample sintered at 1100 °C for 24 h with a magnetostrictive strain of 165 ppm. For a particular dwell time, the magnetostriction is largest for the sample sintered at 1100 °C, then decreases with increasing sintering temperature to 1200 °C and again increased after sintering above 1200 °C. Unexpectedly, larger magnetostriction is observed for the sample sintered at 1200 °C for 4 h. The lowest magnetostriction is observed in case of the sample sintered at 1200 °C for 8 h. The observed values of magnetostriction are higher than that reported earlier for polycrystalline cobalt ferrite [17], but less than that reported recently by Paulsen *et al.* [47]. This difference in the magnitude of magnetostriction may be due to the difference in the processing conditions of our samples.

The magnetostriction curves recorded in the perpendicular direction with respect to the applied magnetic field are shown in figure 3.25. As can be seen from the figure,

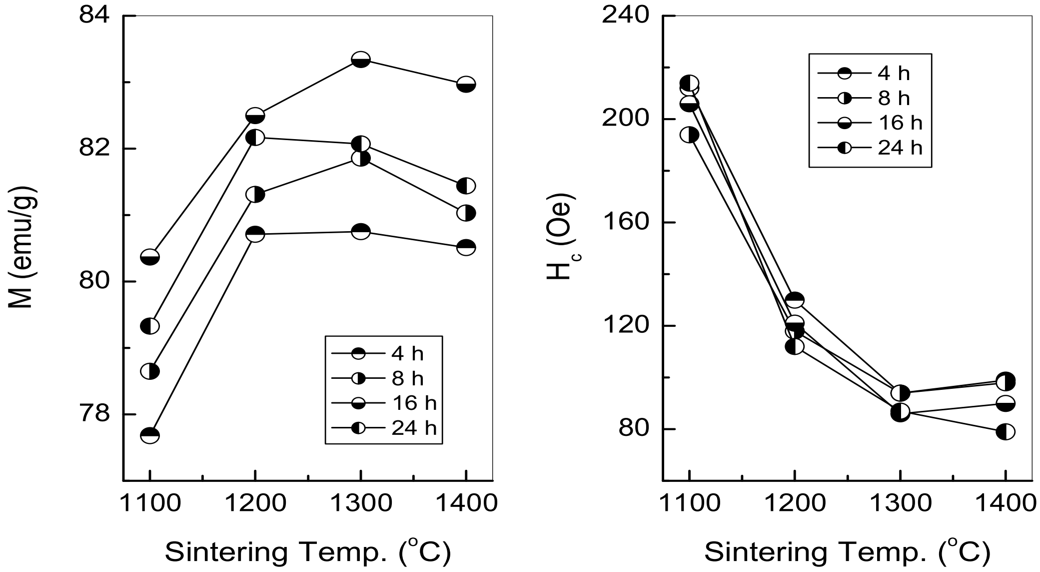

Figure 3.22: Variation of magnetization (at 15 kOe) and coercivity as a function of sintering temperature for different dwell times.

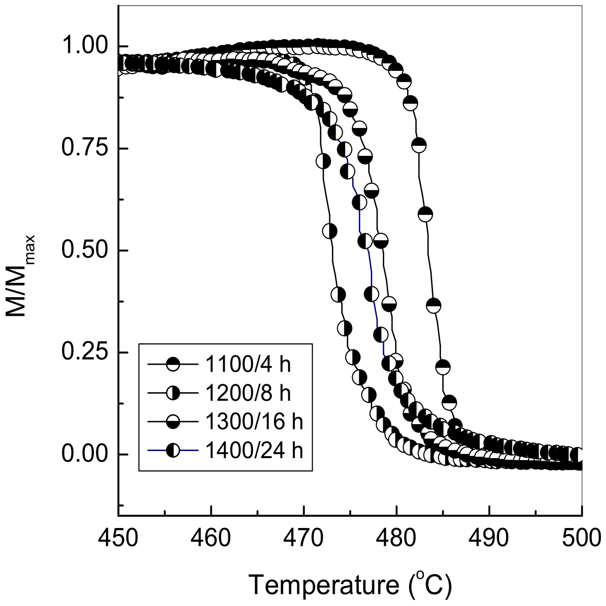

Figure 3.23: Temperature dependence of magnetization for the samples sintered at different temperatures.

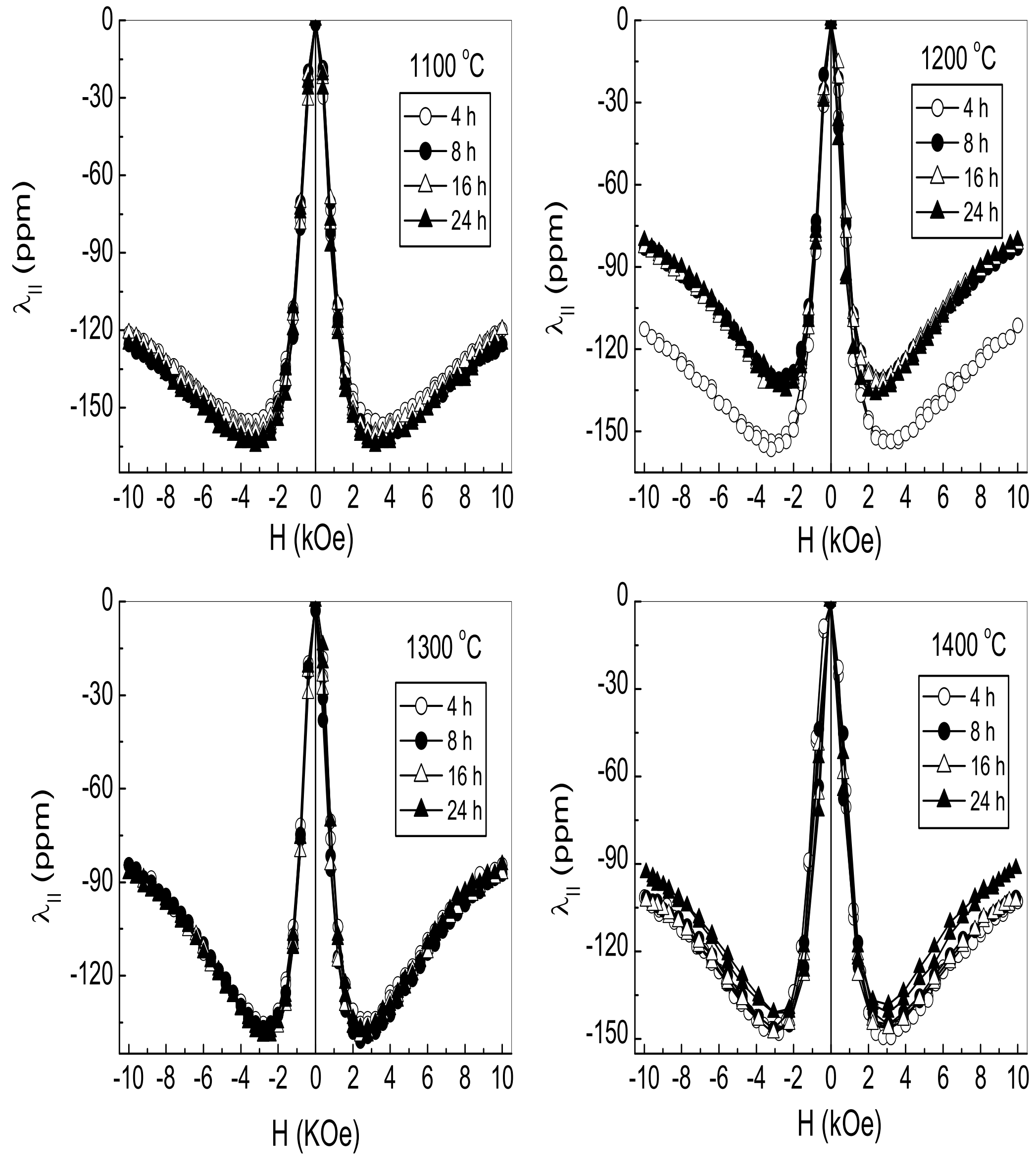

Figure 3.24: Magnetostriction curves recorded in the parallel direction to the applied magnetic field for samples sintered at different temperatures, as indicated.

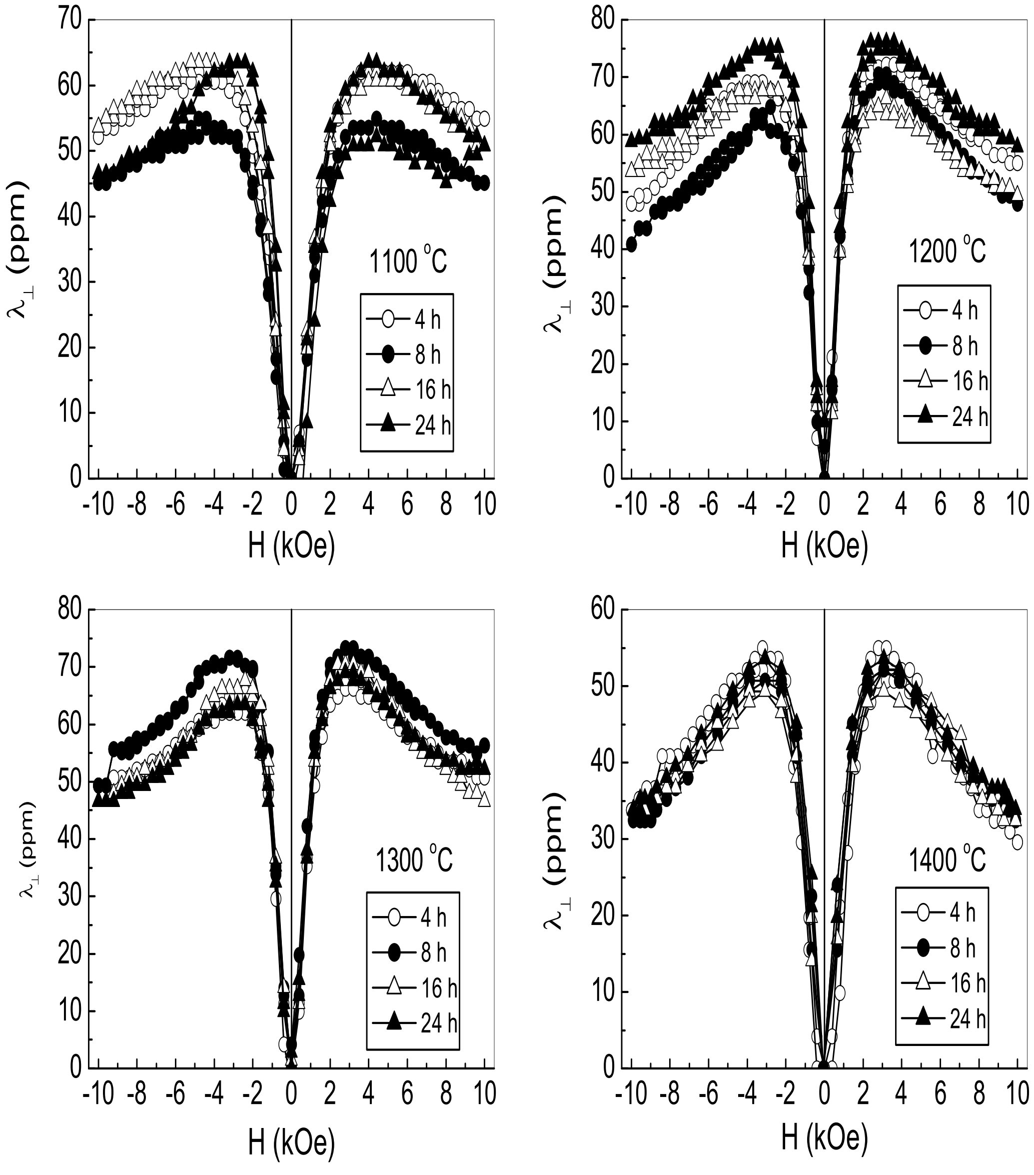

Figure 3.25: Magnetostriction curves recorded in the perpendicular direction to the applied magnetic field for different samples.

the sign of the magnetostriction in the perpendicular direction is positive. A maximum magnetostriction of 75 ppm is observed for the sample sintered at 1200 °C. The values are in between a minimum of 50 to a maximum value of 75 ppm for the samples sintered at various temperatures.

Along the parallel direction, the magnetic field strength at which the maximum value of magnetostriction is observed, (H_{max}), is found to be between 2 kOe to 3 kOe for all the samples. The slope of the magnetostriction curve ($d\lambda/dH$) is also found to be dependent on the sintering time and temperature. The rate of change of magnetostriction below the maximum at low fields is the maximum for samples sintered at 1100 °C and further decreases as the sintering temperature is increased. The variations of the slope of the parallel magnetostriction curves and the maximum of magnetostriction as a function of the sintering temperature are shown in figure 3.26. The samples sintered at 1100 °C show the maximum slope change. A value of 102 ppm/Oe is observed for the sample sintered at 1100 °C for 24 h. The slope values for all the samples are found to be between 80 to 105 ppm/Oe. These values are comparable to that reported by Mcallum *et al* [46]. The slope of the magnetostriction curve is very important for utilizing these materials for stress sensing applications [66].

A comparison of the various parameters listed in Table 3.3 shows that magnetostriction is highest when the magnetization and density are lower and the coercivity is larger. However, this seems to be not a true correlation as the magnetization is dependent on the density of the samples and the coercivity depends on grain size. A close comparison of the micrographs and the magnetostriction curves shows that there is some sort of a dependence of the magnetostrictive strain on the microstructure of the sintered compacts. The samples sintered at 1100 °C are having the smallest grains of size ∼2 μm and there is not much increase in the grain size as the sintering time is increased from 4 h to 24 h. Though the densities of the samples sintered at 1100 °C are smaller than those of the samples sintered at higher temperatures, there is a direct correlation between the density and dwell time. The density is increased from ∼75% to ∼80% with increasing dwell time. Similarly, for the sample sintered at 1200 °C for 4 h and showing relatively larger strain, the grains are smaller and the microstructure is comparable to that of the sample sintered at 1100 °C. A comparison between the density, microstructure and

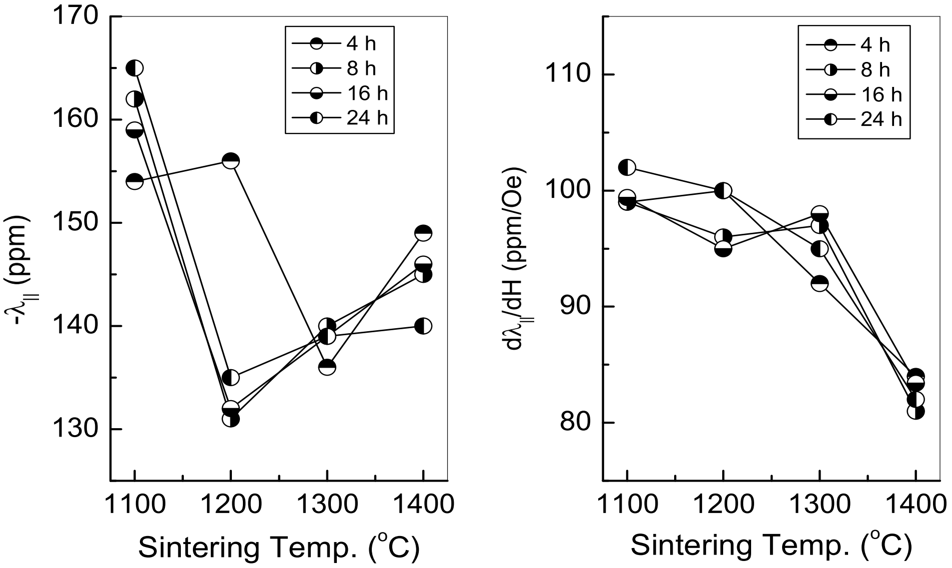

Figure 3.26: Variation of maximum magnetostriction and slope of magnetostriction as a function of the sintering temperature.

magnetostriction indicates that higher sintered density with smaller grain size is essential for larger magnetostriction.

In order to confirm the correlation between grain size and magnetostriction, and the role played by microstructural features, some studies were made on the effect of a sintering aid on the microstructural and magnetostrictive properties. Samples were sintered at 1100 °C for 8 h with 1% each of TiO_2, Y_2O_3 and Nb_2O_5 as additives. These three metal oxides are known to play different roles for grain growth during sintering [67]. Nb_2O_5 forms liquid phase with the ferrite and promotes planar grain growth forming abnormal and matrix grains. Y_2O_3 is known to be inactive and TiO_2 promotes grain growth without liquid phase sintering. However, the temperature at which the powders are sintered with the additives (1100 °C) may not be sufficient for the full action of the sintering aids. This sintering temperature was selected because higher strains are obtained after sintering at this temperature with out any sintering aids. From SEM studies (see figure 3.20) it was found that there is not much grain growth taken place when the additives are used, except when Nb_2O_5 is used and the sample sintered with TiO_2 exhibited a less porous microstructure.

Table 3.3: Summary of magnitude of maximum magnetostriction $\lambda_{\parallel}$, H_c and M_s for the samples sintered at various temperatures.

Sintering Temp.	Sintering Time											
	4h			8 h			16 h			24 h		
	$\lambda_{\parallel}$	H_c	M_s	$\lambda_{\parallel}$	H_c	M_s	$\lambda_{\parallel}$	H_c	M_s	$\lambda_{\parallel}$	H_c	M_s
1100°C	-154	212	77.6	-162	197	78.7	-159	206	80.0	-165	214	79.0
1200°C	-156	130	81.7	-131	118	80.5	-132	121	82.4	-135	112	82.0
1300°C	-136	94	81.0	-140	94	80.5	-139	86	82.0	-139	86	81.0
1400°C	-149	99	80.7	-145	97	82.9	-146	90	81.5	-140	78	81.0

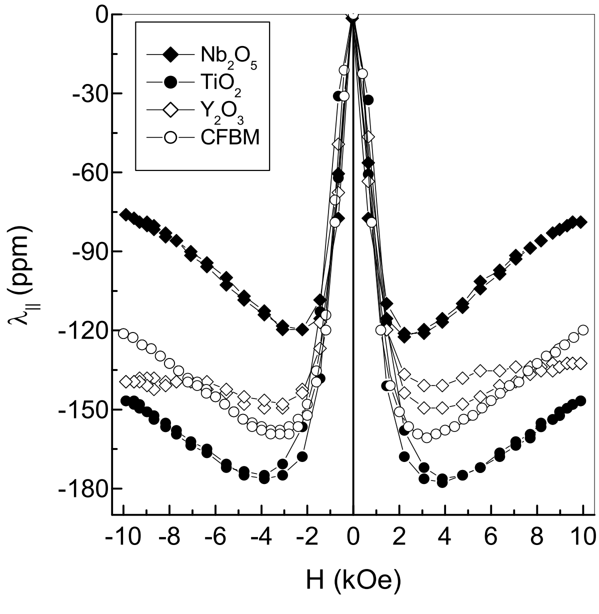

Figure 3.27: Magnetostriction as a function of magnetic field for the samples with Nb_2O_5, Y_2O_3 and TiO_2 as additives and without additive (CFBM).

The magnetostriction curves of the samples sintered with the additives along with that of the corresponding sample sintered without any additive are compared in figure 3.27. An increase in the magnetostriction is observed when TiO_2 is used as the additive and the magnetostriction is found to be decreased slightly when Y_2O_3 is used. The lowest value of magnetostriction is observed in the case of the Nb_2O_5 added sample. The sample sintered with titanium dioxide as the sintering aid shows an enhanced value of magnetostriction of 177 ppm whereas the samples sintered with Y_2O_3 and Nb_2O_5 exhibit magnetostrictive strains of 149 and 121 ppm, respectively, as compared to 159 ppm of the virgin sample. However, the maximum of the magnetostriction is observed at a relatively higher magnetic field strength of 3.8 kOe as compared to 2.8 kOe of the parent sample. The enhancement in the magnetostriction found for the sample with TiO_2 as a sintering aid can be attributed to the presence of smaller grains with uniform distribution of the grains in the sintered compact. Thus, better sintered density with out any grain growth is likely to be the possible factors responsible for the enhanced magnetostriction. Similar grain size dependence of magnetostrictive strain is reported in the case of Fe-Pd ferromagnetic shape memory alloys by Yasuda *et al.* [68] and $Tb_{0.3}Dy_{0.7}Fe_2$ thin films formed by flash evaporation process [69].

3.6 Conclusions

Sintered polycrystalline cobalt ferrite has been studied in detail for its magnetostrictive behavior. Initial studies on different compositions in the series $Co_xFe_{3-x}O_4$ showed that the compositions with $x = 1.0$, 1.1, and 1.2 show better magnetostrictive properties. However, higher sintering temperatures are required in order to have a material with enhanced density. The studies performed on the nanosized cobalt ferrite showed that the magnetostrictive properties can be enhanced by starting from nanosized particles and by changing the synthesis route. The samples prepared using three different low-temperature methods resulted in the nanosized powders of cobalt ferrite and show enhanced magnetostrictive behavior as compared to the one synthesized by conventional high temperature methods of synthesis. A very good correlation is observed between the magnetostriction and the microstructure of the sintered materials. Magnetostrictive strain as high as 197 ppm is observed for combustion synthesized sample, which after sintering exhibits a uniform microstructure with presence of smaller sized grains. This is further confirmed by studies on ball milled cobalt ferrite. The effect of sintering temperature, dwell time and sintering aids on the microstructure and magnetostrictive properties of ball milled cobalt ferrite have been evaluated. The sintering studies reveled that sintering temperatures can be reduced to as low as 1100 °C by using the ball milling method, thereby restricting the grain growth and enhancing the magnitude of the magnetostrictive strain. The studies performed with sintering aids also support the observation that the presence of small and uniform sized grains along with better sintered density is one of the essential parameters for enhancing the magnetostrictive performance of cobalt ferrite.

References

[1] S. L. Blum, *J. Am. Ceram. Soc.* 41 (1958) 489.

[2] A. Goldman, *Modern Ferrite Technology* (Van Nostrand Reinhold, New York, 1990).

[3] I. C. Heck, *Magnetic Materials and their Applications* (Butterworth & Co. Pub. Ltd, London, 1974).

[4] W. A. Kaczmarek, *J. Magn. Magn. Mater.* 157-158 (1996) 264.

[5] S. Bid and S. K. Pradhan, *Mater. Chem. Phys.* 82 (2003) 27.

[6] C. N. R. Rao, *Chemical Approaches to the synthesis of Inorganic Materials* (Wiley Eastern Ltd., New Delhi, 1994).

[7] O. Masala and R. Seshadri, *Annu. Rev. Mater. Res.* 34 (2004) 41.

[8] T. Nakamura, *J. Magn. Magn. Mater.* 168 (1997) 285.

[9] S. Komarneni, E. Fregeau, E. Breval and R. Roy, *J. Am. Ceram. Soc.* 71 (1988) C-26.

[10] S. Deka and P. A. Joy, *J. Am. Ceram. Soc.* 90 (2007) 1494.

[11] C. A. Domenicali, *Phys. Rev.* 78 (1950) 458.

[12] R. M. Bozorth and J. G. Walker, *Phys. Rev.* 88 (1952) 1209.

[13] C. Guillad, *Rev. Mod. Phys.* 25 (1953) 64.

[14] L. R. Bickford Jr, J. Pappis and J. L. Stull, *Phys. Rev.* 99 (1955) 1210.

[15] R. M. Bozorth, E. F. Tilden and A. J. Williams, *Phys. Rev.* 99 (1955) 1788.

[16] J. C. Slonczewski, *Phys. Rev.* 122 (1961) 1367.

[17] J. Smith and H. P. J. Wijn, *Ferrites* (Philiphs Technical Library, Eindhoven, 1953).

[18] R. C. Panda, J. C. Shih and T. S. Chin, *J. Magn. Magn. Mater.* 257 (2003) 79.

[19] Z. Zhang, A. J. Rondinone, J-X. Ma, J. Shen and S. Dai, *Adv. Mater.* 17 (2005) 1415.

[20] R. Sani, A.Beitollahi, Y. V. Maksimov and I. P. Suzdalev, *J. Mater. Sci.* 42 (2007) 2126.

[21] M. H. Khedr, A. A. Omar and S. A. Abdel-Moaty, *Colloids Surf.* A 281 (2006) 8.

[22] A. Rafferty, T. Prescott and D. Brabazon, *Cer. Int.* (2006), doi:10.1016/j.ceramint.2006.07.012

[23] Y. Kim, D. Kim and C. S. Lee, *Physica* B 337 (2003) 42.

[24] E. Uzunova, D. Klissurski, I. Mitov and P. Stefanov, *Chem. Mater.* 5 (1993) 576.

[25] X. Yang, X. Wang and Z. Zhang, *J. Crystal Growth* 277 (2005) 467.

[26] G. B. Ji, H. L. Su, S. L. Tang and B. L. Xu, *Chem. Lett.* 34 (2005) 86.

[27] J-G. Lee, J. Y. Park and C. S. Kim, *J. Mater. Sci.* 33 (1998) 3965.

[28] J. G. S. Duque, M. A. Maceado, N. O. Moreno, J. L. Lopez and H. D. Pfanes, *J. Magn. Magn. Mater.* 226-230 (2001) 1424.

[29] E. J. Choi, Y. Ahn, S. Kim, D. H. An, K. U. Kang, B. -G. Lee, K. S. Baek and H. N. Oak, *J. Magn. Magn. Mater.* 262 (2003) L198.

[30] D. Makovec, A. Kosak, A. Zindarsic and M. Drofenik, *J. Magn. Magn. Mater.* 289 (2005) 32.

[31] V. Pillai and D. O. Shah, *J. Magn. Magn. Mater.* 163 (1996) 243.

[32] I. Chassing, L. Presmanes, P. Tailheads and A. Rousset, *Solid State Ionics* 58 (1992) 261.

[33] O. Carp, L. Patron and A. Reller, *Mater. Chem. Phys.* 101 (2007) 142.

[34] C. H. Yan, Z. -G. Xu, F.-X. Cheng, Z. -M. Wang, L. -D. Sun, C. -S. Liao and J. -T. Jia, *Solid. State. Commun.* 111 (1999) 287.

[35] N. Kikukawa, M. Takemori, Y. Nagano, M. Sugawasa and S. Kobayashi, *J. Magn. Magn. Mater.* 284 (2004) 206.

[36] P. D. Thang, G. Rijnders and D. H. A. Blank, *J. Magn. Magn. Mater.* 295 (2005) 251.

[37] L. J. Cote, A. S. Teja, A. P. Wilkinson and Z. J. Zhang, *Fluid Phase Equilib.* 210 (2003) 307.

[38] N. Millot, B. Xin, C. Pighini and D. Aymes, *J. Eur. Ceram. Soc.* 25 (2005) 2013.

[39] M. Rajendran, R. C. Pullar, A. K. Bhattacharya, D. Das, S. N. Chnitalapudi and C. K. Mujumdar, *J. Magn. Magn. Mater.* 232 (2001) 71.

[40] I. Hilger, R. Hergt and W. A. Kaiser, *J. Magn. Magn. Mater.* 293 (2005) 314.

[41] D. Zhang, X. Zhang, X. Ni, J. Song and H. Zheng, *J. Magn. Magn. Mater.* 305 (2006) 68.

[42] Ph. Tailheads, C. Villete, A. Rousset, G. U. Kulkarni, K. R. Kannan, C. N. R. Rao and M. Lenglet, *J. Solid State Chem.* 141 (1998) 56.

[43] D. H. Lee, H. S. Kim, J. Y. Lee, C. H. Yo and K. H. Kim, *Solid State Commun.* 96 (1995) 445.

[44] A. F. Junior, E. C. O. Lima, M. A. Novak and P. R. Wells Jr., *J. Magn. Magn. Mater.* 308 (2007) 198.

[45] J. Ding, P. C. McCormick and R. Street, *Silod State Commun.* 95 (1995) 31.

[46] R. W. McCallum, K. W. Dennis, D. C. Jiles, J. E. Snyder and Y. H. Chen, *Low. Temp. Phys.* 27 (2001) 266.

[47] J. A. Paulsen, A. P. Ring, C. C. H. Lo, J. E. Snyder and D. C. Jiles, *J. Appl. Phys.* 97 (2005) 044502.

[48] F. S. Galasso, *Structure and Properties of Inorganic Solids* (Pergamon Press, Oxford, 1970).

[49] L. A. Chick, L. R. Pederson, G. D. Maupin, J. L. Bates, L. E. Thomas and G. J. Exarhos, *Mater. Lett.* 10 (1990) 6.

[50] S. Ounnunkad, *Solid State Commun.* 138 (2006) 472.

[51] W-C. Hsu, S. C. Chen, P. C. Kuo, C. T. Lie and W. S. Tsai, *Mater. Sci. Eng.* B 111 (2004) 142.

[52] Z. Yue, J. Zhou, X. Wang, Z. Gui and L. Li, *J. Mater. Sci. Lett.* 20 (2001) 1327.

[53] R. Basu, F. Tietz, E. Wessel, H. P. Buchkremer, *Mater. Res. Bull.* 39 (2004) 1335.

[54] M. Shi, N. Liu, Y. Xu, Y. Yuan, P. Majewski and F. Aldinger, *J. Alloys Compd.* 425 (2006) 348.

[55] T. Mimani, *J. Alloys Compd.* 315 (2001) 123.

[56] R. A. Dunlap, D. A. Small, G. R. MacKay, J. W. O'Brien, J. R. Dahn and Z. H. Cheng, *Can. J. Phys* 78 (2000) 211.

[57] M. Rozmann and M. Drofenik, *J. Am. Ceram. Soc.* 81 (1998) 1757.

[58] J. G. Na, T. D. Lee and S. J. Park, *J. Mater. Sci. Lett.* 12 (1993) 961.

[59] S. A. Patil, V. C. Mahajan, A. K. Ghatage and S.D. Lotke, *Mater. Chem. Phys.* 57 (1998) 86.

[60] P. N. Vasambekar, C. B. Kolekar and A.S. Vaingankar, *Mater. Chem. Phys.* 60 (1999) 282.

[61] P. A. Joy and S. K. Date, *J. Magn. Magn. Mater.* 222 (2000) 33.

[62] O. Caltun, G. S. N. Rao, K. H. Rao, B. P. Rao, I. Dumitru, C. -O. Kim and C. Kim, *J. Magn. Magn. Mater.* 316 (2007) e618.

[63] G. A. Sawatzky, F. Van Der Woulde and A. H. Morrish, *Phys. Rev.* 187 (1969) 747.

[64] G. D. Rieck and J. J. M. Thijssen, *Acta. Crystallgr.* B24 (1968) 982.

[65] J. A. Paulsen, C. C. H. Lo, J. E. Snyder, A. P. Ring, L. L. Jones and D. C. Jiles, *IEEE. Trans. Magn.* 39 (2003) 3316.

[66] D. C. Jiles, *J. Phys. D: Appl. Phys.* 28 (1995) 1537.

[67] M. F. Yan and D. W. Jonson Jr., *J. Am. Ceram. Soc.* 61 (1978) 342.

[68] H. Y. Yasuda, M. Komoto, M. Ueda and Y. Umakoshi, *Sci. Technol. Adv. Mat.* 3 (2002) 165.

[69] M. Wada, H. Uchida and N. Kaneko, *J. Alloys Comp.* 258 (1997) 143.

Chapter 4

Magnetostriction Studies on Mn Substituted Cobalt Ferrite

4.1 Introduction

The spinel structure allows the introduction of different metal ions into the crystal lattice which can change the electrical and magnetic properties of the resulting compositions considerably. The effect of substitution of various magnetic as well as nonmagnetic ions such as Ti, Al, Zn, Cd, Cr etc., for cobalt and iron in $CoFe_2O_4$ has been studied by several researchers [1–8]. Such a substitution also affects the distribution of Fe ions in the octahedral and tetrahedral sites of the spinel lattice, thereby considerably changing the magnetic and electrical properties. A very small amount of substitution can also affect the initial permeability and therefore could affect the magnetomechanical response. Greenough and Lee have earlier studied the contribution of Co^{2+} ions on the magnetostriction constants of single crystals in the series $Co_xMn_{1-x}Fe_2O_4$, grown by flame fusion method [9]. The theoretical aspects of substituting Mn for Co and Fe, on the magnetostriction constants of cobalt ferrite were studied by Pointon *et al.* [10]. The *ab initio* calculations were performed in order to understand the effect of Mn ions on the magnetostriction constants λ_{100} and λ_{111}. These studies showed that the Mn^{3+} ions in the octahedral sites have negligible contribution whereas Mn^{3+} ions in the tetrahedral sites have a significant contribution towards magnetostriction. These calculations were based on a single ion model, assuming that the crystal potential can be calculated at the Mn^{3+} ions on a point charge approximation. It was also shown that Mn^{4+} ions, if present in the tetrahedral sites, could be an additional source of magnetostriction. However, the Mn^{4+} ions in the octahedral site do not contribute to magnetostriction. These studies revealed the importance of Mn substitution in determining the magnetostrictive behavior of cobalt ferrite.

In Mn substituted cobalt ferrite, Mn^{3+} ions will have a strong preference for octahedral sites when substituted for Fe^{3+}, like in $CoMn_2O_4$ [11]. On the other hand Mn^{2+} ions will have a stronger preference for tetrahedral sites when substituted for Co^{2+} as in $MnFe_2O_4$. Cobalt ferrite and Mn substituted cobalt ferrite has been proposed to be one of the suitable materials for stress sensing applications [12]. There is a strong demand for materials exhibiting higher magnetostrictive strains at low magnetic strengths. Recently Paulsen *et al.* have reported that the stress sensitivity, Curie temperature, and magnetostriction of cobalt ferrite can be changed by substituting Mn for Fe in $CoFe_2O_4$ [13]. Caltun *et al.* have recently studied the effect of Mn substitution for Fe in the series $CoFe_{2-x}Mn_xO_4$ ($0.0 \leq x \leq 0.6$) and found that by adjusting the Mn content and the sintering process, these materials could be optimized for use in magnetomechanical stress sensors [14, 15]. These studies indicate that it is possible to tune the magnetic as well as the magnetostrictive properties of cobalt ferrite by substituting Mn for Fe. The Mössbauer spectral investigations performed on $CoFe_{2-x}Mn_xO_4$ showed that substituting Mn for Fe displaces the cobalt on octahedral sites to the tetrahedral sites [16]. Similarly, Melikhov *et al.* have evaluated the changes in the magnetic anisotropy of $CoFe_{2-x}Mn_xO_4$ and found that anisotropy decreases with increasing Mn content [17]. This is again attributed to the displacement of Co from the octahedral sites by Mn, as the very large anisotropy of the ferrite is due to the Co in the octahedral sites. The ionic radii of Co^{2+} and Fe^{3+} are very sensitive to the coordination. The ionic radii of different ions in the octahedral and tetrahedral coordinations are shown in Table 4.1.

Since it is the Co^{2+} ion which has an enormous effect on the magnetostriction and anisotropy of $CoFe_2O_4$, it is desirable to understand the effect of direct substitution of Co by Mn on the magnetostrictive properties of cobalt ferrite. However, the effect of substitution of Mn for Co in cobalt ferrite is not reported in the literature.

4.2 Studies on Mn Substituted Cobalt Ferrite

The studies carried out in the present work analyze the effect of substitution of Mn for Fe and Co on the magnetic and magnetostrictive behavior of cobalt ferrite. The effect of substitution of Mn has been investigated here in detail in two particular compositions

Table 4.1: Effective ionic radii for Fe, Co and Mn in the tetrahedral and octahedral coordinations, taken from reference [18].

Ion	IV coordination (Å)	VI coordination (Å)
Fe^{2+}	0.63	0.78
Fe^{3+}	0.49	0.645
Co^{2+}	0.58	0.745
Co^{3+}	–	0.61
Mn^{2+}	0.66	0.83
Mn^{3+}	–	0.645

$CoFe_2O_4$ and $Co_{1.2}Fe_{1.8}O_4$. These two compositions were found to show higher magnetostriction from the studies performed in the series $Co_xFe_{3-x}O_4$ as discussed in chapter 3. This chapter deals with the magnetic and magnetostrictive properties of Mn substituted $CoFe_2O_4$, in which Mn is gradually substituted for Co, and comparison of the effect of substitution of Mn for both Co and Fe in $Co_{1.2}Fe_{1.8}O_4$. Earlier reports on the substitution of Mn for Fe in $CoFe_2O_4$ showed a constant decrease in the magnetostrictive strain, along with a decrease in the Curie temperature [13]. However, substitution of Mn for Fe is not likely to affect the cation distribution, since Mn^{3+} ions will have octahedral site preference as in $CoMn_2O_4$. The substitution of Mn for Co will significantly affect the cation distribution in the octahedral and tetrahedral sites, since Mn^{2+} is likely to occupy the tetrahedral sites, as in the case of $MnFe_2O_4$. Thus, the resulting changes in the cation distribution will in turn affect the magnetic and magnetostrictive behavior.

4.2.1 Synthesis

All the compositions in the $Co_{1-x}Mn_xFe_2O_4$ (CMF) series ($0.0 \leq x \leq 0.4$) were synthesized by the conventional ceramic method. Stoichiometric amounts of $CoCO_3$, Fe_2O_3 and MnO_2 were mixed together in an agate mortar with acetone as a mixing medium. The mixtures were pre-calcined at 1000 °C for 12 h. Further heat treatments were carried out at 1000 °C for 12 h and 1100 °C for 72 h with intermediate grinding after each 24 h. The powders were pelletized in the form of circular discs and sintered in air at a

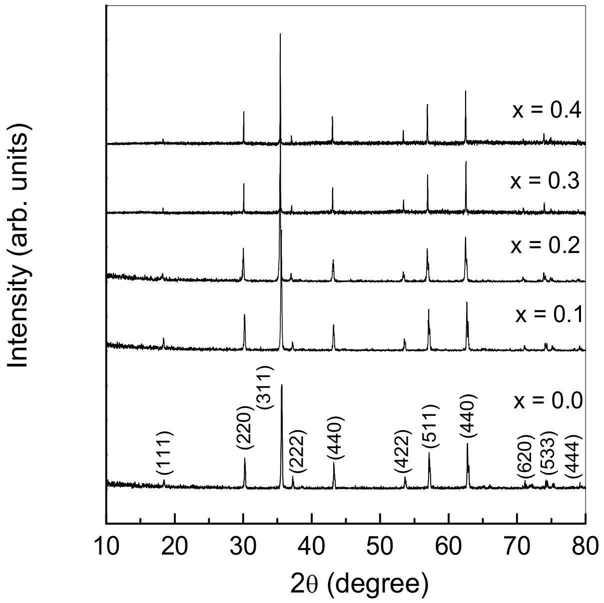

Figure 4.1: X-ray diffraction patterns for different compositions in the $Co_{1-x}Mn_xFe_2O_4$ series.

maximum temperature of 1450 °C for 10 minutes. These sintered pellets were used for magnetostriction measurements. Similar procedures were followed for the synthesis of the compositions in the series $Co_{1.2-x}Mn_xFe_{1.8}O_4$ (CMFO) and $Co_{1.2}Fe_{1.8-x}Mn_xO_4$ (CFMO) where $(0.0 \leq x \leq 0.4)$.

4.3 $Co_{1-x}Mn_xFe_2O_4$

4.3.1 Powder XRD Analysis

The XRD patterns of the compositions in the CMF series are shown in figure 4.1. All the XRD patterns show the reflections from the spinel phase only indicating the formation of the respective compositions. The variation of the cubic lattice parameter as a function of Mn concentration is plotted in figure 4.2. The cubic lattice parameter increases almost linearly with increasing Mn content. This is expected because $MnFe_2O_4$ has a lattice constant of 8.50 Å as compared to 8.38 Å for $CoFe_2O_4$ due to the larger ionic radius of Mn^{2+} (0.83 Å) ions when compared to that of Co^{2+} (0.745 Å) [11, 18]. A continuous variation in the unit cell parameter is observed. Similar variation of lattice parameter

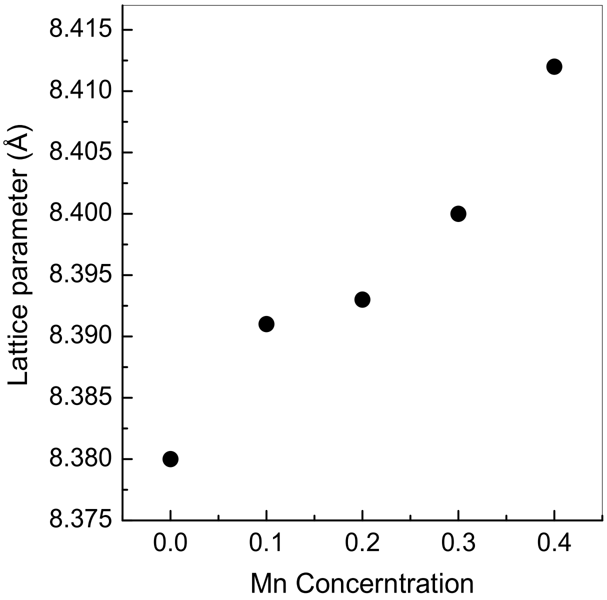

Figure 4.2: The variation of the unit cell parameter with Mn concentration in the $Co_{1-x}Mn_xFe_2O_4$ (CMF) series.

is reported by Zhou *et al.* for the thin film samples of $CoFe_{2-x}Mn_xO_4$ [19]. The lattice parameters calculated using the PCW refinement program are listed in Table 4.2.

4.3.2 TMA Analysis

The sintering behavior of some of the compositions in the CMF series is shown in figure 4.3. The shrinkage starts above 1000 °C and a slight drop in the onset of sintering is observed with increasing Mn content. However, sintering is not completed even at a temperature as high as 1350 °C. All the samples show a liner shrinkage of ∼10% at a maximum sintering temperature of 1350 °C. Since the sintering is not completed at this temperature as evidenced from the TMA studies, the compositions in the present study are sintered at a higher temperature of 1450 °C in order to have a sintered material with relatively higher density. Also, sintering at 1450 °C was performed for a direct comparison of the results reported by Paulsen *et al.* [13] from the studies on the $CoFe_{2-x}Mn_xO_4$ series.

Table 4.2: Cubic unit cell parameter for the compositions in the $Co_{1-x}Mn_xFe_2O_4$ (CMF) series.

Mn content	a (Å)
$x = 0.0$	8.380
$x = 0.1$	8.391
$x = 0.2$	8.393
$x = 0.3$	8.400
$x = 0.4$	8.412

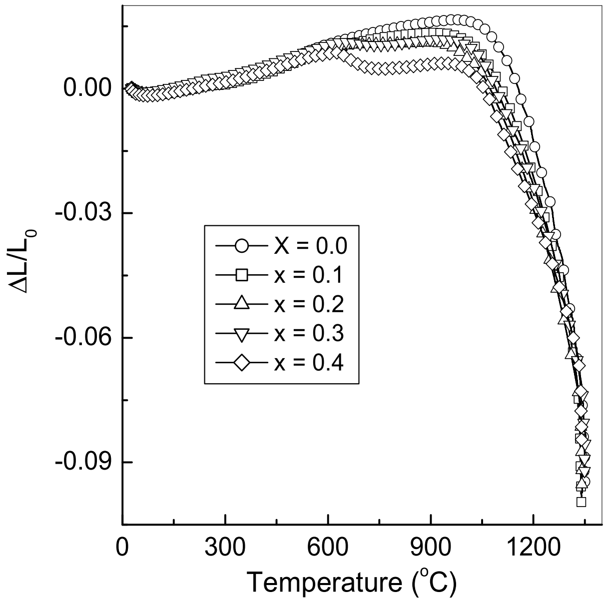

Figure 4.3: Sintering behavior of the compositions in the $Co_{1-x}Mn_xFe_2O_4$ (CMF) series.

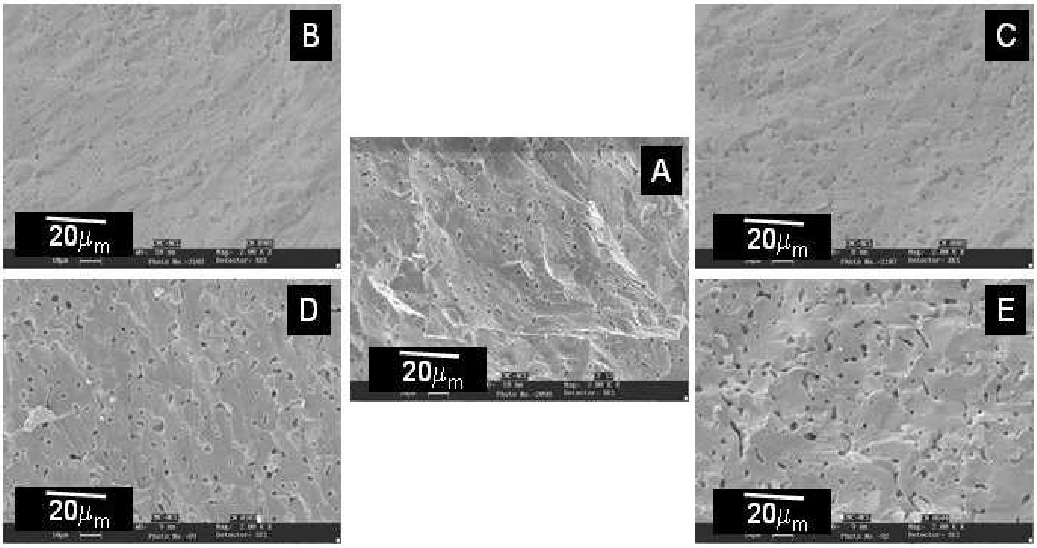

Figure 4.4: Scanning electron micrographs for different compositions in the $Co_{1-x}Mn_xFe_2O_4$ (CMF) series. (A) $CoFe_2O_4$ (B) $Co_{0.9}Mn_{0.1}Fe_2O_4$ (C) $Co_{0.8}Mn_{0.2}Fe_2O_4$ (D) $Co_{0.7}Mn_{0.3}Fe_2O_4$ and (E) $Co_{0.6}Mn_{0.4}Fe_2O_4$.

4.3.3 Microstructural Analysis

Figure 4.4 shows the scanning electron micrographs of different compositions sintered at 1450 °C. As can be seen from the images, a very dense microstructure is observed for all the compositions. The densities of the sintered compacts are found to be around 90% of the theoretical X-ray density of the corresponding compositions. However, for the composition containing 10% Mn, somewhat directional growth of grains is observed as compared with other samples. Such a grain growth can lead to the pinning of the domain walls weakening the response of the magnetic domains to align with the applied magnetic field thereby affecting the magnetostrictive response.

4.3.4 Magnetic Measurements

The magnetization curves of the compositions in the CMF series, sintered at 1450 °C, as a function of magnetic field are shown in figure 4.5. The inset shows the M-H curves at low magnetic field strengths indicating the changes in the coercivity on Mn substitution. The

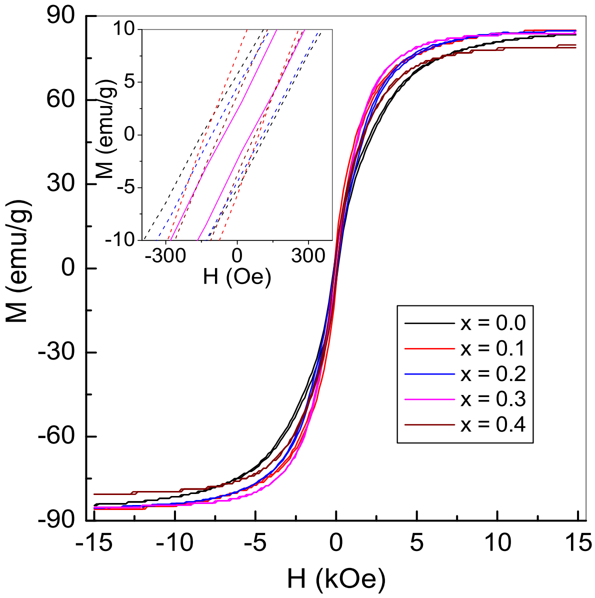

Figure 4.5: Magnetization as a function of magnetic field for the compositions in the $Co_{1-x}Mn_xFe_2O_4$ (CMF) series.

temperature dependence of magnetization recorded using a low magnetic field strength of 50 Oe, is shown in figure 4.6. The Curie temperature is found to decrease from 520 °C for $x = 0.0$ to 416 °C for $x = 0.4$.

The variations of the Curie temperature, magnetization at 7 kOe and 15 kOe as well as the coercivity as a function of Mn concentration are shown in figure 4.7. The saturation magnetization at 7 kOe and Curie temperature, reported previously by Paulsen *et al.* [13] for different compositions in $CoFe_{2-x}Mn_xO_4$ are also shown in the figure for comparison. The magnetization at 15 kOe, which is almost saturated, is increased with increasing Mn content from 83 emu/g for $x = 0.0$ to 85 emu/g for $x = 0.1$. Magnetization remains almost constant till $x = 0.3$ and then decreases to 80 emu/g for $x = 0.4$. However, at lower field strengths, the magnetization continuously increases up to $x = 0.3$ and then drops to a smaller value, indicating a decrease in the magnetic anisotropy with increasing Mn content. The coercivity is found to decrease almost linearly with increasing Mn content, again indicating a decrease in the anisotropy of the material. However, for the composition with $x = 0.3$, unexpectedly lower coercivity is observed. This is probably due to some peculiar changes in the cation distribution in the octahedral and tetrahedral sites near

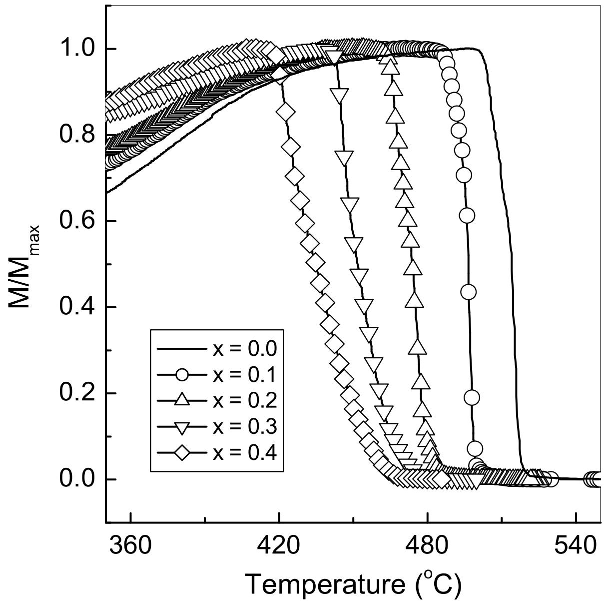

Figure 4.6: Temperature variation of magnetization for the compositions in the $Co_{1-x}Mn_xFe_2O_4$ (CMF) series.

this composition.

For $MnFe_2O_4$ ($x = 1$), nearly 20% of Mn is distributed in the octahedral sites as Mn^{3+} and therefore equivalent amount of Fe will be present as Fe^{2+} for charge compensation [20]. For $Co_{1-x}Mn_xFe_2O_4$, an increase in the magnetization is expected after substitution of Mn for Co, if Co^{2+} is replaced by Mn^{2+}, since Mn^{2+} has a larger magnetic moment of 5 μ_B as compared to 3 μ_B for Co^{2+}. However, if Mn is substituted initially as Mn^{2+} (5 μ_B) at lower Mn concentrations and as Mn^{2+} as well as Mn^{3+} at larger concentrations, then the magnetization is expected to level off at certain concentrations of Mn and then decreases because of the lower magnetic moment of Mn^{3+} (4 μ_B) and the conversion of equivalent amounts of Fe^{3+} (5 μ_B) to Fe^{2+} (4 μ_B). As can be seen from figure 4.7, T_C drops almost linearly with increasing Mn content. The decrease in the T_C is not as large as that observed in the case of Mn substitution for Fe as reported by Paulsen *et al.* [13]. Linear least squares fit of the data of $Co_{1-x}Mn_xFe_2O_4$ series gives the T_C as 314 °C for $x = 1$ and this is comparable to the Curie temperature of $MnFe_2O_4$ (~300 °C). Hence, the assumption of small amounts of Mn^{3+} and Fe^{2+} at larger Mn concentrations as in $MnFe_2O_4$ is likely to be correct. It is reported that the Curie temperature plays

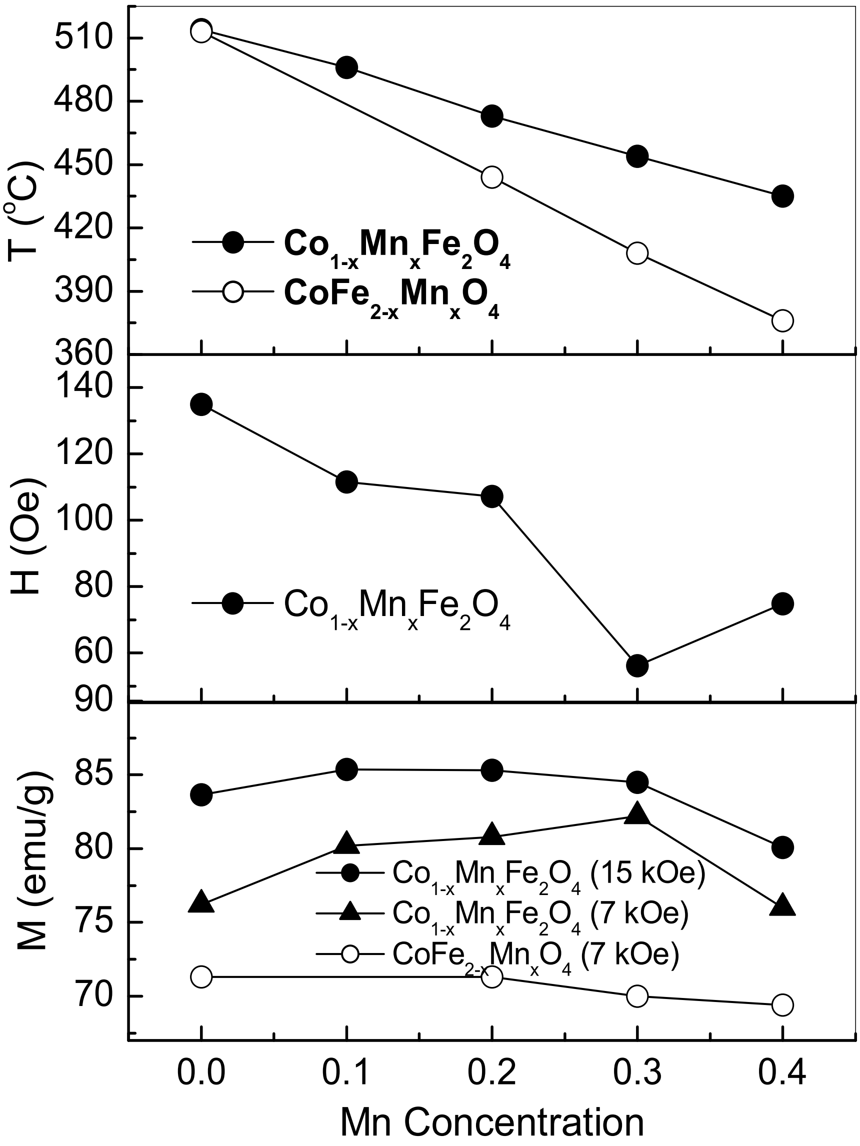

Figure 4.7: Variation M_s, H_c, and T_C as a function of Mn concentration in the $Co_{1-x}Mn_xFe_2O_4$ (CMF) series. The values shown for $CoFe_{2-x}Mn_xO_4$ are from reference [13].

Table 4.3: Variation of coercivity, magnetization and Curie temperature of the sintered compositions in the $Co_{1-x}Mn_xFe_2O_4$ (CMF) series.

Mn content	H_c (Oe)	M_s (emu/g)	T_C (°C)
$x = 0.0$	135	83.6	514
$x = 0.1$	111	85.3	496
$x = 0.2$	107	85.3	473
$x = 0.3$	56	84.5	454
$x = 0.4$	74	80.0	435

a key role in determining the temperature dependence of magnetomechanical effects and in reducing the magnetomechanical hysteresis [13]. This implies the need to modify the Curie temperature by still maintaining a sufficiently high value of magnetostriction. The values of coercivity, magnetization and Curie temperature for different compositions in the CMF series are summarized in table 4.3.

4.3.5 Magnetostriction Studies

Figure 4.8 and figure 4.9 show the variation of the magnetostriction as a function of magnetic field, measured at room temperature, along the parallel ($\lambda_{\parallel}$) and perpendicular ($\lambda_{\perp}$) directions to the applied magnetic field, respectively. The magnitude of $\lambda_{\parallel}$ is maximum for $x = 0.0$ with a maximum strain of 138 ppm. This maximum value of magnetostriction (λ_{max}) is relatively lower than that reported recently for polycrystalline cobalt ferrite samples (210 ppm) [21, 22]. This difference is likely to be due to the difference in the processing conditions and the associated changes in the distribution of the ions in the spinel lattice as well as the changes in the microstructure. Harrison *et al.* have shown that the cation distribution in cobalt ferrite is very sensitive to the heating and cooling rates [23]. With increasing manganese content the strain in the parallel direction decreases, except for 30% substitution where it is found to be larger than that for 10% and 20% substitution. On the other hand, along the perpendicular direction, the maximum strain is enhanced from 106 ppm to 117 ppm for 10% substitution and $\lambda_{\perp}$ then decreases continuously with increasing Mn content. For other compositions in the CMF series, the magnitude of maximum magnetostriction ($\lambda_{\perp}$) decreases to 97 ppm, 55 ppm and 58 ppm

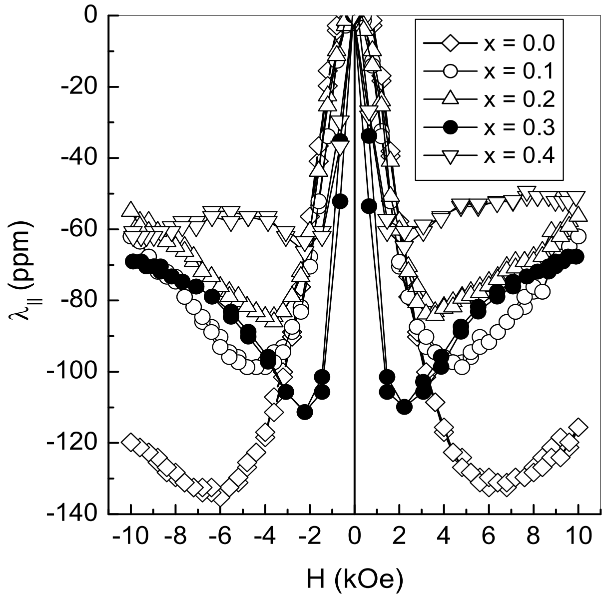

Figure 4.8: Magnetostriction curves recorded in the parallel direction ($\lambda_{\parallel}$) as a function of magnetic field for different compositions in the $Co_{1-x}Mn_xFe_2O_4$ (CMF) series.

for $x = 0.2$, 0.3 and 0.4, respectively. Since the 30% substituted sample shows unusual behavior, the measurements were repeated on another sample sintered separately, and it was found that the peculiar behavior is reproducible. As the densities of all the samples were found to be almost identical (∼90%), the changes in the value of magnetostriction is not likely to be due to any variation of porosity.

Apart from the changes in the peak values of magnetostriction (λ_{max}), there are large changes in the magnetostriction at low fields as well as the magnetic field at which maximum magnetostriction is observed, along both directions. For $x < 0.3$, there is an initial lag in the magnetostriction with increasing field where as for $x = 0.3$ and 0.4, the magnetostriction sharply rises at low fields. Figure 4.10 shows a comparison of λ_{max} and λ at different low fields, as a function of x. Though λ_{max} decreases with increasing Mn concentration, unusually large value is obtained for $x = 0.3$ along the parallel direction. The magnetostriction for $x = 0.3$ is 3 to 6 times larger at low field strengths when compared to the value for the unsubstituted sample.

The changes in the volume (ω) and anisotropic magnetostriction (λ_t), as a function of Mn concentration, are plotted in figure 4.11. The magnitude of volume magnetostriction is

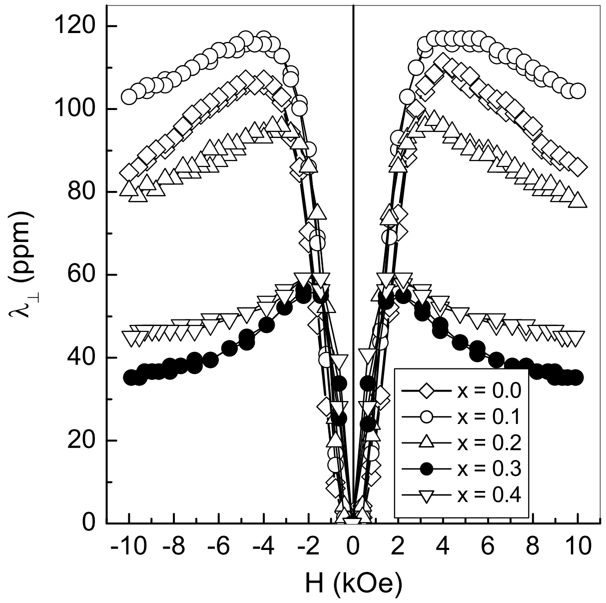

Figure 4.9: Magnetostriction curves recorded in the perpendicular direction ($\lambda_{\perp}$) as a function of magnetic field for different compositions in the $Co_{1-x}Mn_xFe_2O_4$ (CMF) series.

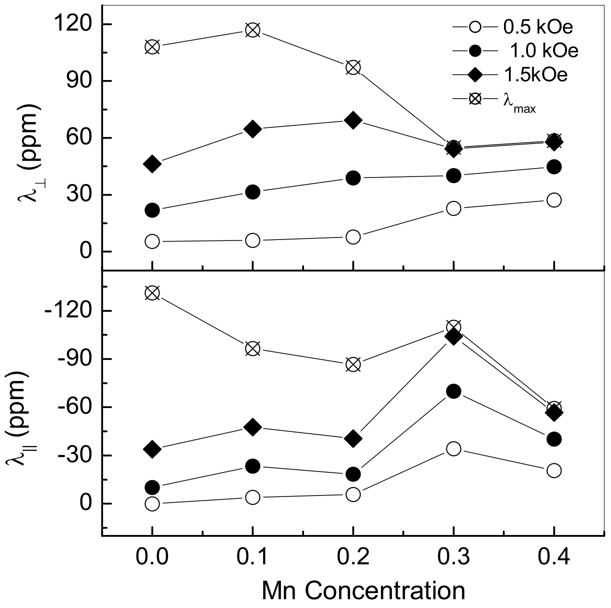

Figure 4.10: Variation of λ at different low fields and λ_{max} as a function of Mn concentration in $Co_{1-x}Mn_xFe_2O_4$.

found to be maximum for the composition containing 10% Mn. However, the anisotropic magnetostriction shows a continuous decrease with increasing Mn content. Figure 4.12 shows the variation of the slope of the magnetostriction curve (dλ/dH), for both parallel and perpendicular measurements, and the field required to attain the maximum value of magnetostriction (H_{max}). The slopes of the magnetostriction curves show a strong dependence on the Mn content. For $x = 0.0$, the maximum of magnetostriction in the parallel direction is observed at a magnetic field strength of 5.9 kOe, which is shifted to a lower magnetic field of 2.2 kOe for the compositions containing 30% and 40% manganese. For the composition with 10% Mn content, the maximum of magnetostriction is observed at 4.8 kOe. For the measurements carried out in the perpendicular direction also, a similar lowering of the magnetic field required to achieve the maximum value of the magnetostriction is observed. In this direction the magnetic fields required are found to be between 4 and 2.2 kOe. Along the parallel and perpendicular directions, H_m is reduced to almost 33% and 50%, respectively, for $x = 0.3$ and 0.4 when compared to the values for $x = 0$. The strain derivative or the slope of the magnetostriction curve dλ/dH is found to be almost double for $x = 0.3$. dλ/dH is a measure of the performance of the material and is related to the efficiency of energy conversion of the material [24]. For applications in stress sensing, the slope of the magnetostriction curve is very important. A high value of magnetostriction at low magnetic field strength is very essential for such applications.

A comparison of the observed magnetostrictive strain with the microstructure (see figure 4.4) shows that for the composition with $x = 0.1$, a directed grain growth leads to an enhanced magnetostriction in the perpendicular direction. The composition with $x = 0.3$, shows the presence of smaller uniform sized grains as compared to other compositions, and this could be the reason for the larger magnetostriction and enhanced slope of the magnetostriction curve.

The different parameters such as magnetostrictive strains in the parallel ($\lambda_{\parallel}$) and perpendicular ($\lambda_{\perp}$) directions, maximum magnetic field (H_{max}) required to achieve the maximum magnetostriction, anisotropic magnetostriction and volume magnetostriction for different compositions are summarized in Table 4.4. Mn substitution for Co in $CoFe_2O_4$ is found to be more effective in tuning the magnetostrictive behavior of polycrystalline cobalt ferrite. The enhanced slope of magnetostriction curve for 30% Mn content, higher

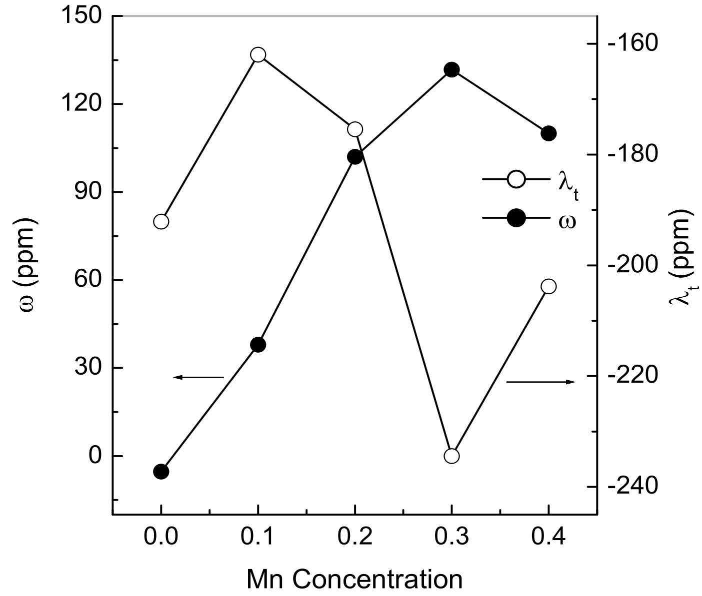

Figure 4.11: Variation of volume (ω) and anisotropic strain (λ_t) for the compositions in the $Co_{1-x}Mn_xFe_2O_4$ (CMF) series.

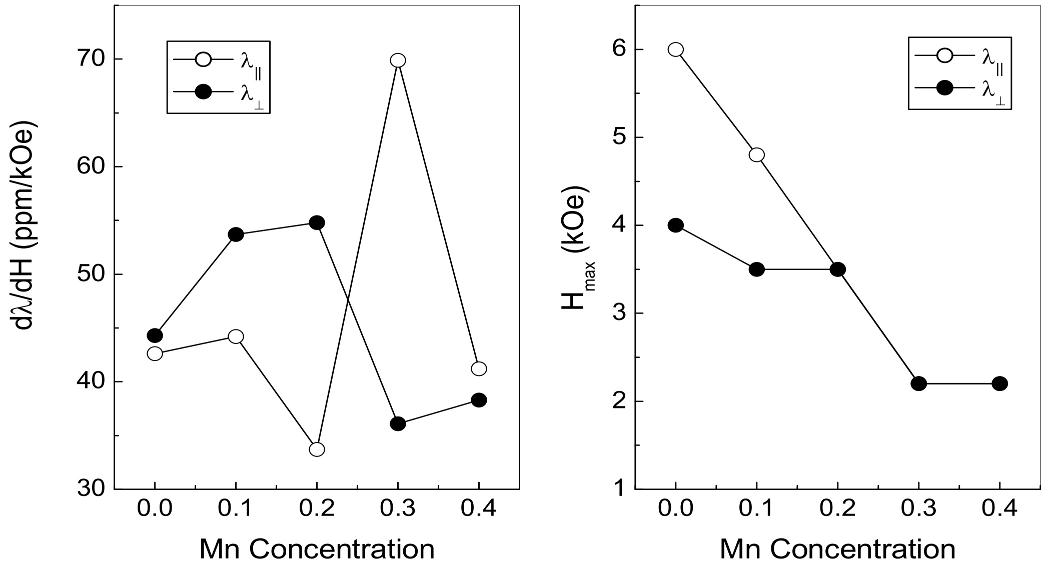

Figure 4.12: Variation of slope of the magnetostriction curve and H_{max} for the measurements in the parallel (open symbols) and perpendicular (closed symbols) directions for the compositions in the $Co_{1-x}Mn_xFe_2O_4$ (CMF) series.

Table 4.4: Summary of $\lambda_{\parallel}$, $\lambda_{\perp}$, H_{max}, dλ/dH, λ_t and ω for different compositions in the $Co_{1-x}Mn_xFe_2O_4$ (CMF) series.

Mn Content	$\lambda_{\parallel}$ (ppm)	$\lambda_{\perp}$ (ppm)	$H_{max}(\parallel)$ (kOe)	$H_{max}(\perp)$ (kOe)	d$\lambda/dH_{\parallel}$ (ppm/kOe)	d$\lambda/dH_{\perp}$ (ppm/kOe)	λ_t (ppm)	ω (ppm)
$x = 0.0$	-138	108	6.0	4.0	42.6	44.3	-237.2	79.9
$x = 0.1$	-97	117	4.8	3.5	44.2	53.7	-214.3	136.7
$x = 0.2$	-87	97	3.5	3.5	33.7	54.8	-180.4	111.3
$x = 0.3$	-107	55	2.2	2.2	69.9	36.1	-164.7	0.0
$x = 0.4$	-64	58	2.2	2.2	41.2	38.3	-176.2	57.8

value of strain in the perpendicular direction for 10% Mn content, and a lowering of the magnetic field required to achieve the maximum strain are the key features of the partial substitution of Co by Mn. The studies showed that the microstructure also plays a crucial role in determining the magnetostrictive properties.

4.4 Studies on Mn Substituted $Co_{1.2}Fe_{1.8}O_4$

4.4.1 Powder XRD Analysis

The X-ray diffraction patterns of the compositions in the $Co_{1.2-x}Mn_xFe_{1.8}O_4$ (CMFO) and $Co_{1.2}Fe_{1.8-x}Mn_xO_4$ (CFMO) series are shown in figure 4.13. All the reflections in the XRD patterns correspond to the spinel structure and no additional reflections are observed indicating the phase purity of the compositions. For the compositions in the CFMO series, only a slight change in the unit cell parameter is observed. Similar results were obtained by Zhou *et al.* [19] in the case of thin film samples of $CoFe_{2-x}Mn_xO_4$ prepared by sol-gel process. It is expected that when Fe^{3+} is replaced by Mn^{3+}, the lattice parameter will not be varied much because of the identical ionic radii of both these ions (0.645 Å), for octahedral coordination. The smaller increase in the lattice parameter is likely to be due to some variation in the distribution of the ions in the tetrahedral and octahedral sites. On the other hand, larger increase in the lattice parameter is observed when Co is replaced by Mn in the CMFO series. This can be attributed to the larger ionic

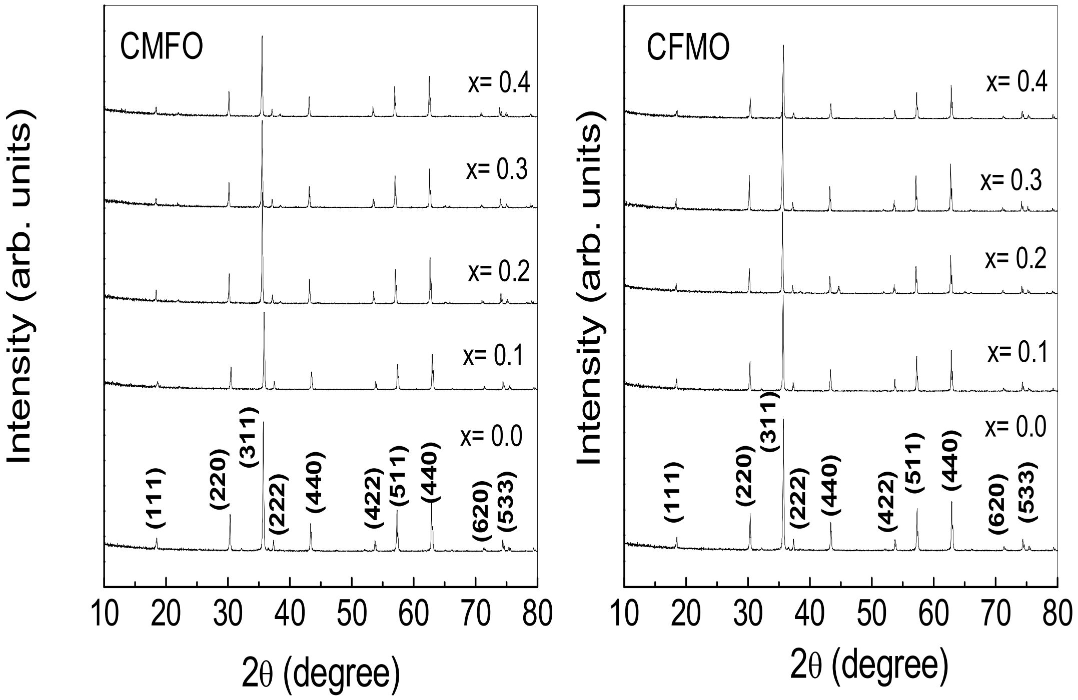

Figure 4.13: Powder X-ray diffraction patterns for different compositions in the $Co_{1.2-x}Mn_xFe_{1.8}O_4$ (CMFO) and $Co_{1.2}Fe_{1.8-x}Mn_xO_4$ (CFMO) series.

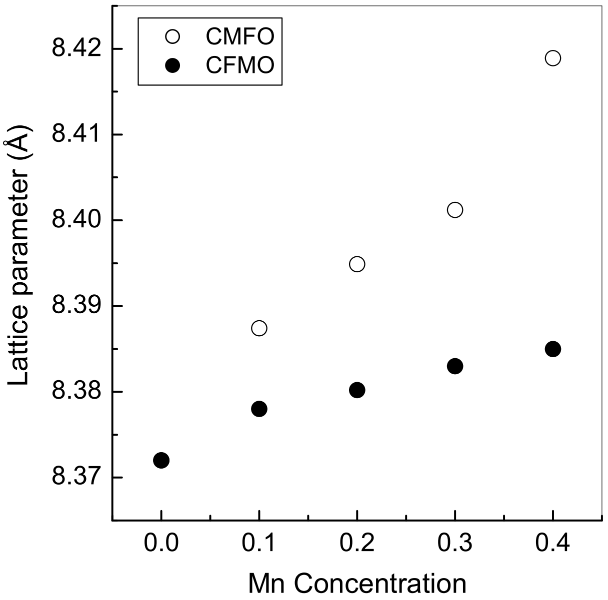

Figure 4.14: Variation of the cubic lattice parameter with Mn content for different compositions in the $Co_{1.2-x}Mn_xFe_{1.8}O_4$ (CMFO) and $Co_{1.2}Fe_{1.8-x}Mn_xO_4$ (CFMO) series.

size of Mn^{2+} (0.83 Å) as compared to Co^{2+} (0.745 Å) in the tetrahedral coordination. The variation of the lattice parameter for the compositions in the CMFO and CFMO series is plotted in figure 4.14. Table 4.5 shows the calculated lattice parameters for all the compositions.

4.4.2 TMA Analysis

The sintering behavior of $CoFe_2O_4$, $Co_{1.2}Fe_{1.8}O_4$ and $Co_{1.1}Mn_{0.1}Fe1.8O_4$ is compared in figure 4.15. Both the compositions show almost identical sintering behavior and shrinkage, as that of $CoFe_2O_4$ except for the fact that the Mn substituted composition shows a slight decrease in the onset temperature for sintering. Sintering is not completed at 1350 °C, the maximum temperature in the TMA analysis.

4.4.3 Microstructural Analysis

The SEM micrographs of the $x = 0$, 0.1, and 0.3 compositions for both the CFMO and the CMFO series are shown in figure 4.16. In the case of CMFO, the microstructure is

Table 4.5: Cubic unit cell parameters for different compositions in the $Co_{1.2-x}Mn_xFe_{1.8}O_4$ (CMFO)and $Co_{1.2}Fe_{1.8-x}Mn_xO_4$ (CFMO) series with increasing Mn content.

Mn content	a (Å) (CMFO)	a (Å)(CFMO)
$x = 0.0$	8.372	8.372
$x = 0.1$	8.387	8.378
$x = 0.2$	8.394	8.380
$x = 0.3$	8.401	8.383
$x = 0.3$	8.418	8.385

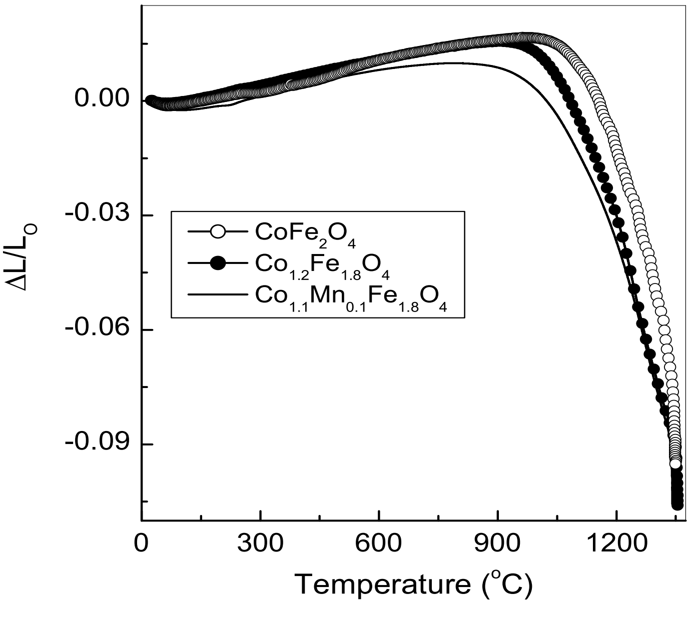

Figure 4.15: Sintering behavior of $Co_{1.2}Fe_{1.8}O_4$, and $Co_{1.1}Mn_{0.1}$Fe1.8O_4 compared with $CoFe_2O_4$.

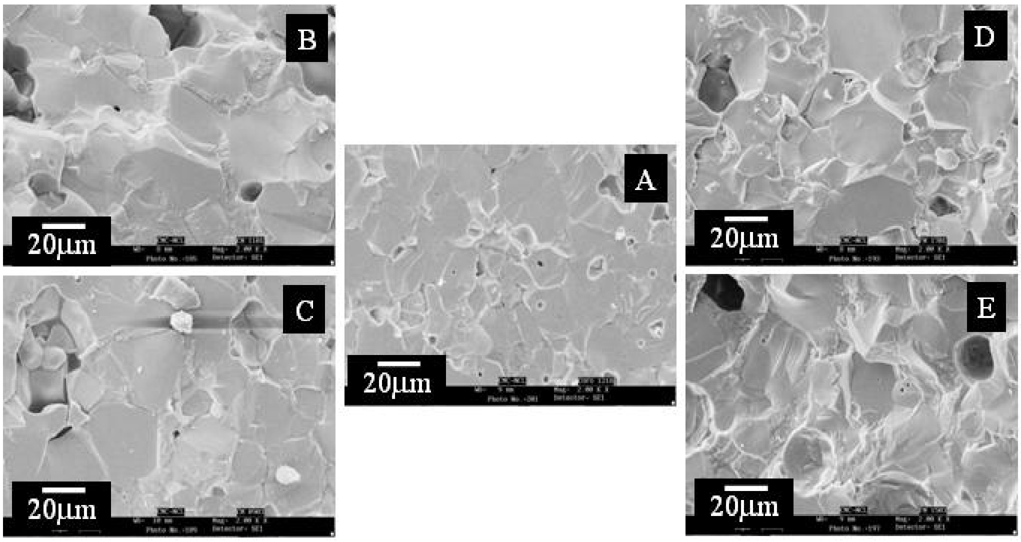

Figure 4.16: Comparison of the SEM micrographs of (A) $Co_{1.2}Fe_{1.8}O_4$, (B) $Co_{1.1}Mn_{0.1}Fe_{1.8}O_4$, (C) $Co_{0.9}Mn_{0.3}Fe_{1.8}O_4$, (D) $Co_{1.2}Fe_{1.7}Mn_{0.1}O_4$, and (E) $Co_{1.2}Fe_{1.5}Mn_{0.3}O_4$.

found to be uniform along with the presence of large grains. The porosity increases with increasing Mn content. The overall microstructure is found to be much more uniform as compared to that of the parent compound. However, in the case of CFMO, discontinuous grain growth and presence of large pores is observed with increasing Mn content.

4.4.4 Magnetic Measurements

The magnetization measurements were carried out at room temperature up to a maximum magnetic field strength of 15 kOe for the powder samples as well as for the sintered pellets. Figure 4.17 and Figure 4.18 show the variation of magnetization as a function of magnetic field for different compositions in the CMFO and CFMO series.

The variations of saturation magnetization and coercivity for the powders and sintered samples are shown in figure 4.19. In the case of the powder samples, the saturation magnetization value of 64 emu/g is observed for the parent compound $Co_{1.2}Fe_{1.8}O_4$. All the compositions show magnetic saturation above 5 kOe. For the compositions in the CMFO series, the magnetization increases with increasing Mn content up to $x = 0.2$ and

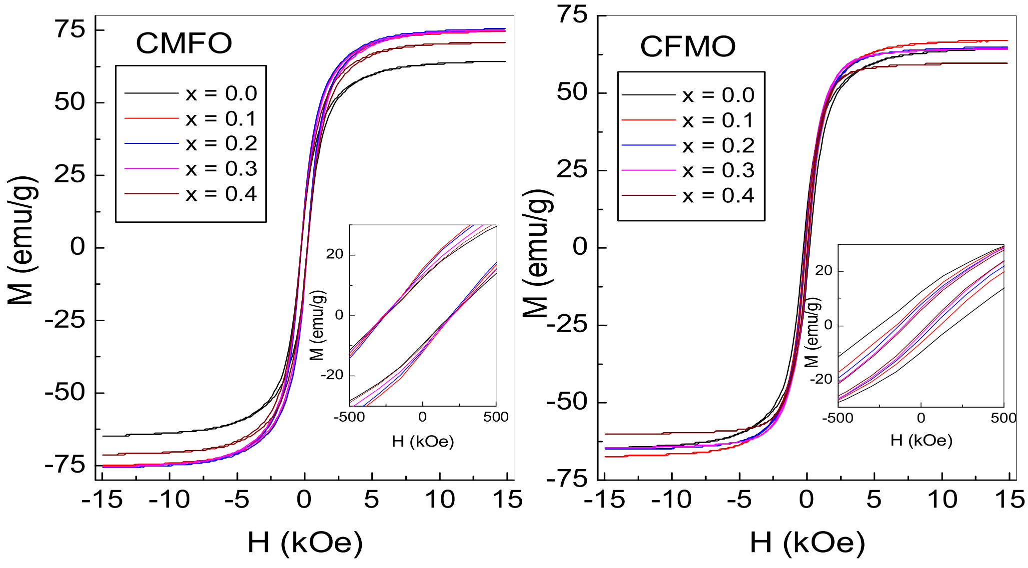

Figure 4.17: Room temperature magnetization curves for the powder samples in the $Co_{1.2-x}Mn_xFe_{1.8}O_4$ (CMFO) and $Co_{1.2}Fe_{1.8-x}Mn_xO_4$ (CFMO) series.

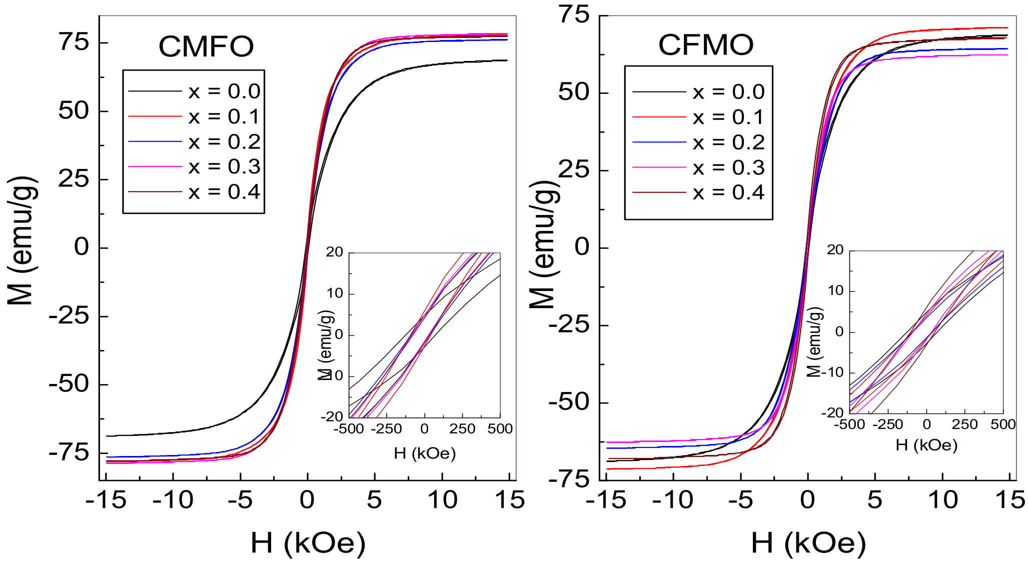

Figure 4.18: Room temperature magnetization curves for the sintered samples in the $Co_{1.2-x}Mn_xFe_{1.8}O_4$ (CMFO) and $Co_{1.2}Fe_{1.8-x}Mn_xO_4$ (CFMO) series.

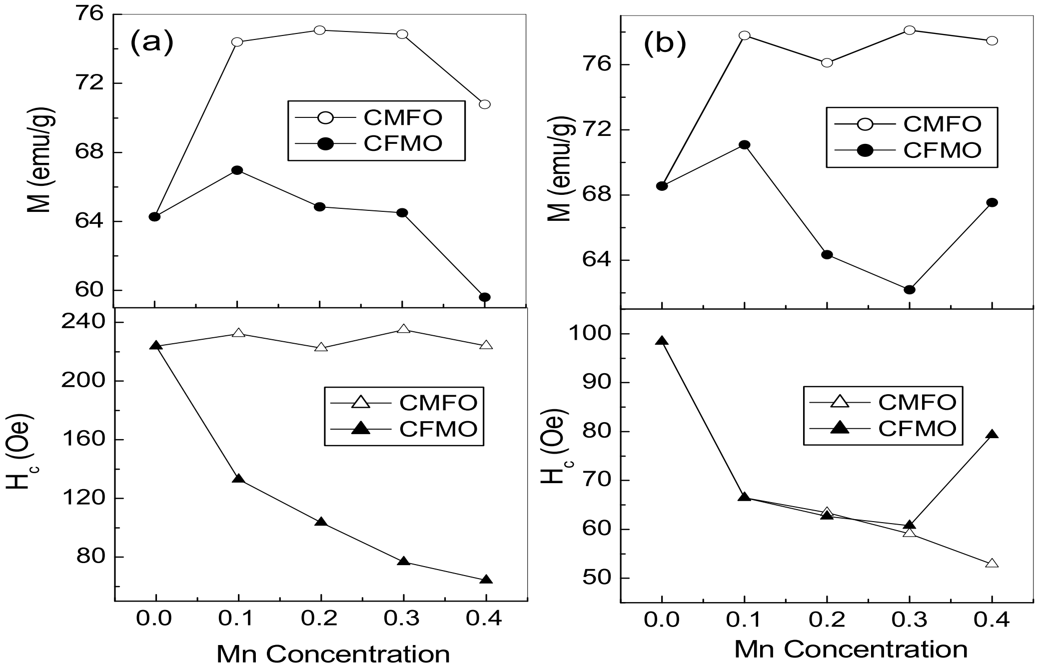

Figure 4.19: Variation of magnetization and coercivity for the powder (a) and sintered (b) samples in the $Co_{1.2-x}Mn_xFe_{1.8}O_4$ (CMFO) and $Co_{1.2}Fe_{1.8-x}Mn_xO_4$ (CFMO) series with increasing Mn concentration.

then decreases to a small value. A maximum magnetization of 75 emu/g is obtained for the composition with 20% Mn. However, the magnetization increases only a little when Mn is substituted for Fe. It remains almost constant up to 30% Mn substitution and then decreases to 60 emu/g for $x = 0.4$. Similarly the coercivities of the powder samples also exhibited a marked dependence on Mn content. When Mn is substituted for Co the coercivity remains almost constant for all the compositions and is close to 225 Oe. However, in the case of Mn substitution for Fe, the coercivity decreases continuously.

The sintered samples show almost a similar trend as in case of the powder samples. The magnetization is found to be higher for CMFO series compositions and slightly higher value is observed as compared to the powder samples. For the substitution of Co by Mn, there is an initial increase in the saturation magnetization from ∼68 emu/g for $x = 0.0$ to ∼79 emu/g for $x = 0.1$ and then the magnetization remains almost constant for larger values of x. For the CFMO series, magnetization is increased to 71 emu/g for 10% Mn

Table 4.6: Summary of magnetization and coercivity for the powder and sintered samples in the $Co_{1.2-x}Mn_xFe_{1.8}O_4$ (CMFO) and $Co_{1.2}Fe_{1.8-x}Mn_xO_4$ (CFMO) series.

Mn Content	CMFO				CFMO			
	Powder		Pellet		Powder		Pellet	
	H_c (Oe)	M_s (emu/g)	H_c (Oe)	M_s (emu/g)	H_c (Oe)	M_s (emu/g)	H_c (Oe)	M_s (emu/g)
$x = 0.0$	223	64.2	98	68.5	223	64.2	98	68.5
$x = 0.1$	232	74.4	66	77.8	133	66.9	66	71.8
$x = 0.2$	222	75.0	63	76.1	104	64.8	63	64.3
$x = 0.3$	235	74.8	59	78.1	77	64.5	61	62.2
$x = 0.4$	224	70.7	53	77.4	64	59.6	79	67.5

content, which then decreases up to 30% Mn content and again increases for $x = 0.4$. The coercivity of the sintered samples, in the case of CFMO series compositions, shows a decrease with increasing Mn content up to 30%, and then increases for 40% Mn content. However, a continuous decrease in coercivity is seen for the sintered samples in the CMFO series.

The substitution of Fe^{3+} by Mn^{3+} is expected to decrease the saturation magnetization assuming that the substituted Mn^{3+} ions preferentially occupies the octahedral B site in the AB_2O_4 spinel structure. This is due to the decrease in the magnetic moment from 5 μ_B for Fe^{3+} to 4 μ_B for Mn^{3+}. On the other hand, substitution of Co^{2+} by Mn^{2+} should enhance the saturation magnetization since the magnetic moments for Co^{2+} and Mn^{2+} are $3\mu_B$ and $5\mu_B$, respectively. The initial increase in the magnetization for $x = 0.1$ and a constant value thereafter, for $Co_{1.2-x}Mn_xFe_{1.8}O_4$, indicate that initially, at lower concentrations, the Mn^{2+} ions are substituted in the B site of the spinel lattice and at higher concentrations, the rest of the Mn^{2+} ions are distributed in the A site. The coercivity is decreased irrespective of whether Co or Fe is replaced by Mn. The variation in the coercivity of the CFMO series is similar to that observed in the case of $CoFe_2O_4$. The changes in the coercivity and magnetization are likely to affect the magnetostrictive responses of the Mn substituted compounds.

The temperature dependence of magnetization recorded in a magnetic field of 50 Oe are

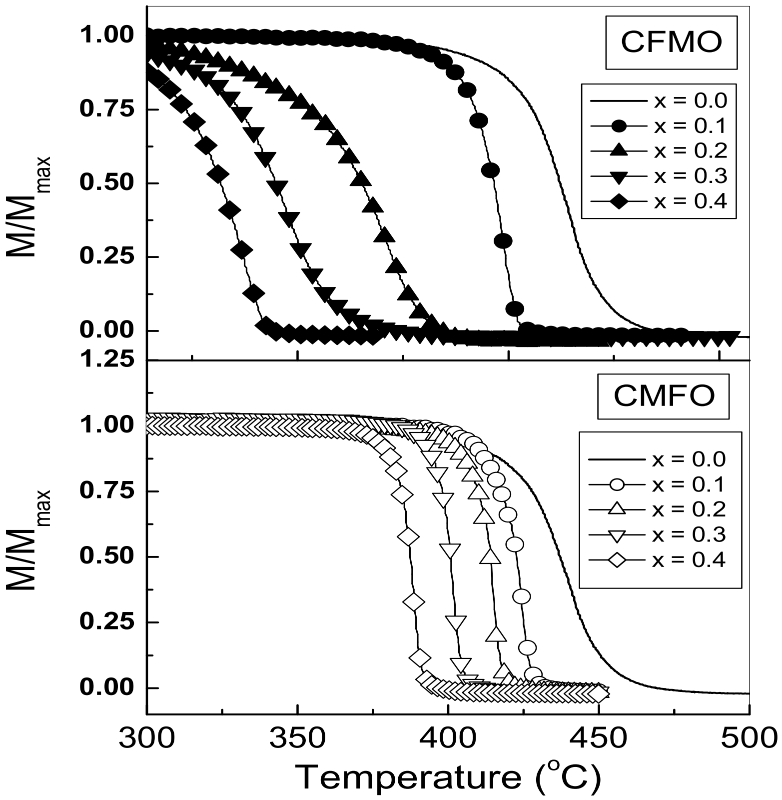

Figure 4.20: Temperature dependence of magnetization for different compositions in the $Co_{1.2-x}Mn_xFe_{1.8}O_4$ (CMFO) and $Co_{1.2}Fe_{1.8-x}Mn_xO_4$ (CFMO) series.

shown in figure 4.20. The parent composition $Co_{1.2}Fe_{1.8}O_4$ shows a Curie temperature of 440 °C. A continuous decrease in the Curie temperature with increasing Mn concentration is observed for both the series. However, the T_C drops rapidly when Mn is substituted for Fe as compared to Mn substitution for Co. A Similar decrease in the Curie temperature has been observed in the case of Mn substitution for Fe in $CoFe_2O_4$ as reported by Paulsen *et al.* [13].

The variation of T_C with increasing Mn content is shown in figure 4.21. This observed difference in the Curie temperatures of the samples in both these series could be due to a different cation distributions in the octahedral and the tetrahedral sites of the spinel lattice. Mn^{2+}, when substituted for Co^{2+}, will have a stronger tetrahedral site preference as in the case of $MnFe_2O_4$, whereas substitution for Fe^{3+} will lead to a octahedral site occupancy of the Mn^{3+} ions, as in case of $CoMn_2O_4$, where Mn^{3+} has strong preference

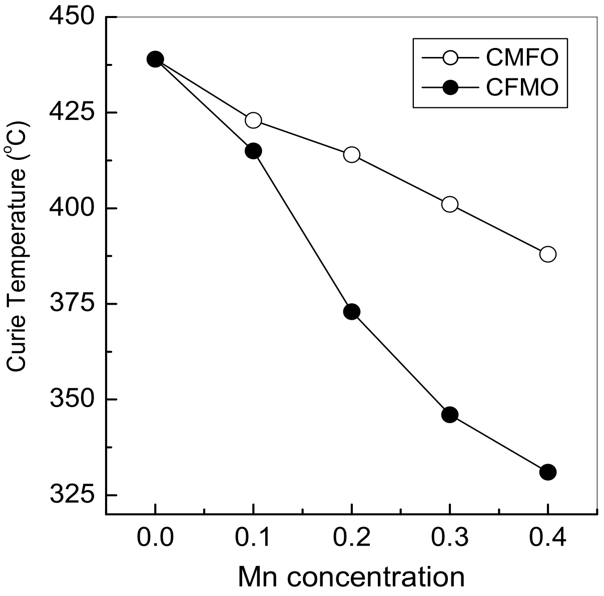

Figure 4.21: Variation of Curie temperature with Mn concentration for the compositions in the $Co_{1.2-x}Mn_xFe_{1.8}O_4$ (CMFO) and $Co_{1.2}Fe_{1.8-x}Mn_xO_4$ (CFMO) series.

for octahedral site occupancy. Such a difference in the cation distribution can affect the strength of the A-O-B magnetic exchange interactions in the spinel lattice thereby leading to different Curie temperatures. The Curie temperature for $CoMn_2O_4$, is -183 °C [19,25], as compared to 300 °C for $MnFe_2O_4$ [26]. Therefore when Mn is substituted for Co, the T_C is expected to decrease but not as rapidly as when Mn is substituted for Fe. Similarly, a larger decrease in the T_C has been observed when Mn is substituted for Fe [13], as compared to the substitution of Mn for Co as has been shown in figure 4.7. This is mainly because of the decrease in the A-O-B exchange interactions when Fe is replaced by Mn.

4.4.5 Magnetostriction Studies

The magnetostriction curves recorded for different compositions in the CMFO and CFMO series in the parallel and perpendicular directions are shown in figure 4.22 and figure 4.23, respectively. As can be seen from the figures, the magnetostriction observed for the composition with $x = 0.0$, *i.e.* $Co_{1.2}Fe_{1.8}O_4$, is around 90 ppm. This value is relatively

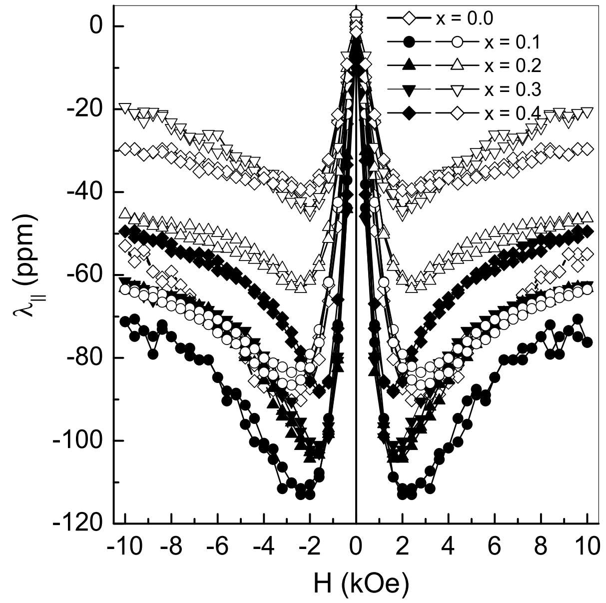

Figure 4.22: Magnetostriction measured parallel to the field direction, as a function of field, for the different compositions in the $Co_{1.2-x}Mn_xFe_{1.8}O_4$ (filled symbols) and the $Co_{1.2}Fe_{1.8-x}Mn_xO_4$ (open symbols
series

smaller than the value obtained (113 ppm) for this composition in the preliminary studies (see figure 3.4). This is possibly due to the differences in the processing conditions and the associated changes in the microstructure and cation distribution. In the preliminary studies, the sample was sintered at 1100 °C for 8 h whereas here the samples are sintered at 1450 °C for 4 h. For comparison with the studies on Mn substituted compositions, the un-substituted compound was also synthesized again along with the other compositions.

For the compositions in the CMFO series, the magnetostriction recorded in the parallel direction ($\lambda_{||}$) is found to be higher for the compositions containing Mn. Maximum value is obtained for the sample containing 10% Mn, with a maximum magnetostrictive strain of 112 ppm. For 20% and 30% Mn containing compositions the magnitudes of the magnetostrictive strains are 104 and 101 ppm, respectively, which is still higher than the composition with $x=$ 0.0. However, the strain drops to a lower value of 88 ppm for the composition containing 40% Mn. On the other hand, the magnetostriction values for all the compositions in the CFMO series are less than that of the parent compound. The

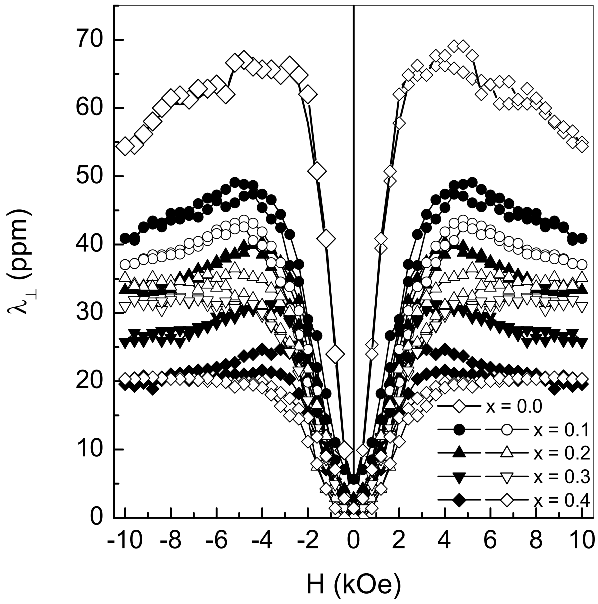

Figure 4.23: Magnetostriction measured perpendicular to the field direction, as a function of field, for the different compositions in $Co_{1.2-x}Mn_xFe_{1.8}O_4$ (CMFO) (filled symbols) and $Co_{1.2}Fe_{1.8-x}Mn_xO_4$ (CFMO)(open symbols).

value is decreased from 88 ppm to 85, 62, 42 and 38 ppm for $x = 0.1$, 0.2, 0.3 and 0.4, respectively.

The perpendicular measurements show a continuous decrease in the magnetostriction for both CMFO and CFMO series with increasing Mn content. The values of maximum magnetostriction are 67, 47, 39, 30 and 22 ppm for $x = 0.0$, 0.1, 0.2, 0.3 and 0.4, respectively for the CMFO series and 42, 38, 31 and 19 ppm for $x = 0.1$, 0.2, 0.3 and 0.4, respectively, for the CFMO series. Thus, a larger decrease in magnetostrictive strain, in both parallel and perpendicular directions, is observed when Mn is substituted for Fe.

The variation of the maximum magnetostriction as a function of Mn concentration is shown in Fig. 4.24. For the CFMO series, the magnetostriction decreases continuously as the concentration of Mn is increased. This is similar to the results reported for $CoFe_{2-x}Mn_xO_4$ [13]. On the other hand, $\lambda_{\|}$ increases by 25% for $x = 0.1$ in the CMFO series, and then decreases almost linearly with increasing Mn concentration, so that $\lambda_{\|}$ is comparable for both $x = 0$ and 0.4 in $Co_{1.2-x}Mn_xFe_{1.8}O_4$. However, in the case of the perpendicular magnetostriction, the highest value of 67 ppm is obtained for the un-

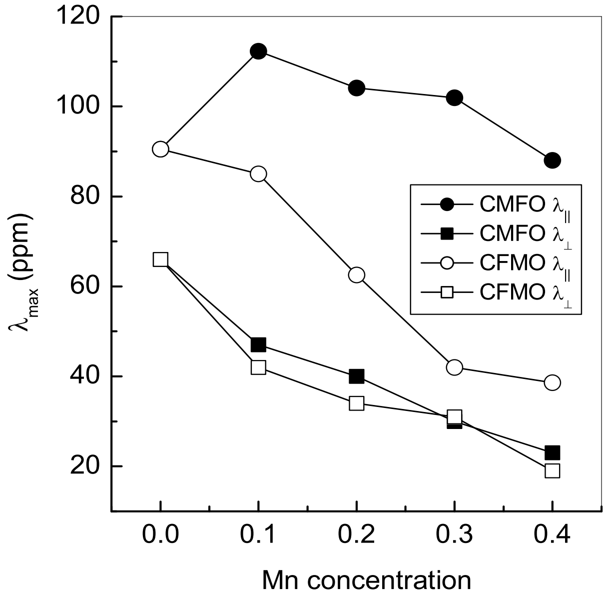

Figure 4.24: Variation of the magnitude of maximum magnetostriction as a function of Mn concentration in $Co_{1.2-x}Mn_xFe_{1.8}O_4$ (CMFO) and $Co_{1.2}Fe_{1.8-x}Mn_xO_4$ (CFMO).

doped compound. $\lambda_\perp$ decreases continuously in a similar fashion for both the series with increasing concentration of Mn.

The variations of volume (ω) and anisotropic (λ_t) magnetostrictions as a function of Mn concentration are shown in figure 4.25. This comparison shows that there is a marked dependence of ω as well as λ_t on Mn content. Apart from the variations in the volume and anisotropic magnetostrictions, the magnetic field required to achieve the maximum strain (H_{max}) is also found to be different for the CMFO and CFMO series. The variation of H_m as a function of Mn concentration is shown in figure 4.26. For magnetostriction measurements in the parallel direction, H_{max} is found to be relatively less and it decreases with increasing Mn content. Higher value of strain is obtained at lower magnetic field strengths. For example, for $x = 0.1$ in the CMFO series, maximum magnetostriction of 112 ppm is obtained at a field of ~2 kOe compared to 90 ppm at ~3 kOe for the un-substituted composition ($x = 0$). In the perpendicular direction, the maximum of the magnetostriction curve shifts to relatively higher magnetic fields for the CFMO series up to $x = 0.2$ and then decreases whereas a continuous decrease is observed in the case of CMFO. The results indicates that Mn substitution for Co is much more effective in order

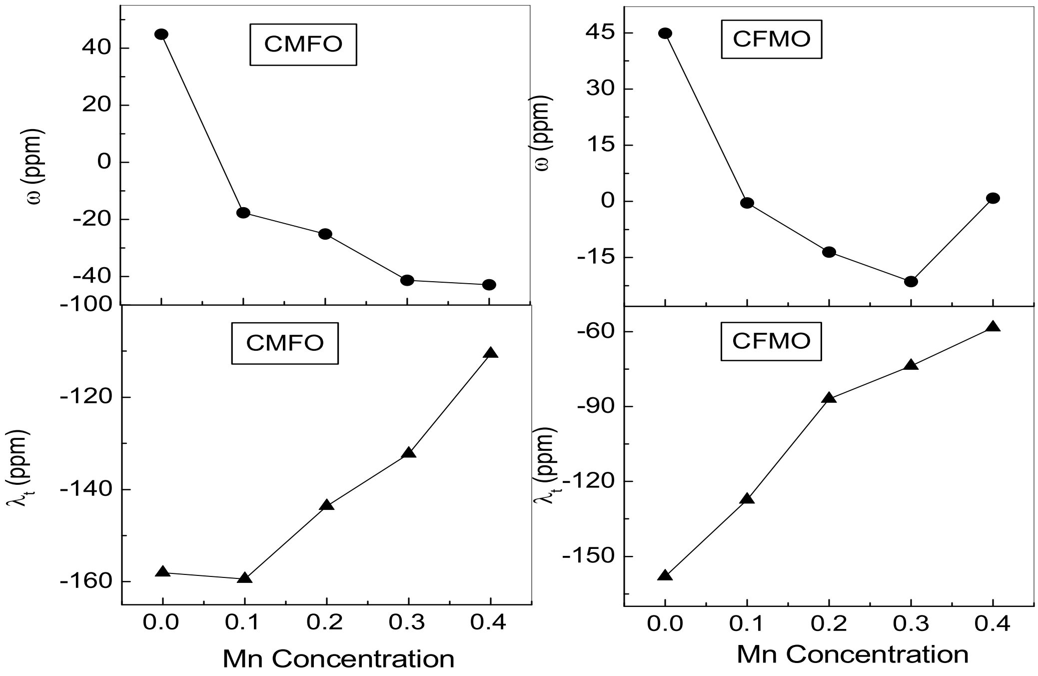

Figure 4.25: The variation of volume (ω) and anisotropic strain (λ_t) with Mn concentration for the samples in the $Co_{1.2-x}Mn_xFe_{1.8}O_4$ (CMFO) and $Co_{1.2}Fe_{1.8-x}Mn_xO_4$ (CFMO) series.

to reduce the magnetic field required than substituting Mn for Fe.

The slope of the magnetostriction curve (dλ/dH) for both the parallel and perpendicular measurements is shown in figure 4.27. It is observed that the rate of change of magnetostriction along the parallel direction is increased with the substitution of Co by Mn in $Co_{1.2-x}Mn_xFe_{1.8}O_4$ whereas in all other cases the rate decreases. The slope is almost doubled for 30% Mn substitution for Co in the parallel direction. Lower slope values are observed for measurements in the perpendicular direction for both CMFO and CFMO series.

A close comparison of the observed magnetostrictive strains with the microstructures shown in figure 4.14 indicate correlation between the microstructure and the changes in the magnetostriction. Uniform microstructure is observed for the compositions in the CMFO series and a discontinuous grain growth with large sized grains along with increased porosity is observed with increasing Mn content for the compositions in the CFMO series.

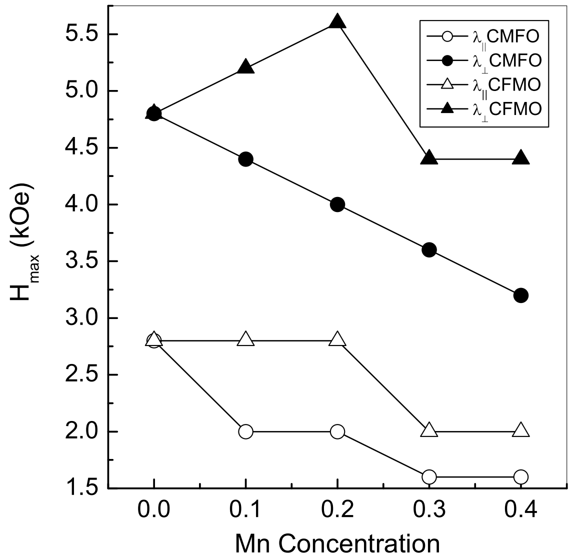

Figure 4.26: The variation of the magnetic field H_{max} at which maximum magnetostriction is obtained, as a function of Mn concentration in $Co_{1.2-x}Mn_xFe_{1.8}O_4$ (CMFO) and $Co_{1.2}Fe_{1.8-x}Mn_xO_4$ (CFMO) series.

Such a discontinuous grain growth may lead to the pinning of domain walls in the grain boundary region thereby affecting the response of the domains to the applied magnetic field and reducing the magnetostriction, which is in agreement with the lower strains observed in the case of CFMO series of compositions. This again underpins the importance of microstructural control in determining the magnetostrictive properties of the compositions. The different parameters such as magnetostrictive strain in the parallel ($\lambda_{\parallel}$), and perpendicular ($\lambda_{\perp}$) directions, maximum magnetic field (H_{max}) required to achieve the maximum magnetostriction, anisotropic magnetostriction and volume magnetostriction for different compositions are summarized in Table 4.7.

In summary, the substitution of Fe and Co by Mn on the magnetostrictive properties of $Co_{1.2}Fe_{1.8}O_4$ shows strong dependence of magnetostriction on the Mn content in both cases. The substitution of Co by Mn enhances the magnetostriction for small values of x in $Co_{1.2-x}Mn_xFe_{1.8}O_4$ whereas magnetostriction decreases continuously with increasing x in $Co_{1.2}Fe_{1.8-x}Mn_xO_4$. A twofold increase in the initial slope, $d\lambda/dH$, with large magnetostriction as compared to that of the unsubstituted compound is observed when small

Table 4.7: Summary of $\lambda_{\parallel}$, $\lambda_{\perp}$, H_{max}, $d\lambda/dH$, λ_t and ω for different compositions in the $Co_{1.2-x}Mn_xFe_{1.8}O_4$ (CMFO) and $Co_{1.2}Fe_{1.8-x}Mn_xO_4$ (CFMO) series.

Mn Content	$\lambda_{\parallel}$ (ppm)	$\lambda_{\perp}$ (ppm)	$H_{max}(\parallel)$ (kOe)	$H_{max}(\perp)$ (kOe)	$d\lambda/dH_{\parallel}$ (ppm/kOe)	$d\lambda/dH_{\perp}$ (ppm/kOe)	λ_t (ppm)	ω (ppm)
CMFO								
$x = 0.0$	-90	67	2.8	4.8	56.4	37.9	-158.0	44.9
$x = 0.1$	-112	47	2.0	4.4	92.7	14.1	-159.4	-17.7
$x = 0.2$	-104	39	2.0	4.0	109.0	14.1	-143.5	-25.1
$x = 0.3$	-101	30	1.6	3.6	122.0	12.9	-132.2	-41.3
$x = 0.4$	-88	22	1.6	3.2	83.5	12.3	-110.5	-42.9
CFMO								
$x = 0.0$	-90	67	2.8	4.8	56.4	37.9	-158.0	44.9
$x = 0.1$	-85	42	2.8	5.2	53.2	14.1	-123.3	-0.4
$x = 0.2$	-62	24	2.8	5.6	43.5	12.2	-87.0	13.5
$x = 0.3$	-42	31	2.0	4.4	42.0	8.8	-73.7	-21.4
$x = 0.4$	-38	19	2.0	4.4	27.7	6.6	-58.3	-0.8

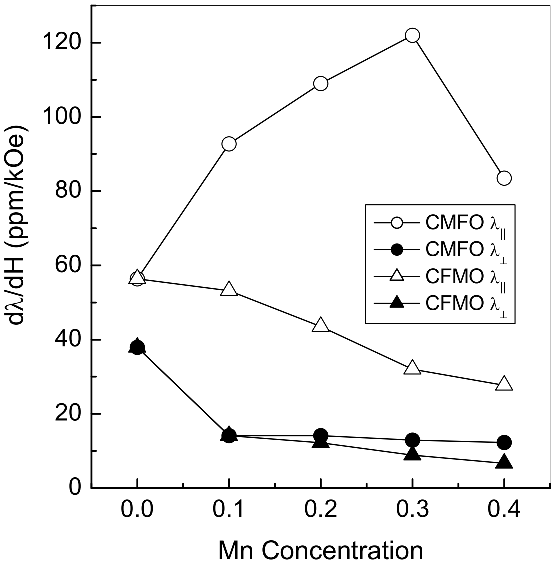

Figure 4.27: The Variation of the initial slope of magnetostriction (dλ/dH) with field as a function of Mn concentration for different compositions in the CMFO and CFMO series.

amounts of Co is replaced by Mn. Similarly, the field at which maximum magnetostriction is obtained is also reduced by 50% by this substitution. Thus, the present work shows that magnetostriction in cobalt ferrite can be enhanced by the substitution of small fraction of Co by Mn and this leads to an increase in the strain derivative as well as magnetostriction at lower magnetic fields.

4.5 Conclusions

The effect of substitution of Co and Fe by Mn on the magnetostrictive properties is analyzed for $CoFe_2O_4$ as well as $Co_{1.2}Fe_{1.8}O_4$. Magnetostriction is found to be affected more by the substitution of Mn for Co than for Fe. Enhancement in the slope of the magnetostriction curve as well as an enhanced magnetostriction in the perpendicular direction for 10% Mn content are observed in the case of substitution studies on $CoFe_2O_4$. The studies carried on Mn substitution for Fe and Co in $Co_{1.2}Fe_{1.8}O_4$ also showed that the substitution of Mn for Co can lead to better control over the magnetostrictive properties than the substitution for Fe. Therefore, the present studies show that it is possible to tune the magnetostriction of cobalt ferrite by suitable substitution of Mn for Fe and Co. The present work shows a way to tune the magnetostriction by effective substitution of Fe and Co by Mn for a choice to have materials with controlled magnetostrictive response for stress sensing and other applications at much lower magnetic field strengths.

References

[1] B. S. Trivedi and R. G. Kulkarni, *Solid State Commun.* 86 (1993) 327.

[2] P. N. Vasambekar, C. B. Kolekar and A. S. Vainganka r, *Mater. Chem. Phys.* 60 (1999) 282.

[3] K. P. Chae, Y. B. Lee, J. G. Lee and S. H. Lee, *J. Magn. Magn. Mater.* 220 (2000) 59.

[4] M. A. Gabal and S. S. Ata-Allah, *J. Mater. Chem. Phys.* 85 (2004) 104.

[5] T. T. Ahmed, I. Z. Rahman and M. A. Rahman, *J. Mater. Process. Technol.* 153154 (2004) 797.

[6] K. P. Chae, J-G. Lee, H. S. Kweon and Y. B. Lee, *J. Magn. Magn. Mater.* 283 (2004) 103.

[7] R. K. Sharma, O. Suwalka, N. Lakshmi, K. Venugopalan, A. Banerjee and P. A. Joy, *Mater. Lett.* 59 (2005) 3402.

[8] G. V. Duong, N. Hanha, D. V. Linha, R. Groessinger, P. Weinberger, E. Schafler and M. Zehetbauer, *J. Magn. Magn. Mater.* 311 (2007) 46.

[9] R. D. Greenough and E. W. Lee, *J. Phys. D.* 3 (1595) 1970.

[10] A. J. Pointon and N. P. Akers, *J. Magn. Magn. Mater.* 30 (1982) 50.

[11] F. S. Galasso, *Structure and Properties of Inorganic Solids* (Pergamon Press, Oxford, 1970).

[12] M. R. J. Gibbs, *Modern Trends in Magnetostriction Study and Application* (Kluwer Academic, Dordrecht, 2000).

[13] J. A. Paulsen, A. P. Ring, C. C. H. Lo, J. E. Snyder and D. C. Jiles, *J. Appl. Phys.* 97 (2005) 044502.

[14] O. F. Caltun, H. Chiriac, N. Lupu, I. Dumitru and B. P. Rao, *J. Optoelectron. Adv. Mater.* 9 (2007) 1158.

[15] O. F. Caltun, G. S. N. Rao, K. H. Rao, B. P. Rao, C. Kim, Chong-Oh Kim, I. Dumitru, N. Lupu and H. Chiriac, *Sensor Letters* 5 (2007) 1.

[16] K. Krieble, T. Schaeffer, J. A. paulsen, A. P. Ring, C. C. H. Lo and J. E. Snyder, *J. Appl. Phys.* 97 (2005) 10F101.

[17] Y. Melikhov, J. E. Snyder, D. C. Jiles, A. P. Ring, J. A. Paulsen, C. C. H. Lo and K. W. Dennis, *J. Appl. Phys.* 99 (2006) 08R102.

[18] R. D. Shannon, *Acta Crystallogr.* A 32 (1976) 751.

[19] B. Zhou, Y-W. Zhang, C-S. Liao and C-H. Yan, *J. Magn. Magn. Mater.* 247 (2002) 70.

[20] G. A. Sawatzky, F. V. D. Woude and A. H. Morrish, *Phys. Rev.* 187 (1969) 187.

[21] R. M. Bozorth, *Phys. Rev.* 50 (1936) 1076.

[22] Y. Chen, J. E. Snyder, C. R. Schwichtenberg, K. W. Dennis, R. W. McCallum and D. C. Jiles, *43rd annual conference on Magntism and Magnetic Materials* (1998).

[23] F. W. Harrison, W. P. Osmond and R. W. Teale, *Phys. Rev.* 106 (1957) 865.

[24] D. C. Jiles, *Acta Mater.* 51 (2003) 5907.

[25] D. G. Wickham and W. J. Croft, *J. Phys. Chem. Solids* 7 (1958) 351.

[26] G. U. Kulkarni, K. R. Kannan, T. Arunarkavalli and C. N. R. Rao, *Phys. Rev.* B 49 (1994) 724.

PART-II

Chapter 5

Studies on $LaMn_{1-x}Fe_xO_3$

5.1 Introduction

Studies on the magnetic properties of perovskite type lanthanum manganite and substituted lanthanum manganites gained momentum after the discovery of colossal magnetoresistance (CMR) in this class of materials [1–4]. The parent compound $LaMnO_3$ is an A-type antiferromagnetic insulator where the high-spin state of Mn^{3+} (S=2) couples antiferromagnetically via superexchange interaction [5]. The transport and magnetic properties of $LaMnO_3$ can be altered by the substitution of suitable metal ions in the A-site of the ABO_3 perovskite structure. It has been found that the changes in the transport and magnetic properties are generally associated with the spin states of Mn ion in the perovskite structure [6]. The substitution of divalent metal ions like Ca^{2+}, Ba^{2+} and Sr^{2+} for La^{3+} induces ferromagnetism in $LaMnO_3$, because of the changes in the spin state of Mn from Mn^{3+} to Mn^{4+}. This shows that the substitution at the A-site of the ABO_3 perovskite structure ultimately affects the ion situated at the B-site. Therefore, it should be possible to mimic the properties observed after the A-site substitution, by direct substitution at the B-site by proper ions. Such studies have in fact confirmed the presence of ferromagnetic behavior in the case of substitution of Co, Ni and Cr for Mn in $LaMnO_3$ [7–9]. However, the substitution at the B-site is more complicated because of the possibility for the presence of multiple valance states of the B-site ions.

The substitution of Mn by Fe in the $La_{1-x}D_xMnO_3$ (where D = Ca^{2+}, Ba^{2+}, Sr^{2+} etc) system, which is already ferromagnetic and metallic, destroys ferromagnetism and conductivity with increasing Fe^{3+} ion concentration. The consequences of Fe substitution have been explained based on the breakdown of long range order in the system as

Fe^{3+} occupies the B-sites in a random manner, the increased strength of the Fe^{3+}-O-Fe^{3+} antiferromagnetic superexchange interactions, and the weakening of the Mn^{3+}-O-Mn^{4+} double exchange mechanism [10–15]. These observations are contradicting to the fact that Fe^{3+}-O-Mn^{3+} is expected to be one of the strongest ferromagnetic interaction according to Goodenough-Kanamori rules [16]. From the comparative studies on the effect of substitution of different transition elements for Mn in $La_{0.7}Ca_{0.3}MnO_3$ indicated some unusual effect on the substitution of Fe^{3+} for Mn^{3+} [17]. From comparative studies on the role of impurity e_g levels on the properties of $Pr_{0.5}Ca_{0.5}MnO_3$ doped with 5% of different elements, Hebert *et al.* showed that doping elements with d^0 and d^{10} configurations and dopants without d orbitals destroy ferromagnetic ordering and Fe^{3+} also belongs to this class in spite of its d^5 electronic configuration [18]. A similar effect has been observed in the case of direct Mn-site substitution also.

Although ferromagnetism is induced on the substitution of the transition metals Co, Ni, and Cr for Mn in $LaMnO_3$, it was observed that the same effect is not produced on the substitution of Fe [19]. However, the studies on the Fe substituted manganites took a new turn after the paper published by ueda *et al.* who made artificial superlattices of $LaMnO_3$ and $LaFeO_3$ and found that the magnetic properties could be controlled by altering the ordering of Mn and Fe ions in the lattice [20]. Ferromagnetism, with a T_C of 230 K, is observed for stacking on the < 111> plane of $SrTiO_3$ substrate whereas spin-glass-like behavior has been observed for <100> and <110> stacking. Further report by the same research group on the observation of ferromagnetism above room temperature in a thin film sample of $LaMn_{0.5}Fe_{0.5}O_3$, where the Mn^{3+} and Fe^{3+} ions were made to order, confirms the role of randomness in the occupancy of Fe^{3+} in determining the magnetic properties [21]. The driving force for the ordering of the ions in the B site of the perovskite lattice, when there are more than one type of ions is present, is either the difference in the charge or the size or both these factors together. So, it is clear that, in a polycrystalline sample of $LaMn_{0.5}Fe_{0.5}O_3$, if Fe is present as trivalent high spin ion, the compound is less likely to have ferromagnetic behavior due to the randomness in the occupancy, as trivalent Mn and Fe ions have identical ionic size (0.65 Å) and ionic charge [22].

Although ferromagnetism was not observed in polycrystalline $LaMn_{0.5}Fe_{0.5}O_3$ in the earlier studies [19], cluster-glass-like features with large difference between the field cooled and zero field cooled magnetization below 260 K have been reported for this compound very recently [23]. The difference between the compounds in the above two reports is in the difference in the synthesis and processing conditions. Recent studies on polycrystalline $LaMn_{0.5}Co_{0.5}O_3$ and $LaMn_{0.5}Ni_{0.5}O_3$ [24, 25] synthesized by a low-temperature method and annealed at different temperatures, have shown the interplay of different spin states of Mn and the substituted ions in the two compounds and the effect of these parameters on their magnetic properties. These studies also showed how the processing conditions affect the magnetic properties, due to the changes in the spin states of Mn and the substituted ion. In the present study we have synthesized polycrystalline samples in the series $LaMn_{1-x}Fe_xO_3$ by a low temperature method and the magnetic properties of the resulting compositions have been evaluated after annealing at different temperatures in air. Mössbauer, EPR and IR spectroscopic studies were made to get more information on the changes in the magnetic properties and the state of Mn and Fe ions in the compound.

5.2 Synthesis

The synthesis of the compositions in the series $LaMn_{1-x}Fe_xO_3$ ($0.0 \leq x \leq 0.5$) was carried out using the low temperature glycine nitrate combustion route. Stoichiometric amounts of La_2O_3 and Mn metal powder were dissolved separately in minimum amount of 4N nitric acid to get the corresponding metal nitrates. $Fe(NO_3)_3$ was dissolved separately in minimum amount of distilled water and then the metal nitrate solutions were mixed together. Water solution of glycine was added to this metal nitrates solution by maintaining the metal to glycine molar ratio as 1:2. The final mixed solution was evaporated on a hot plate at 200 °C , resulting in the formation of a thick fluffy mass, which finally burned vigorously forming a black powder. This powder was then heated in air at different temperatures, at 200 °C and 700 °C for 12 hours each and at 1300 °C for 24 hours. The powders were characterized using different techniques such as XRD, VSM and IR studies. For the composition with $x = 0.5$, further studies were carried out with Mössbauer and EPR measurements.

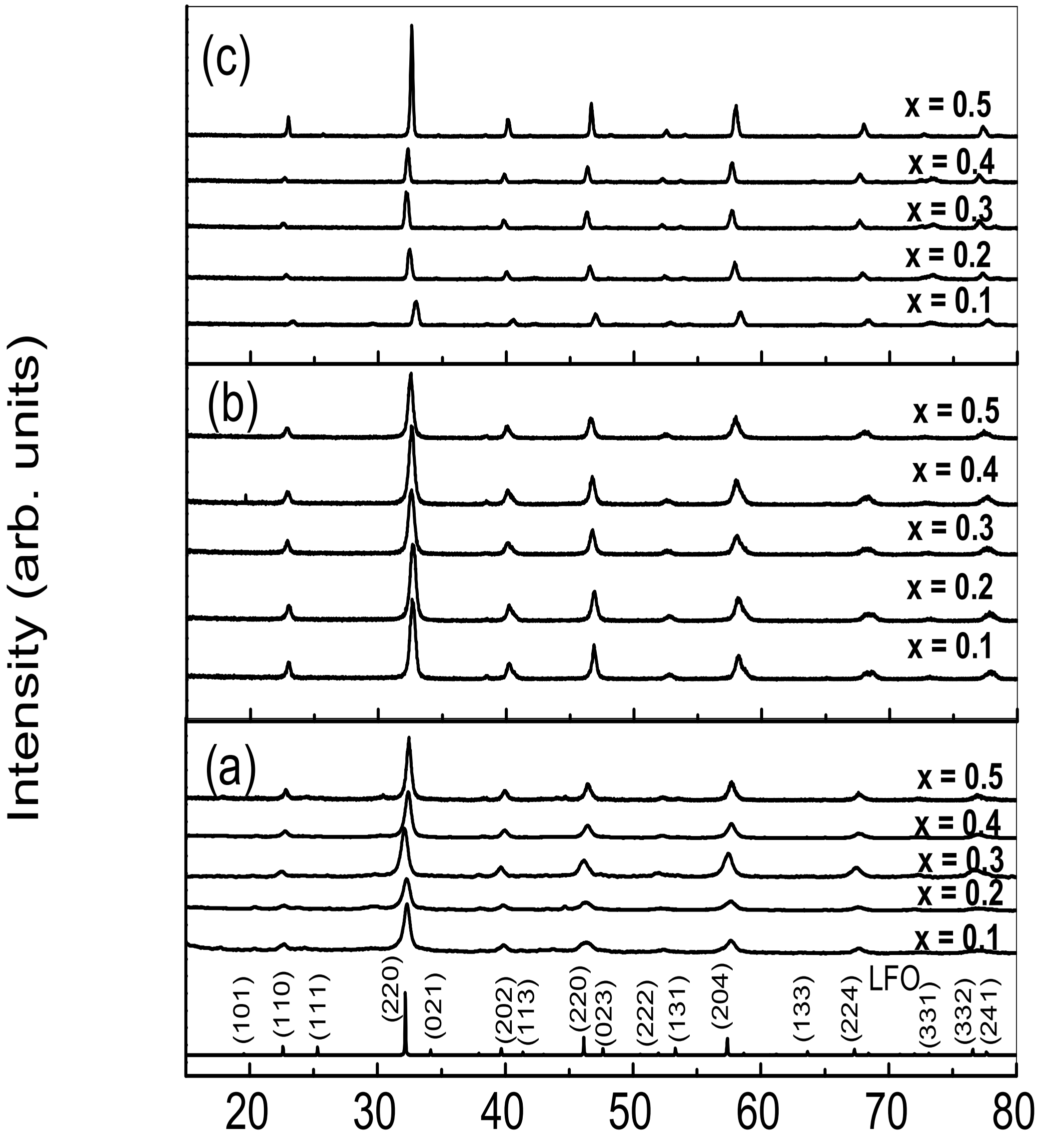

Figure 5.1: Powder XRD patterns of different compositions in the $LaMn_{1-x}Fe_xO_3$ series annealed at (c) 200 °C, (b) 700 °C and (c) 1300 °C. The simulated XRD pattern of $LaFeO_3$ (LFO) is shown and indexed for comparison.

5.3 Powder XRD Analysis

The powder XRD patterns of different compositions in the $LaMn_{1-x}Fe_xO_3$ (LMF) series annealed at different temperatures are shown in figure 5.1. All the samples, after annealing at 200 °C, show identical characteristics in the powder XRD patterns. The smaller particles formed during the combustion synthesis are responsible for the broad reflections in the diffraction patterns. All the XRD patterns could be indexed to the $GdFeO_3$ type orthorhombic perovskite structure with the space group *pbnm*. The samples annealed at 700 °C and 1300 °C also show similar features in the XRD patterns, excepted for the decreased broadness of the reflections, as observed in the case of the 200 °C annealed samples. The lattice parameters were calculated by the least square refinement method. The variation in the orthorhombic lattice parameters with increasing Fe concentration is shown in figure 5.2. As can be seen from the figure, for the compositions annealed at 200 °C, 700 °C and 1300 °C, the lattice parameters a, b, and c remain almost constant. This is likely to be due to the the identical ionic radii of Mn^{3+} and Fe^{3+}. It is expected that there will not be any major shift in the lattice parameters. Few studies have been reported on the structural characteristics of the compositions in the series $LaMn_{1-x}Fe_xO_3$. An orthorhombic structure has been reported by Gilleo [19] for the compositions in the series $LaFe_xMn_{1-x}O_3$ for $0.5 < x \leq 1$. Similarly, Wu *et al.* have also observed orthorhombic structure for Fe rich compositions in the series $LaFe_xMn_{1-x}O_3$, where the variation in the lattice parameters was found to be very small because of the identical ionic radii of Mn^{3+} and Fe^{3+} [26]. However, Miwa *et al.* have reported rhombohedral and monoclinic phases for a gradual substitution of Fe for Mn in $LaMnO_3$ [27]. Recently, Tong *et al.* have shown that the structure changes from rhombohedral to orthorhombic with increasing Fe content [28].

5.4 Magnetic Measurements

The zero field cooled (ZFC) magnetization curves recorded in a magnetic field of 50 Oe are shown in figure 5.3. The samples annealed at 200 °C, show sharp magnetic transitions between 100 and 125 K. The onset of the magnetic transition is observed below 125 K for all compositions. The parent compound $LaMnO_3$ is an antiferromagnet, having a

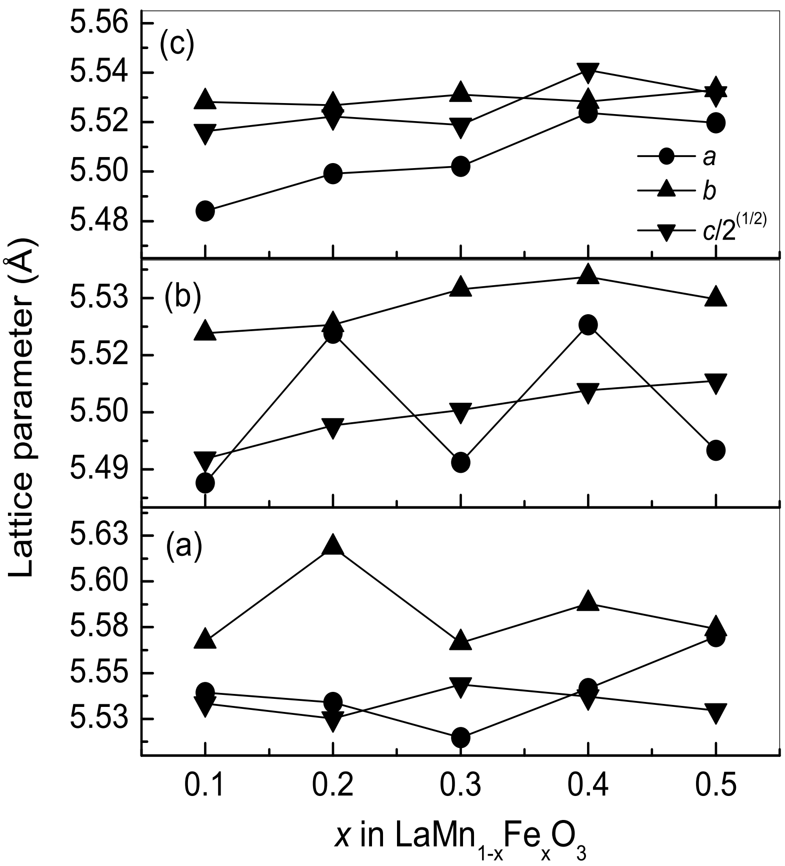

Figure 5.2: Variation of the orthorhombic lattice parameters as a function of Mn concentration in the $LaMn_{1-x}Fe_xO_3$ series for samples annealed at (a) 200 °C, (b) 700 °C and (c) 1300 °C.

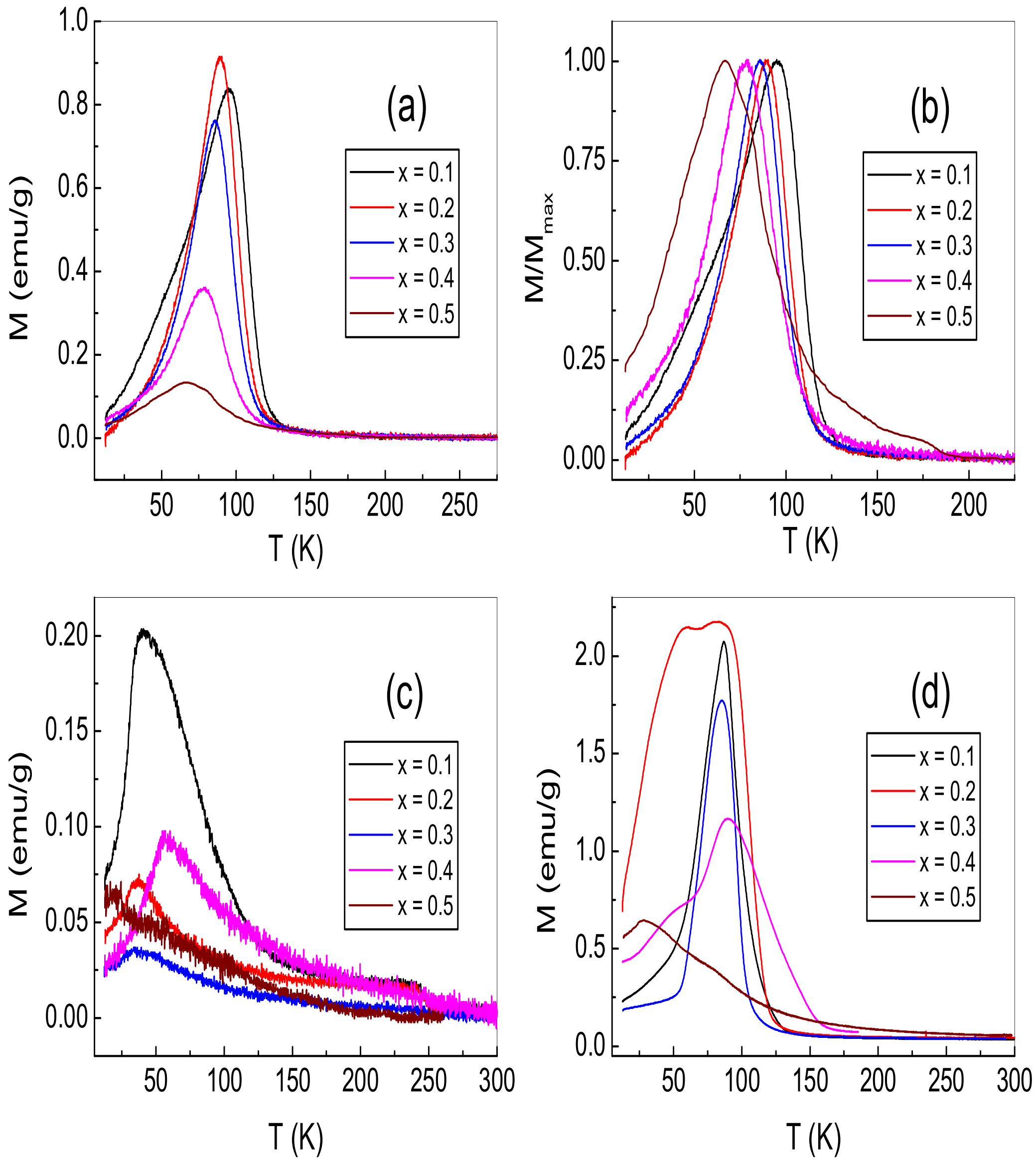

Figure 5.3: ZFC magnetization (H = 50 Oe) curves of different compositions in $LaMn_{1-x}Fe_xO_3$ series annealed at (a) 200 °C, (c) 700 °C and (d) 1300 °C. (b) shows the normalized magnetization curves of the samples annealed at 200 °C.

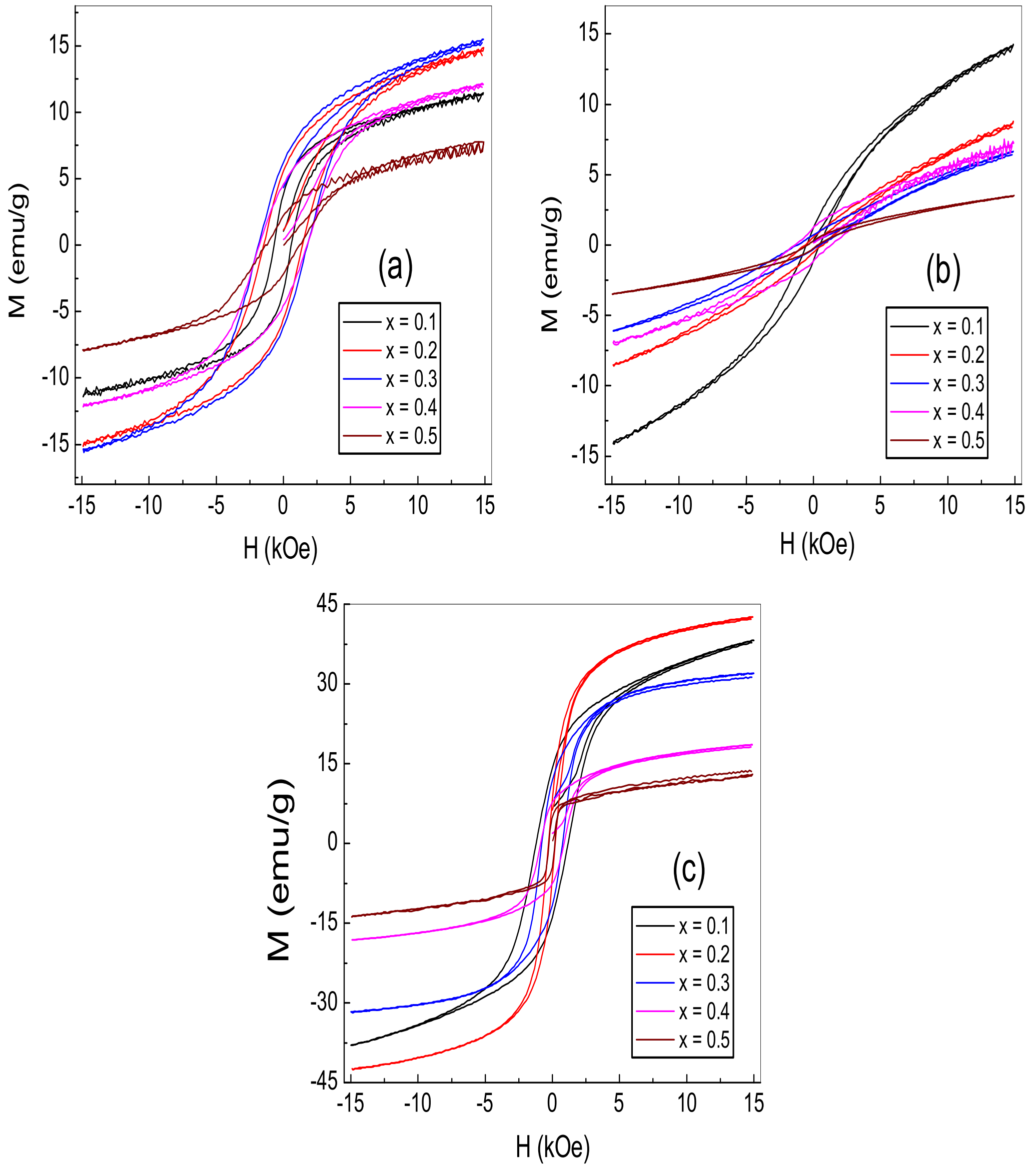

Figure 5.4: Magnetic field dependence of magnetization recorded at 12 K for different compositions in the $LaMn_{1-x}Fe_xO_3$ series annealed at (a) 200 °C, (b) 700 °C and (c) 1300 °C.

Neel temperature of ~140 K. The magnetic transition temperature for the compositions annealed at 200 °C is found to decrease with increasing Fe concentration. Also, the peak temperature decreases continuously with increasing Fe content, which can be clearly seen in figure 5.3(b), where normalized magnetization curves for the samples annealed at 200 °C are shown. It is also observed that the magnetic transition becomes broadened over a wide temperature range with increasing Fe content. For the composition with x = 0.5, a small cusp is observed at 65 K. In the case of the samples annealed at 700 $°C$ (figure 5.3(c)), the magnetic transition is found to be broadened over a wide temperature range. The peak temperature decreases for compositions up to $x = 0.3$, and then further increases for $x = 0.4$. However, the composition with $x = 0.5$ does not show any kind of magnetic transition or peak down to 12 K. Even for those compositions showing a peak in the magnetization, the over all magnitude of magnetization at the peak temperature is much less than that observed for the sample annealed at 200 °C. For the samples heated at 1300 °C, the ZFC magnetization curves are shown in figure 5.3(d). Distinct magnetic transitions are observed 100 and 125 K for the compositions up to $x = 0.3$, with even higher magnetizations than that observed for 200 °C annealed samples. The composition containing 20% Fe shows a double peak behavior in the ZFC magnetization curve. The magnetic transition becomes broader for compositions with higher Fe content. The composition with $x = 0.5$ shows a continuous rise in the magnetization with decreasing temperature and exhibits a cusp at ~27 K. For $x = 0.5$, the magnetization is very low for all three annealed samples.

The changes in the magnitudes of magnetization of the annealed samples are clearly visible from field dependence of magnetization recorded at 12 K, shown in figure 5.4. There is no saturation of magnetization at a maximum magnetic field strength 15 kOe for any of the samples. All the compositions annealed at 200 °C show distinct magnetic hysteresis loops as can be seen from figure 5.4(a). The magnetization at 15 kOe is found to increase with increasing Fe content up to $x = 0.3$ showing a magnetization value of 15.3 emu/g, and then decreases for higher Fe concentration. Similarly a continuous enhancement in coercivity is observed with increasing Fe content up to $x = 0.3$. Largest coercivity of ~1830 Oe observed for $x = 0.3$. The coercivity is found to decrease for compositions with $x = 0.4$ and $x = 0.5$. The composition with $x = 0.5$, also exhibits a distinct hysteresis loop having a coercivity 1280 Oe. The M-H curves of the 700 °C annealed samples (figure 5.4(b)) show distinct loops. The M-H loops do not show saturation up to a maximum magnetic field strength of 15 kOe and the magnetization shows a continuous increase as observed in case of superparamagnetic systems. The magnetization is found to decrease continuously with increasing Fe concentration with a maximum magnetization of 14 eum/g for the composition with $x = 0.1$. The coercivity increases with x and a maximum coercivity of 1345 Oe is observed for the composition with $x = 0.4$. Although, the composition with $x = 0.5$ does not show any magnetic transition or cusp down to 12 K, it exhibits a clear hysteresis loop but with s smaller coercivity than that of $x =$ 0.4, indicating that the sample is not truly paramagnetic. For the samples annealed at 1300 °C, the field dependence of magnetization is shown in figure 5.4(c). Enhancement in the magnetization is observed as compared to the compositions annealed at lower temperatures. The composition with $x = 0.2$ shows a maximum magnetization of 42 emu/g, almost three times that observed for the sample annealed at 200 °C. A continuous decrease in the magnetization is observed for the compositions with higher Fe content. However, no regular trend is observed in the coercivity of the samples annealed at 1300 °C. The largest coercivity of 1180 Oe is obtained for $x = 0.1$ and the lowest coercivity of 250 Oe is observed for $x = 0.2$.

The temperature dependence of the magnetization of the corresponding compositions for samples annealed at 200 and 1300 °C is almost similar, except for the difference the the magnitude of magnetization and coercivity. The larger coercivities and lower magnetizations of the samples annealed at 200 °C are likely to be due to the smaller particle sizes of these samples. The relatively lower magnetizations and the nature of the magnetization curves of the samples annealed at 700 °C suggest different type of magnetic phenomena of these samples.

5.5 IR Spectroscopic Studies

The IR spectra of the different compositions in the series $LaMn_{1-x}Fe_xO_3$, annealed at different temperatures, are shown in figure 5.5. For the perovskite ABO_3, the B-O bond stretching vibration of the BO_6 octahedra (ν_1 of the IR active F_{1u} mode of vibration) is observed in the 500 to 700 cm^{-1} region [26, 29]. Wu *et al.* have reported the IR spectral

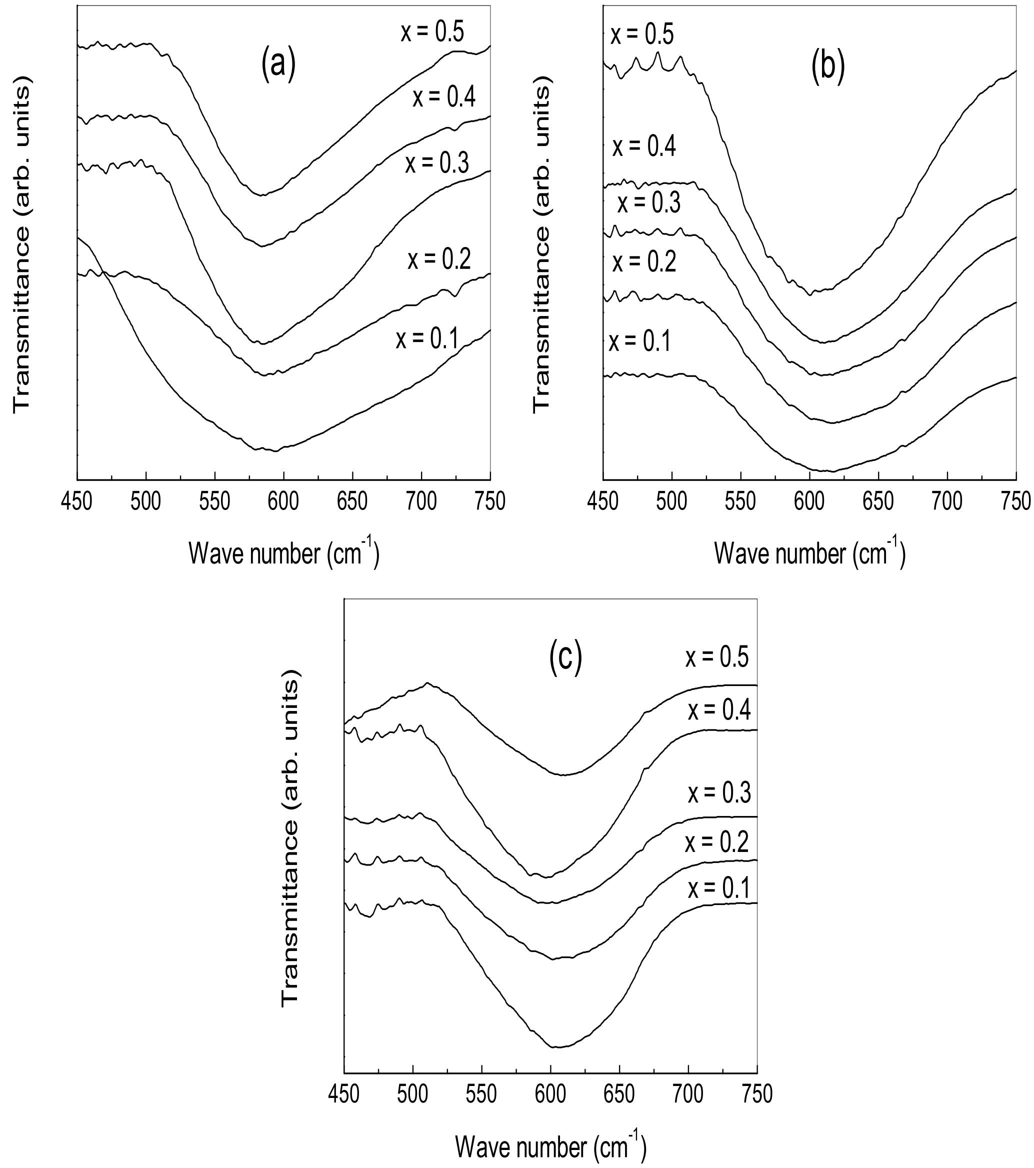

Figure 5.5: IR spectra of different compositions in $LaMn_{1-x}Fe_xO_3$ series annealed at (a) 200 °C, (b) 700 °C and (c) 1300 °C.

data of $LaMn_{1-x}Fe_xO_3$ in the entire compositional range, for samples synthesized by a low temperature method and calcined at 950 °C [26]. It has been shown that the band due to ν_1 stretching vibration observed at 610 cm^{-1} for $LaMnO_3$ is shifted to 568 $^{-1}$ for $LaFeO_3$, indicating that the Fe-O bond has more ionic character. For $LaMn_{0.5}Fe_{0.5}O_3$, this band was observed at 606 $^{-1}$. The decreasing vibrational frequency of the ν_1 mode has been shown to be resulting from the joint action of the Mn-O and Fe-O stretching vibrations, indicating that geometrical factors are more predominant than electronic factors in the system. Therefore, a symmetric band is expected if the Mn^{3+} and Fe^{3+} ions are distributed uniformly in the B site of the perovskite lattice and the band becomes nonsymmetric if the distribution is nonuniform or when clustering occurs. The spectra shown in figure 5.5 reveal changes in the structure of the vibrational band with annealing. For the samples annealed at 200 °C, the stretching frequency is ∼600 cm^{-1}, with a broad shoulder towards higher frequencies. However, a more symmetric band is observed for the samples annealed at 700 °C at ∼606 cm^{-1}, similar to that reported by Wu *et al.* [26]. For the samples annealed at at 1300 °C, the band is shifted to ∼610 cm^{-1}, with a shoulder at ∼570 cm^{-1}.

Since all the samples annealed at different temperatures show different IR spectral features, it is reasonable to believe that some kind of clustering occurs in these samples. Since the samples annealed at 700 °C show symmetric IR bands and those annealed at 200 °C and 1300 °C show shoulders at higher and lower frequencies, respectively, it may be assumed that Mn-rich and Fe-rich clusters are present in the latter samples. Similarly, some unusual features, such as peak in the ZFC magnetization for samples with higher Fe concentration at 65 K, then the disappearance of the peak after annealing at 700 °C and stilling showing a distinct hysteresis loop, and again an enhanced magnetization after annealing to 1300 °C are observed for the composition with $x = 0.5$, apart from the changes in the features in the IR band. Hence, detailed studies are further carried out on this composition. Hereafter, the composition with $x = 0.5$ annealed at 200 °C, 700 °C, and 1300 °C, are referred to as LMF200, LMF700, and LMF1300, respectively.

5.6 Mössbauer Studies on $LaMn_{0.5}Fe_{0.5}O_3$

The Mössbauer spectra of the samples annealed at 200 °C, 700 °C and 1300 °C, shown in figure 5.6, were recorded at room temperature in order to identify the oxidation state

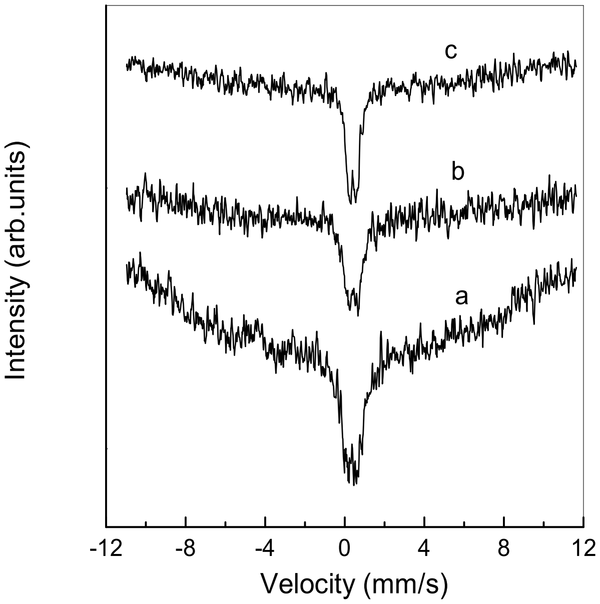

Figure 5.6: Room temperature Mössbauer spectra of $LaMn_{0.5}Fe_{0.5}O_3$ annealed at a) 200 °C, b) 700 °C and c) 1300 °C.

of Fe. The Mössbauer spectra show only doublets for all the samples indicating their paramagnetic nature. The isomer shifts of the samples annealed at 200 °C, 700 °C and 1300 °C are 0.33, 0.43 and 0.40 mm/s respectively. The observed isomer shift values in the present case are comparable to the values reported for the perovskite oxides $LaFeO_3$ and $SrFeO_{2.5}$ [30, 31] containing high spin Fe^{3+} ions. This indicates that the Fe ions are present in the trivalent high-spin state in all three samples. The isomer shift values are also comparable to the literature reported value for $LaMn_{0.5}Fe_{0.5}O_3$ [23]. The spectra are found to be identical to that reported by De *et al.* [23], where $LaMn_{0.5}Fe_{0.5}O_3$ synthesized at a low temperature and heated to 950 °C exhibits a large difference between the FC and ZFC magnetizations below 260 K. The latter observation is explained in terms of some local magnetic ordering. Tong *et al.* [28] have suggested the possibility of double exchange between Mn^{3+} (d^4) and Fe^{3+} (d^5), to explain the origin of ferromagnetism in $LaMn_{1-x}Fe_xO_3$ ($x \leq 0.4$), where similar doublet and isomer shift are observed. What is more interesting is the fact that the isomer shift initially increases to a larger value and then decreases. This is possible if the local environment of the Fe^{3+} ions is changed which affects the s-electron density. It may be assumed that the changes are due to the variation

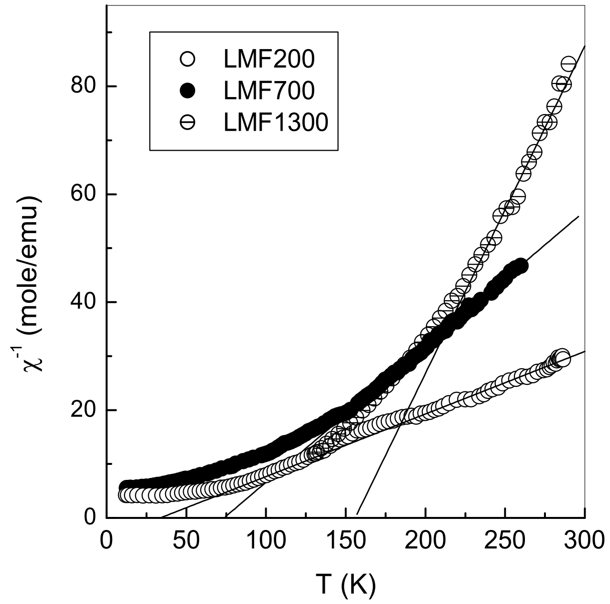

Figure 5.7: Temperature variation of the inverse of the magnetic susceptibility of LMF200, LMF700, and LMF1300.

in the degree of distribution of the Fe^{3+} ions in the lattice, so that larger shift is observed when the disorder is more, as reported for other systems [32, 33].

5.7 Susceptibility studies on $LaMn_{0.5}Fe_{0.5}O_3$

Although no strong magnetic signal or indication for any magnetic transition is observed from low field ZFC magnetization studies down to 12 K (see figure 1.3 c), the field dependent magnetization at 12 K shows a magnetic hysteresis loop (see figure 1.4 b) indicating the contribution from some ferromagnetic or ordered phase in LMF700. However, the magnetic susceptibility studies show the evidence for ferromagnetic exchange interactions in the sample annealed at 700 °C. Figure 5.7 shows the temperature dependence of the inverse of the magnetic susceptibility for the sample LMF200, LMF700 and LMF1300, measured in a magnetic field of 5000 Oe. Curie-Weiss behavior, χ = C/(T-Θ), is observed for all the samples at higher temperatures ($\geq$150 K). From least squares fit to the data in the linear region above 150 K, the effective paramagnetic moment, $\mu_{eff} = 2.828\sqrt{C}$, where C is the Curie constant, is obtained as 8.31, 5.64, and 3.63 μ_B, respectively, for

LMF200, LMF700, and LMF1300. Assuming that the samples contain only Mn^{3+} (S = 2) and Fe^{3+} (S = 5/2) ions, the spin only magnetic moment μ_{so} for $LaMn_{0.5}Fe_{0.5}O_3$ is calculated as $\mu_{so} = [0.5\mu_{Mn}^2 + 0.5\mu_{Fe}^2]^{1/2} = 5.43\mu_B$, where $\mu = [4S(S+1)]^{1/2}$. For the Mn^{4+} (S=3/2) and Fe^{2+} (S = 2) combination, $\mu_{so} = 4.42\mu_B$. The experimental value of the magnetic moment of LMF700 is comparable to the spin-only value for the Mn^{3+}/Fe^{3+} combination indicating that Mn and Fe ions are present in their trivalent high-spin states. On the other hand, the large value of the experimental moment of LMF200 is similar to that observed for superparamagnetic systems and is indicative of ferromagnetic clusters in the sample. The ferromagnetic clusters are likely to contain Mn^{3+} and Fe^{3+} ions with Mn^{3+}-O-Fe^{3+} and/or Mn^{3+}-O-Mn^{3+} ferromagnetic superexchange interactions. The paramagnetic Curie temperature, Θ, is obtained as 34, 78, and 156 K for LMF200, LMF700, and LMF1300, respectively. The positive values of Θ are indicating the presence of ferromagnetic exchange interactions. The increasing value of Θ with increasing annealing temperature is indicative of increasing strength of the ferromagnetic exchange interactions. The very low value of Θ for LMF200 suggests that there are more antiferromagnetic interactions present in the samples, pointing to the formation of larger Fe^{3+}-O-Fe^{3+} clusters with antiferromagnetic exchange interactions. From the larger effective magnetic moment and smaller Θ of this sample, it can be assumed that the sample contains small Mn-rich clusters contributing to the superparamagnetic behavior. Then the larger values of Θ and smaller values of the effective moments of LMF1300 favor a conclusion in terms of larger Mn-rich clusters with stronger ferromagnetic exchange interactions. Thus, from the magnetic susceptibility studies, it can be concluded that the samples annealed at lower temperatures contain small Mn-rich clusters and larger Fe-rich clusters whereas the high-temperature annealed samples contain larger Mn-rich clusters.

5.8 IR Spectra of $LaMn_{0.5}Fe_{0.5}O_3$

The IR spectra of LMF200, LMF700 and LMF1300 are compared in figure 5.8 . The 200 °C annealed sample show major features of $LaFeO_3$ with minor features of $LaMnO_3$ whereas the 1300 °C annealed sample show major features of $LaMnO_3$ and minor features due to $LaFeO_3$. However, the 700 °C annealed sample do not show any individual features of the end members. The IR spectral observations can be explained in terms

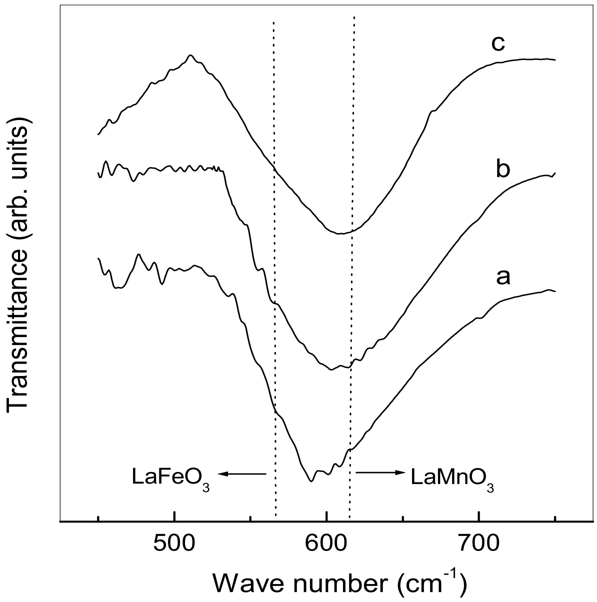

Figure 5.8: IR spectra of $LaMn_{0.5}Fe_{0.5}O_3$ annealed at a) 200 °C, b) 700 °C and c) 1300 °C.

of the formation of clusters due to nonuniform distribution of Mn^{3+} and Fe^{3+} ions in the lattice. In the 200 °C annealed sample, there are larger clusters involving Fe^{3+} ions and smaller clusters involving Mn^{3+} ions whereas in 1300 °C annealed samples, there are larger clusters involving Mn^{3+} ions and smaller clusters of Fe^{3+}. On the other hand, these ions are distributed more uniformly in 700 °C annealed compositions, but probably with smaller clusters. The IR spectral data support the conclusions drawn from the magnetic susceptibility studies.

5.9 EPR Studies on $LaMn_{0.5}Fe_{0.5}O_3$

The EPR spectra of LMF200, LMF700 and LMF1300 recorded at room temperature are shown in figure 5.9. Large changes are observed in the intensities and widths of the spectra, when the samples are heated at higher temperatures. On the other hand, the resonance field remains the same for all three samples. For the samples annealed at 700 °C, the intensity of the EPR signal is reduced to almost half of that of the sample annealed at 200 °C, whereas the peak-to-peak linewidth increases from 448 to 655 Gauss. For

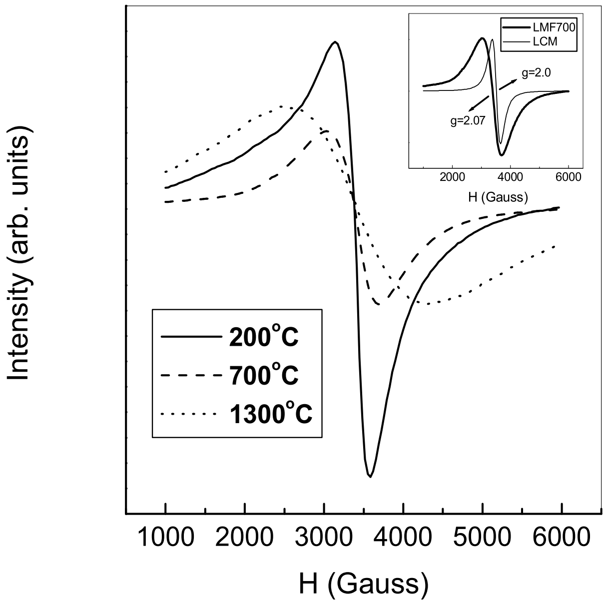

Figure 5.9: EPR spectra of $LaMn_{0.5}Fe_{0.5}O_3$ at 300 K, for samples annealed at different temperatures. Inset, comparison of the EPR spectra of LMF700 and $La_{0.7}Ca_{0.3}MnO_3$ (LCM).

1300 °C annealed sample, the EPR signal becomes extremely broad with a peak-to-peak linewidth of 1790 Gauss. Although the signal becomes broad, the intensity is found to increase when compared to that of the 700 °C annealed sample. In the La-site substituted manganites, where the EPR signal is due to the Mn^{3+}/Mn^{4+} pairs or interaction, the g value is close to 2.0 as shown in the inset of figure 5.9 for $La_{0.7}Ca_{0.3}MnO_3$. EPR signal from Fe^{3+} centers is also expected to give a g value of $\sim$ 2.0. However, the g values are close to 2.07 for all three samples and this indicates that Mn^{3+}/Fe^{3+} pairs are responsible for the resonance. The relative integrated area under the EPR curve is found to decrease from 2.4 for the sample annealed at 200 °C to 1 for the sample annealed at 700 °C and then increased to 3.9 for the 1300 °C annealed sample. The area under the resonance curve is related to the number of unpaired spins contributing to paramagnetic susceptibility. Mössbauer spectral data clearly indicated that Fe^{3+} ions are present in their high-spin trivalent oxidation states. In fact the changes in the intensities and area under the curves of the EPR signals can be directly correlated with the changes in the magnitude of the magnetization at low temperatures. Thus, the initial decrease and further large increase in the susceptibility may be explained in terms of the corresponding changes in the Mn^{3+}/Fe^{3+} interactions. Assuming that only Mn^{3+} and Fe^{3+} ions are present in all the samples, the changes in the EPR data may be explained in terms of the distribution of these ions in the perovskite lattice. This degree of distribution is then responsible for the magnetic properties also. The changes in the peak-to-peak linewidth is a direct measure of the magnetic exchange interactions and the linewidth increases because of the weakening of the exchange field. For example, Gutierrez *et al.* [34] have reported that the width of resonance line increases with Fe content in $La_{0.7}Pb_{0.3}Mn_{1-x}Fe_xO_3$, and this corresponds to a decrease of the exchange narrowing, indicating lowering of the strength of the ferromagnetic interactions. Compositions with larger Fe content show spin-glass-like behavior due to the antiferromagnetic coupling between Mn and Fe ions forming ferromagnetic clusters. On the other hand, Rubinstein *et al.* [13] have shown that in the case of $La_{0.67}Ca_{0.33}Mn_{1-x}M_xO_3$ (M = Co,Ni) the EPR linewidth increases drastically with Co substitution and weakens the signal whereas for Ni substitution the changes are very little. Rapid spin-lattice relaxation of Co ion and smaller spin-lattice relaxation mechanism for Ni are shown to be responsible for this difference. Blanco *et al.* observed that the effect of line broadening due to Fe substitution is in between that due to Co and Ni substitution for Mn in $Nd_{0.7}A_{0.3}Mn_{1-x}M_xO_3$ (A = Pb, Cd; M = Co, Ni) [14].

5.10 Discussion

The magnetic properties of the different $LaMn_{0.5}Fe_{0.5}O_3$ samples can now be explained based on the observations from different measurements. In LMF200, the magnetic exchange interactions in the small Mn-rich clusters are ferromagnetic and large Fe-rich clusters are antiferromagnetic, as shown by Tanaka *et al.* [35]. The peak observed in the ZFC magnetization curve is likely to be due to an antiferromagnetic transition or a superparamagnetic blocking transition due to the small Mn-rich ferromagnetic clusters. The large value of the effective magnetic moment of this sample and the lower value of the Weiss temperature because of antiferromagnetic contributions is an evidence for these conclusions. In the case of LMF700 showing some peculiar properties such as relatively large isomer shift, lower magnetization and EPR intensity, symmetric IR band, and μ_{eff} closer to the spin-only value for Fe^{3+}/Mn^{3+} combination, the Mn^{3+} and Fe^{3+} ions are distributed somewhat uniformly in the lattice. However, still there is some contribution from a ferromagnetic like phase as evidenced by the magnetic hysteresi loops with very low magnetization and this is likely to be due to some isolated Mn rich clusters. In LMF1300, there are more and bigger ferromagnetic Mn-rich clusters so that the IR spectra resemble that of $LaMnO_3$ and some antiferromagnetic Fe-rich clusters which give rise to the antiferromagnetic transition, observed as a small shoulder at ∼70 K, the temperature at which a transition is observed in LMF200. Annealing at higher temperatures leads to a kind of phase separation with more Fe-rich and Mn-rich clusters.

In the case of $LaMn_{0.5}Co_{0.5}O_3$ and $LaMn_{0.5}Ni_{0.5}O_3$ which are ferromagnetic with transition temperatures of 230 K and 280 K respectively [25,36], for their high-T_C phases, the magnetic ions are high-spin Mn^{3+} and low-spin Co^{3+}/Ni^{3+}. When these compounds are synthesized by the low-temperature method and annealed at 200 °C, the magnetic transition temperature is ∼150 K and the magnetic ions are present as Mn^{4+} and Co^{2+}/Ni^{2+}. It may be argued that the same scenario is possible in $LaMn_{0.5}Fe_{0.5}O_3$ also with the contributions from Mn^{3+}/Fe^{3+} and Mn^{4+}/Fe^{2+} combinations giving rise to the observed magnetic properties for the samples annealed at different temperatures. However, as no evidence for Fe^{2+} is obtained in any of the samples from Mössbauer studies, the latter case can be ruled out. Also, the EPR spectral results are not in favor of Mn^{4+}/Fe^{2+} combination. Moreover, if it is assumed that Mn^{4+} and Fe^{2+} ions are present in LMF700 and these ions are distributed more uniformly in the lattice as deduced from the IR data, the experimental value of the effective magnetic moment obtained from the magnetic susceptibility data is much larger than the spin-only moment for the combination of these ions. Tong *et al.* [28], from the magnetic, EPR and Mössbauer studies on $LaMn_{1-x}Fe_xO_3$ up to $x = 0.4$, have argued that double exchange interaction between Mn^{3+} and Fe^{3+} ions is responsible for ferromagnetism and that the Fe^{3+} may be in the intermediate spin state (t_4^{2g} e_g^1). However, studies on substitution of Fe for Mn in the A-site substituted CMR manganites show that Fe^{3+} ions are in their high-spin state. If it is assumed that Mn^{3+} and Fe^{3+} in their high-spin states are present in LMF700, then, because of the identical ionic sizes of these ions, they will be distributed randomly in the B-site of the perovskite lattice, so that some magnetic clusters will be formed. If the sizes of these clusters are very small, they will behave like superparamagnetic clusters. This way one can explain the origin of the superparamagnetic contribution in the sample. In fact, from studies on gradual substitution of Fe^{3+} for Co^{3+} in $LaMn_{0.5}Co_{0.5}O_3$ it has been shown that a random distribution of Mn^{3+} and Fe^{3+} ions in the lattice is responsible for the destruction of long range ferromagnetic order in $LaMn_{0.5}Fe_{0.5}O_{3.3}$ [37].

Based on the detailed studies on $x = 0.5$, and the evidences obtained from the Mössbauer and the IR Studies, the observed magnetic properties of different compositions in the $LaMn_{1-x}Fe_xO_3$ series annealed at different temperatures can be explained in terms of the formation of different sized clusters involving Mn^{3+} and Fe^{3+} ions. The samples annealed at 200 °C contain larger Fe rich clusters. As can be seen from the IR data, these compositions show more features of $LaFeO_3$ and minor features of $LaMnO_3$. The samples annealed at 700 °C, are likely to have almost uniform distribution of Mn^{3+} and Fe^{3+} ions, with the presence of smaller and uniform sized clusters. However, still there is some contribution from a ferromagnetic like phase in these samples as evidenced from the low magnetization observed from the M-H measurements. This can be attributed to the presence of some isolated Mn clusters in the samples. In the case of the samples annealed at 1300 °C, the sharp magnetic transitions and enhanced magnetization indicate the presence of larger Mn rich ferromagnetic clusters and smaller Fe-rich antiferromagnetic clusters in these samples.

5.11 Conclusions

The magnetic and structural properties of $LaMn_{1-x}Fe_xO_3$ ($0.1 \leq x \leq 0.5$), synthesized by a low temperature combustion method have been studied in detail in order to understand the origin of the absence of ferromagnetism when Mn is substituted by Fe in $LaMnO_3$. The magnetic properties are found to be very sensitive to the processing temperatures. For the low temperature synthesized samples annealed at 200 °C, the magnetic transition is found to become weak and broad with increasing Fe content. However, the samples annealed at 700 °C very weak magnetism is observed for all compositions and no magnetic transition at all is observed for $x = 0.5$ down to 12 K. However, the M-H curve recorded at 12 K shows that this sample is not truly paramagnetic. The samples annealed at 1300 °C show enhanced magnetization at 12 K for all the compositions and distinct magnetic transitions, indicating the presence of magnetic order in all the compositions, including x

= 0.5.

Previous studies on $LaMn_{0.5}Fe_{0.5}O_3$ have reported widely differing magnetic properties for this compound. No ferromagnetism in the compound was observed down to liquid nitrogen temperature in an earlier report whereas recent studies showed weak ferromagnetic contributions below 250 K. The samples in the reported studies are made by different methods and processed at different temperatures. We have studied the magnetic properties of the compound synthesized by a low-temperature method and heated at different temperatures in the temperature range 200 °C to 1300 °C. Mössbauer, EPR and IR spectroscopic studies along with the magnetic data give information on the changes in the distribution of the Mn^{3+} and Fe^{3+} ions in the compound when processed at different temperatures. When Mn-rich and/or Fe-rich clusters with different sizes are formed, the compound shows predominant ferromagnetic or antiferromagnetic character whereas more uniform distribution of these ions makes it nonmagnetic. Thus, from the present study, the interesting magnetic properties observed for polycrystalline $LaMn_{1-x}Fe_xO_3$ can be explained based on a two-phase model where the degree of distribution of Mn and Fe ions in the lattice varies when the compound is annealed at different temperatures.

References

[1] J. M. D. Coey, M. Viret and S. von Molnar, *Adv. Phys.* 48 (1999) 167.

[2] M. B. Salamon and M. Jaime, *Rev. Modern Phys.* 73 (2001) 583.

[3] C. N. R. Rao and B. Raveau (Ed.), *Colossal Magnetoresistance, Charge Ordering and Related Properties of Manganese Oxides* (World Scientific, Singapore, 1998).

[4] Y. Tokura(Ed.), *Colossal Magnetoresistive Oxides* (Gordon and Breach Science, Singapore, 2000).

[5] E. O. Wollan and E. O. Khehler, *Phys. Rev.* 100 (1955) 545.

[6] B. Raveau, C. Martin and A. Maignan, *J. Alloys Comp.* 275277 (1998) 461.

[7] A. Wold, R. J. Arnott and J. B. Goodenough, *J. Appl. Phys.* 29 (1958) 387.

[8] J. B. Goodenough, A. Wold, R. J. Arnott and N. Menyuk, *Phys. Rev.* 124 (1961) 373.

[9] G. Blasse, *J. Phys. Chem. Solids* 26 (1965) 1969.

[10] K. H. Ahn, X. W. Wu, K. Liu and C. L. Chien, *Phys. Rev.* B 54 (1996) 15299.

[11] L. Righi, P. Gorria, M. Insausti, J. Gutierrez and J. M. Barandiaran, *J. Appl. Phys.* 81 (1997) 5767.

[12] J. Gutierrez, A. Pena, J. M. Barandiaran, J. L. Pizarro, T. Hernandez, L. Lezama, M. Insausti and T. Rojo, *Phys. Rev.* B 61 (2000) 9028.

[13] M. Rubinstein, D. J. Gillespie, J. E. Snyder and T. M. Tritt, *Phys. Rev.* B 56 (1997) 5412.

[14] J. J. Blanco, L. Lezama, M. Insausti, J. Gutierrez, J. M. Barandiaran and T. Rojo, *Chem. Mater.* 11 (1990) 3464.

[15] Y. L. Chang, Q. Huang, C. K. Kong, *J. Appl. Phys.* 91 (2002) 789.

[16] J. B. Goodenough, *Magnetism and Chemical Bond*, (John Wiley & Sons: New York, 1963).

[17] K. Ghosh, S. B. Ogale, R. Ramesh, R. L. Greene, T. Venkatesan, K. M. Gapchup, R. Bathe and S. I. Patil, *Phys. Rev.* B 59 (1990) 533.

[18] S. Hebert, A. Maignan, C. Martin and B. Raveau, *Solid State Commun.* 121 (2002) 229.

[19] M. A. Gilleo, *Acta Crystallogr.* 10 (1957) 161.

[20] K. Ueda, H. Tabata and T. Kawai, *Phys. Rev.* B 60 (1999) R12561.

[21] K. Ueda, Y. Muraoka, H. Tabata and T. Kawai, *Appl. Phys. Lett.* 78 (2001) 512.

[22] R. D. Shannon, *Acta Crystallogr.* A 32 (1976) 751.

[23] K. De, R. Ray, R. N. Panda, S. Giri, H. Nakamura and T. Kohara, *J. Magn. Magn. Mater.* 288 (2005) 339.

[24] P. A. Joy, Y. B. Khollam, S. N. Patole and S. K. Date, *Mater. Lett.* 46 (2000) 261.

[25] V. L. Joseph Joly, P. A. Joy, S. K. Date and C. S. Gopinath, *Phys. Rev.* B 65 (2002) 184416.

[26] Y. Wu, Z. Yu and S. Liu, *J. Solid State Chem.* 112 (1994) 157.

[27] Y. Miwa, A. Yamamoto, K. Oda and H. Otsuka, *Trans. Mater. Res. Soc. Jpn.* 25 (2000) 1057.

[28] W. Tong, B. Zhang, S. Tan and Y. Zhang, *Phys. Rev.* B 70 (2004) 014422.

[29] G. V. S. Rao, C. N. R. Rao and J. R. Ferraro, *Appl. Spectrosc.* 24 (1970) 436.

[30] F. M. A. Da Costa and A. J. C. Dos Santos, *Inorg. Chim. Acta* 140 (1987) 105.

[31] L. Fournes, Y. Potin, J. C. Grenier, G. Demazeau and M. Pouchard, *Solid State Commun.* 62 (1987) 239.

[32] Z. Klencsar, Z. Nemeth, A. Vertes, I. Kotsis, M. Nagy, A. Cziraki, C. Ulhaq-Bouillet, V. Pierron-Bohnes, K. Vad, S. Meszaros and J. Hakl, *J. Magn. Magn. Mater.* 281 (2004) 115.

[33] Zs. Gercsi, F. Mazaleyrat, S. N. Kane and L. K. Varga, *Mater. Sci. Eng.* A 375377 (2004) 1048.

[34] J. Gutierrez, A. Pena, J. M. Barandiaran, J. L. Pizarro, T. Hernandez, L. Lezama, M. Insausti and T. Rojo, *Phys. Rev.* B 61(2000) 9028.

[35] H. Tanaka, N. Okawa and T. Kawai, *Solid State Commun.* 110 (1999) 191.

[36] P. A. Joy, Y. B. Khollam and S. K. Date, *Phys. Rev.* B 62 (2000) 8608.

[37] V. L. Joseph Joly, S. D. Bhame, P. A. Joy and S. K. Date, *J. Magn. Magn. Mater.* 261 (2003) 433.

List of Publications

1. "Enhanced magnetostrictive properties of $CoFe_2O_4$ synthesized by an auto combustion method"

   Shekhar D. Bhame and P. A. Joy, *Sensors and Actuators* A 137 (2007) 256.

2. "Magnetic and magnetostrictive properties of Mn substituted cobalt ferrite."

   Shekhar D. Bhame and P. A. Joy, *J. Phys. D: Appl. Phys.* 40 (2007) 3263.

3. "Tuning the magnetostrictive properties of $CoFe_2O_4$ by Mn substitution for Co."

   Shekhar D. Bhame and P. A. Joy, *J. Appl. Phys.* 100 (2006) 113911.

4. "Enhanced magnetostrictive properties of Mn substituted $Co_{1.2}Fe_{1.8}O_4$"

   Shekhar D. Bhame and P. A. Joy, *J. Appl. Phys.* 99 (2006) 073901 .

5. "Effect of disorder on the magnetic properties of $LaMn_{0.5}Fe_{0.5}O_3$"

   Shekhar D. Bhame, V. L. Joseph Joly and P. A. Joy, *Phys. Rev. B* 72 (2005) 054426.

6. "A facile liquid foam based synthesis of Ni nanoparticles and their subsequent conversion to $Ni_{core}Ag_{shell}$ particles: structural characterization and investigation of magnetic properties"

   T. Bala, **S. D. Bhame**, P. A. Joy, B. L. V. Prasad and Murali Sastry, *J. Mater. Chem.* 14 (2004) 2941.

7. "Magnetic properties of $La_2MnCo_{1-x}Fe_xO_6$"

   V. L. Joseph Joly, **S. D. Bhame**, S. K. Date and P. A. Joy, *J. Magn. Magn. Mater.* 261 (2003) 433.

8. "Ferromagnetic properties of low-temperature synthesized $LaMn_{1-x}Fe_xO_3$"

   V. L. Joseph Joly, **S. D. Bhame**, P. A. Joy and S. K. Date, *Inorganic Materials: Recent Advances* (Narosa Publishing New Delhi) p286, (2004).

9. "Effect of sintering conditions and microstructure on the magnetostrictive properties of cobalt ferrite "

   Shekhar D. Bhame and P. A. Joy, *Communicated.*

Awards:

"**Best Poster Award**" in National Science Day poster presentation competition, by NCL Research Foundation 2007, National Chemical Laboratory, Pune, India.

"**Award of Senior Research Fellowship (SRF)**" for 2004-2007 yrs. by Council of Scientific and Industrial Research (CSIR) , Govt. of India, New Delhi.

Workshops:

1. SERC Summer School on "Magnetism and Superconductivity" School of Physics, University of Hyderabad, Hyderabad, 2006.

Symposia and Conferences

Oral presentation

1. "*Effect of Fe doping on the high Tc phase of* $LaMn_{0.5}Co_{0.5}O_3$" National Seminar on Electro and Magneto Ceramics Devices and Systems, (NSEMCDS-2002) held at Akluj.

Poster presentation

1. "*Ferromagnetic properties of low-temperature synthesized* $LaMn_{1-x}Fe_xO_3$ ($x \leq 0.5$)" International seminar on Recent Advances in Inorganic Materials, (RAIM-2002), IIT Bombay, Powai, Mumbai [2002].
2. "*Magnetic and magnetostrictive properties of cobalt ferrite doped with terbium*" Materials for Future conference, IISC, Bangalore [2004].
3. "*Magnetic properties of terbium substituted cobalt ferrite*" Materials Research Society of India, NCL, Pune [2005].
4. "*Spin glass like properties of* $LaMn_{0.5}Fe_{0.5}O_3$" National Symposium and Conference on Solid State Chemistry and Allied Areas, ISCAS-2005 , Goa University, Goa, [2005].
5. "*Cluster size dependent magnetic properties Of low-temperature synthesized polycrystalline* $LaMn_{0.5}Fe_{0.5}O_3$ " Royal Society of Chemistry, RSC, Pune, [2005].
6. "*Magnetoelastic properties of Mn substituted cobalt ferrite* " National Science Day Poster Presentation, NCL Research Foundation, National Chemical Laboratory, Pune, [2007].